Probing Adsorption of Divalent Cations on Kaolinite Clay Surfaces by Atomic Force Microscopy

by

Jing Chang

A thesis submitted in partial fulfillment of the requirements for the degree of

Doctor of Philosophy

in
Chemical Engineering

Department of Chemical and Materials Engineering
University of Alberta

Abstract

Kaolinite is one of the most commonly-used clay minerals in the production of paper, plastics, and ceramics, etc. However, kaolinite is also a hard-to-remove mineral in the processing of valuable minerals or energy resources, such as bauxite, metal sulphide ores, and oil sands. The main problem stems from the stability of the micron-to-nanosized kaolinite particle suspension, which is dominated by the colloidal interactions between the charged kaolinite particles. To provide clear insights into the colloidal behaviour of kaolinite that governs its vast applications in lab research and industry, the surface charging properties of kaolinite particles and interactions of kaolinite with divalent cations were studied using atomic force microscope (AFM).

The two-layer kaolinite ($Al_2[Si_2O_5](OH)_4$) has three kinds of external surfaces: a siloxane (SiOSi) basal plane, an aluminium oxy-hydroxyl basal plane, and edge surfaces. To obtain different kaolinite basal planes, kaolinite suspensions with particle sizes of 1 ~ 2 μm were prepared and deposited on clean glass and sapphire substrates using a fast heating process. To expose the edge surfaces of kaolinite particles, ultramicrotome cutting technique was applied to cut a resin block with kaolinite particles sandwiched in the middle.

The interaction forces between AFM tips and different kaolinite surfaces were measured in 10 mM KCl solutions with varying concentrations of Ca^{2+} and Mg^{2+} at different pHs. The measured interaction forces were fitted with the classical DLVO theory to derive the Stern potentials of various types of kaolinite surfaces. Distinct responses in the measured Stern potentials of the two basal planes to divalent cations at pH 8 and 11 implied different binding mechanisms of the studied divalent cations at clay-solution interfaces, which were further explored by atomic resolution imaging. The change of the surface patterns of

kaolinite basal planes was observed due to the specific adsorption of divalent cations at high pH.

The three different surfaces of kaolinite were shown to form six possible inter-particle associations in a kaolinite suspension. The interaction energies for these six kinds of associations were calculated using the Stern potentials determined from the AFM force measurements. Based on the calculation, the rheological behaviour and the settling test results of kaolinite suspension were scientifically interpreted.

The findings in this dissertation provide fundamental understanding on the adsorption of divalent cations at the clay-solution interfaces. The techniques used in this study might open opportunities for more extensive explorations of features on material surfaces at atomic level.

Preface

The contents in this thesis include drafts for three manuscript that have been written and are under proofreading by co-authors. Here, we introduce the tittles and authors of the three papers, and their contributions.

1. Jing Chang, Bo Liu, Huaizhi Shao, Rogerio Manica, Qingxia Liu, Zhenghe Xu. Imaging ionic distribution at kaolinite-electrolyte interface: direct evidence of specific adsorption. Jing Chang wrote this paper, performed all the experiments and all the data analysis. Bo Liu provided the idea of using atomic resolution imaging to probe ion adsorption. Huaizhi Shao helped with preparing the samples. Rogerio Manica did the proofreading. Qingxia Liu provided valuable suggestions and revised the manuscript. Zhenghe Xu supervised this work. All the authors contributed to the discussion and commented on the manuscript.

2. Jing Chang, Huaizhi Shao, Bo Liu, Rogerio Manica, Qingxia Liu, Zhenghe Xu. Interactions between Divalent Cations and Kaolinite Basal Planes Probed by AFM Force Measurements. Jing Chang wrote this paper, performed all the experiments and all the data analysis. Huaizhi Shao helped with preparing samples and background electrolytes. Bo Liu and Rogerio Manica wrote the Matlab codes. Rogerio Manica also helped with the proofreading. Qingxia Liu provided valuable suggestions to the manuscript. Zhenghe Xu supervised this work. All the authors contributed to the discussion and commented on the manuscript.

3. Jing Chang, Huaizhi Shao, Bo Liu, Rogerio Manica, Qingxia Liu, Zhenghe Xu. Understanding Rheology and Settling Behaviors of Kaolinite Suspension through Direct

Interaction Force Measurement Using AFM. Jing Chang wrote this paper, performed all the experiments and all the data analysis. Huaizhi Shao helped with preparing samples and background electrolytes. Bo Liu and Rogerio Manica wrote the Matlab codes. Qingxia Liu provided valuable suggestions to the manuscript. Zhenghe Xu supervised this work. All the authors contributed to the discussion and commented on the manuscript.

With great power comes great responsibility.

-- "Spider-Man", by Stan Lee

Acknowledgments

First and foremost, I wish to give my utmost gratitude to my supervisor, Professor Zhenghe Xu for giving me this valuable opportunity to fulfill my Ph.D study at the University of Alberta. I would like to express my heartful appreciation to Professor Qingxia Liu for being my co-supervisor. The intelligent guidance and continuous support from Professor Zhenghe Xu and Professor Qingxia Liu enabled me to gain research skills, develop critical thinking, maintain proper attitude and finally achieve my academic goal.

Special appreciation to my colleague, Bo Liu, for his friendship and giving me priceless idea on my research project.

I thank Dr. Rogerio Manica, for his help on the Matlab programming and all his encouragement.

Many thanks to Huaizhi Shao, my colleague, who helped me a lot on hours and hours of experiments with his patience.

I devoted my sincere gratitude to Ms. Jie Ru and Mr. James Skwarok, our technologists, and Dr. Chen Wang, for their training on grasping essential skills and offering me their valuable experience. I would also like to thank Ms. Lisa Carreiro for her assistance in managing my study here.

I thank all my colleagues from the research groups of Professor Zhenghe Xu and Professor Qingxia Liu, for their help on providing technical support, sharing knowledge and discussing my project.

The financial support from China Scholarship Council is acknowledged.

My accomplishment and achievements are owed to all my friends, for their company, support and understanding. My profound thanks to my parents, Huiping Zhang and Yinkui

Chang, for their unconditional love and their absolute faith in me even during the hardest time.

Table of Contents

Chapter 1 Introduction..... 1

1.1 Background and motivations..... 1

1.2 Objectives and scope of the thesis..... 2

1.3 Organization of the dissertation..... 3

Chapter 2 Literature Review..... 5

2.1 An overview of bitumen extraction..... 5

2.1.1 Fundamentals of water-based bitumen extraction process..... 5

2.1.2 Bitumen extraction process influence factors..... 6

2.1.3 Oil sands tailings..... 10

2.1.4 Tailings management methods..... 11

2.2 An introduction to clay minerals..... 13

2.2.1 Definition of clay and clay minerals..... 13

2.2.2 Applications of clay minerals..... 15

2.2.3 The anisotropic surface property of clay minerals..... 16

2.2.4 Investigation techniques for surface property of clay minerals..... 20

2.2.5 Probing anisotropic surface property of clay minerals using AFM..... 22

2.2.6 Influence of anisotropic surface property..... 25

2.3 Kaolinite..... 27

2.3.1 Background information for kaolinite..... 27

2.3.2 Structure of kaolinite 28

2.3.3 Particle aggregation 30

2.4 Ion distribution at a solid-liquid interface 31

2.4.1 Electric double layer theory 32

2.4.2 Debate on ion adsorption mechanisms 32

2.4.3 Atomic resolution imaging 33

Chapter 3 Materials and Methods 35

3.1 Materials 35

3.2 Sample preparation 36

3.2.1 Kaolinite basal planes 37

3.2.2 Kaolinite edge surfaces 38

3.3 Atomic force microscopy 38

3.3.1 AFM force measurement 38

3.3.2 AFM tip evaluation 40

3.3.3 Atomic resolution imaging by AFM 41

3.4 Theoretical model 42

Chapter 4 Determination of Stern Potentials of Kaolinite Surfaces: Effect of Divalent Cations and Solution pH 48

4.1 Introduction 48

4.2 Results and discussion 49

4.2.1 AFM tip calibration 49

4.2.2 Characterization of kaolinite samples..... 59

4.2.3 Effect of divalent cations on Stern potential of kaolinite Si-basal planes 63

4.2.4 Effect of divalent cations on Stern potential of kaolinite Al-basal planes ... 68

4.2.5 Effect of divalent cations on Stern potential of kaolinite edge surfaces 72

4.3 Summary 74

Chapter 5 Imaging of Ion Adsorptions on Kaolinite Basal Planes..... 79

5.1 Introduction 79

5.2 Results and discussion..... 79

5.2.1 Ion adsorption of monovalent ions 80

5.2.2 Ion adsorption of divalent ions 82

5.3 Summary 85

Chapter 6 Understanding Rheology and Settling Behaviors of Kaolinite Suspension 86

6.1 Understanding the rheology behavior of kaolinite suspension 86

6.1.1 Calculation of interaction energy 86

6.1.2 Shear yield stress measurement 87

6.1.3 Understanding kaolinite suspension rheology behavior through interaction energy calculation..... 88

6.2 Understanding the settling behavior of kaolinite suspension..... 92

6.2.1 Settling test 92

6.2.2 Understanding kaolinite suspension settling behavior through interaction energy calculation 93

Chapter 7 Conclusions and Future Work 98

7.1 Conclusions 98

7.2 Recommendations for future work 99

Bibliography 101

Appendices 109

Appendix A Atomic resolution image processing 109

Appendix B Error analysis of force fitting 111

Appendix C Speciation diagram 113

List of Tables

Table 2.1 Tailings management methods status 13

Table 2.2 Distinction between clay and clay minerals[24] 14

Table 2.3 Common uses of clay minerals 15

Table 2.4 Anisotropic surface properties of clay minerals studied by AFM 25

Table 2.5 Summary of reported PZC and IEP for kaolinite. 30

Table 3.1 Values used to calculate the Hamaker constants. 44

Table 5.1 Comparison of the unit cell spacing of kaolinite basal planes 81

Table 6.1 Prediction of the pH of the maximum shear yield stress for different pairs of surfaces from the calculated interaction energy profiles. 91

List of Figures

Figure 2.1 Program diagram of bitumen production from oil sands by open-pit mining technology[1]. 5

Figure 2.2 Formation of water layers in a tailings pond. 11

Figure 2.3 Schematics of phyllosilicates with anisotropic surfaces. 17

Figure 2.4 Structure of the tetrahedral sheet[27]. (a) tetrahedral arrangement of Si and O, (b) projection of tetrahedron on plane of sheet, (b) top view of tetrahedral sheet (dotted red line: unit cell area). Large grey circles represent oxygen; small red circles, silicon. 17

Figure 2.5 Structure of the octahedral sheet[27]. (a) octahedral arrangement of Al or Mg with O or OH, (b) projection of octahedron in two dimensions, and (c) top view of octahedral sheet (dotted red line: unit cell area). Large white circles represent oxygen atoms; large grey circles represent hydroxyl groups; small blue circles, aluminum atoms. 18

Figure 2.6 Relative amounts of clay minerals in oil sands deposits[52]. 28

Figure 2.7 Structure of kaolinite clays[36]. Red: oxygen; yellow: silicon; purple: aluminum; white: hydrogen. 29

Figure 2.8 Stairstep card-house structure of aggregated kaolinite particles[53]. 31

Figure 3.1 X-ray diffraction (XRD) analysis of kaolinite..... 35

Figure 3.2 Schematics of preparing kaolinite (a) Si-basal plane, (b) Al-basal plane, and (c) edge surfaces. 37

Figure 3.3 Illustration of the electric double layer (shown as grey thin layer) surrounding the AFM tip, kaolinite and substrate in electrolyte solutions with $\kappa - 1$ less than the thickness (d) of the kaolinite particle. 39

Figure 3.4 SEM images of the side view of (a) a cantilever with a DNP-10 AFM tip on top at low magnification, (b) DNP-10 AFM tip at high magnification, (c) cantilever with a SNL-10 AFM tip on top at low magnification, and (d) SNL-10 AFM tip at high magnification. 41

Figure 3.5 Schematic illustration of the AFM tip-flat surface system used in the theoretical calculation. Angles α and β are the geometrical angles for the spherical cap at the tip apex and the conical tip body, respectively, and $\alpha + \beta = 90°$; D refers to the separation between the end of the tip apex and the surface of the substrate; L is the distance from the AFM tip to the substrate; R is the radius of the spherical cap at the tip apex; r is the radius of the tip at a given vertical position[40]. 42

Figure 4.1 Zeta Potential of silica wafer in 10 mM KCl solutions at pH 8 and 11 with varying concentrations of divalent cations (Ca^{2+} and Mg^{2+}, respectively) determined using the streaming potential method. 49

Figure 4.2 Comparison of the zeta potential of Si_3N_4 nano particles with the Stern potential of AFM Si_3N_4 tip in 10 mM KCl solutions at pH 8 and 11 containing different concentrations of (a) Ca^{2+} and (b) Mg^{2+}. 51

Figure 4.3 Interaction forces between the AFM Si_3N_4 tip and the silica wafer in 10 mM KCl solutions (a) at different pH, (b) at pH 8 containing different concentrations of Ca^{2+}, (c) at pH 8 containing different concentrations of Mg^{2+}, (d) at pH 11 containing different concentrations of Ca^{2+}, and (e) at pH 11 containing different concentrations of Mg^{2+}; and (f) Comparison of the Stern potentials of the AFM Si_3N_4 tip obtained in this this study with those reported in literature. 53

Figure 4.4 (a) Representative AFM image of a silica wafer surface; and typical interaction forces (solid lines represent theoretical DLVO forces, open symbols represent experimental data) between the AFM Si tip and the silica wafer in 10 mM KCl solutions (b) at different pH, (c) at pH 8 containing different concentrations of Ca^{2+}, (d) at pH 8 containing different concentrations of Mg^{2+}, (e) at pH 11 containing different concentrations of Ca^{2+}, and (f) at pH 11 containing different concentrations of Mg^{2+}. ... 57

Figure 4.5 SEM images of kaolinite particles deposited on (a) glass substrate and (b) sapphire substrate after drying on a hot plate; AFM images of kaolinite particles deposited on (c) glass substrate and (d) sapphire substrate, after the substrate was rinsed with Milli-Q water and blown dry. 59

Figure 4.6 Interaction forces between an AFM tip and silica wafer (a), kaolinite particles sitting on a glass substrate (b), and particles sitting on a sapphire substrate (c) in 10 mM KCl solutions of pH 5 (open symbols represent experimental data, and solid lines represent theoretical DLVO forces). 61

Figure 4.7 SEM images of (a) kaolinite particles deposited on the resin surface, and (b) kaolinite edge surfaces prepared by ultramicrotome cutting technique; and (c) AFM image of kaolinite edge surfaces..... 62

Figure 4.8 Interaction forces between the AFM Si_3N_4 tip and the kaolinite Si-basal plane in 10 mM KCl solutions (a) at different pH, (b) at pH 8 containing different concentrations of Ca^{2+}, (c) at pH 8 containing different concentrations of Mg^{2+}, (d) at pH 11 containing different concentrations of Ca^{2+}, and (e) at pH 11 containing different concentrations of Mg^{2+}; and (f) Summary of the Stern potential of kaolinite Si-basal plane at pH 8 and 11 in 10 mM KCl solutions containing different concentrations of Ca^{2+} and Mg^{2+}. 64

Figure 4.9 Interaction forces between the AFM Si_3N_4 tip and the Al-basal plane of kaolinite in 10 mM KCl solutions (a) at different pH, (b) at pH 8 containing different concentrations of Ca^{2+}, (c) at pH 8 containing different concentrations of Mg^{2+}, (d) at pH 11 containing different concentrations of Ca^{2+}, and (e) at pH 11 containing different concentrations of Mg^{2+}; and (f) Summary of the Stern potential of kaolinite Al-basal plane at pH 8 and 11 in 10 mM KCl solutions containing different concentrations of Ca^{2+} and Mg^{2+}. 68

Figure 4.10 Typical interaction forces between the AFM Si tip and kaolinite edge surface in10 mM KCl solutions (a) at different pH, (b) at pH 8 containing different concentrations of Ca^{2+}, (c) at pH 8 containing different concentrations of Mg^{2+}, (d) at pH 11 containing different concentrations of Ca^{2+}, and (e) at pH 11 containing different concentrations of Mg^{2+}; and (f) summary of the Stern potentials of kaolinite edge surfaces. 72

Figure 4.11 Schematics of the adsorption of divalent cations on kaolinite surfaces at pH 8. 77

Figure 4.12 Schematics of the adsorption of divalent cations on kaolinite surfaces at pH 11. 77

Figure 5.1 Surface lattice structure of kaolinite: Top view of the T sheet (a), and atomic resolution images of kaolinite Si-basal plane in Milli-Q water (b) and 10 mM KCl solution (c) at pH 5; Top view of the O sheet (d), and atomic resolution images of kaolinite Al-basal plane in Milli-Q water (e) and 10 mM KCl solution (f) at pH 5; with insets being high resolution views (top) and 2D spectrum (Fast Fourier Transform) image of the same data (bottom) (large white, solid circle represents oxygen; large, dotted circle shows the fourth oxygen atom of each tetrahedron pointing downward; small red circle represents silicon; large grey, solid circle represents hydroxyl; small blue circle represents aluminum)..... 80

Figure 5.2 Atomic resolution images of kaolinite Si-basal (a), and Al-basal plane (b) in 10 mM KCl + 1 mM Ca^{2+} at pH 8; kaolinite Si-basal plane (c), and Al-basal plane (d) in 10 mM KCl + 1 mM Ca^{2+} at pH 11. 83

Figure 5.3 Schematic of AFM tip scanning surface in solution. 84

Figure 6.1 Impact of solution pH on the shear yield stress of kaolinite suspension. 88

Figure 6.2 Interaction energy/unit area between different kaolinite surfaces in 10 mM KCl solutions at different pHs. 89

Figure 6.3 Proposed aggregate structures: (a) card house structure; (b) parallel stacking; (c) dispersed structure. 92

Figure 6.4 Settling performance of kaolinite suspension. 93

Figure 6.5 Impact of divalent cations on the interaction energy/unit area between different kaolinite surfaces. 94

Figure 6.6 Proposed aggregate structures in 10 mM KCl solutions with 0, 0.1 mM Ca^{2+} addition (a), with 0.5 and 1 mM Ca^{2+} addition (b), and with 5 mM Ca^{2+} addition (c). 96

Figure 6.7 Impact of Mg^{2+} on the settling performance of kaolinite suspension. 97

Figure A1. Image processing procedure. (a) Original atomic resolution image after being flattened, (b) Spectrum 2D image, (c) inverse FFT image, and (d) zoomed-in view of (c). 109

Figure C1. Concentration diagram for 10^{-3} mol/L Ca^{2+} and Mg^{2+} 113

Nomenclature

Abbreviations

AFM	atomic force microscope
BC	boundary condition
CEC	cation exchange capacity
EDL	electrical double layer
FFT	fluid fine tailings
IEP	isoelectric point
ISR	initial settling rate
MFT	mature fine tailings
PZC	point of zero charge
SEM	scanning electron microscope

Symbols

A	Hamaker constant, J
c_0	bulk concentration of the salt
e	electronic charge, 1.6×10^{-19} C
F_{DLVO}	DLVO force, N
F_{edl}	electrostatic double-layer force, N
F_{vdw}	van der Waals force, N
h	Planck's constant, 6.63×10^{-34} J·s
k_B	Boltzmann constant, 1.38×10^{-23} J/K
n	refractive indexes
n_{i0}	bulk concentration of electrolyte *i*, ions/m^3
ν_e	main electronic absorption frequency in the UV region, s^{-1}
z_i	valence of ion *i*

Greek symbols

γ	shear rate, P
ε	static dielectric constants
ε_0	permittivity of vacuum, 8.85×10^{-12} C/mV
η_P	plastic viscosity, mPa.s
κ^{-1}	Debye length, m
σ	surface charge density, C/m^2
τ	shear stress, Pa
τ_B	Bingham yield stress, Pa
ψ	surface potential, V

Chapter 1 Introduction

1.1 Background and motivations

Oil Sands industry makes a major contribution to the economy of Canada. However, this profitable industry has caused serious environmental problem due to the generation of oil sands tailings, which mostly consists of kaolinite particles. The treatment of oil sands tailings and the reclamation of land are of great significance for environmental protection. The Alberta Energy Regulator enacted the Directive 074 to force operators to capture the fluid fine tailings (FFT) within 1 year of deposition and fully reclaim the landscape in 5 years. Unfortunately, since this was beyond the technology at that time, enforcement of Directive 074 was suspended in April 2015 due to difficulty in meeting all its targets. Directive 074 was replaced by directive 085 at October, 2017. Directive 085 requires that the fluid tailings volumes to be managed during and after mine operation, and the fluid tailings should be progressively reclaimed during the life of a project. New directive demands all fluid tailings that are related to a project need to be ready to reclaim within ten years after the end of mine life of that project.

As an unsolved problem, management of oil sands tailings still draws considerable research attention. The main problem of the tailings is that the fine particles in the tailings ponds cannot form dense flocs and then settle down fast, which is caused by the repulsive electrical double layer (EDL) forces among the charged fine particles. Currently, the two most effective methods used in dewatering of oil sands tailings are flocculation and coagulation. Flocculation uses polymers to bridge particles into large flocs, and the polymer bridge can extend beyond the range of electrical double layer (EDL) repulsion.

Coagulation uses inorganic multivalent cations to depress the repulsive forces till the attractive van der Waals forces become dominant and are able to bring and hold the particles together.

To manipulate the settling process, the charging characteristics of the fine clay particles should be well understood, as well as how the solution pH and the ions in the process water affect the charging features of the particles. As the main reagent used in oil sands tailings treatment, divalent cations and their impact on the anisotropic surface charging characteristics of kaolinite particle became the focus of this research. The ion adsorption mechanisms were also deeply investigated.

1.2 Objectives and scope of the thesis

The major objective of this work is to study the effect of monovalent and divalent ions on the anisotropic surface charging properties of kaolinite. Through the study of the Stern potential of kaolinite different surfaces under various solution conditions, possible ion adsorption mechanisms were proposed, and the mechanisms were further elucidated by atomic resolution imaging.

In the first part of this thesis, kaolinite samples were carefully prepared to expose the three different kinds of surfaces of plate-like kaolinite particles. Then AFM force measurements were performed on each kind of surface to explore the impact of background electrolyte pH and the impact of the concentration of divalent cations at lower and higher pHs. By analyzing the experimental data, proper ion adsorption mechanisms were proposed to explain the effect of different cations at different solution conditions.

In the second part of this thesis, atomic resolution imaging was conducted to confirm the ion adsorption mechanisms proposed in the first part. With the observation on the change in surface lattice structure caused by adsorption of divalent cations at high solution pH, specific adsorption was directly visualized and identified for the first time without involving any EDL model.

In the last part of this thesis, the knowledge learnt from microscopic scale study was applied to understand the behavior of kaolinite particles in the macroscopic processes. Using the Stern potentials obtained in the first part of this work, the interaction energies between different kaolinite surfaces were calculated to explain the rheology and the settling behaviors of kaolinite suspension.

1.3 Organization of the dissertation

This thesis consists of seven chapters.

Chapter 1 provides a short statement of the background, the origin and the main objectives of this research.

Chapter 2 presents a literature review on the most relevant background information or previous research on anisotropic surface charging properties of kaolinite particles.

Chapter 3 gives detailed descriptions of the materials and key experimental methods used in this study.

Chapter 4 shows the experimental data and in-depth data analysis on the Stern potential results. Corresponding ion adsorption mechanisms were proposed according to the experimental results.

Chapter 5 investigates the suggested ion adsorption mechanisms using experiments that were designed and performed to confirm our theory.

Chapter 6 uses the fundamental knowledge we gained in the microscopic scale to understand the kaolinite suspension behavior happens in the macroscopic level. By doing this, we were hoping the fundamental knowledge can provide guidance for the application in the real world.

Chapter 7 summarizes the work presented in this dissertation and gives suggestions on future work in this research field.

Chapter 2 Literature Review

2.1 An overview of bitumen extraction

2.1.1 Fundamentals of water-based bitumen extraction process

Oil sands are a kind of valuable unconventional fossil fuel, which spread throughout the world. Canada and Venezuela are the two countries that own the world's two largest sources of bitumen. In Canada, bitumen mostly concentrates in the province of Alberta. Thanks to the devotion of Dr. Karl Clark on oil sands extraction, bitumen recovery can be commercialized. The modified versions of the Clark Hot Water Extraction process (CHWE) are still being used in the current bitumen extraction, in which bitumen is separated from sand and clay particles by the joint efforts of mechanical energy, heat, and the presence of surfactants and caustic addition. This process is illustrated in Figure 2.1.

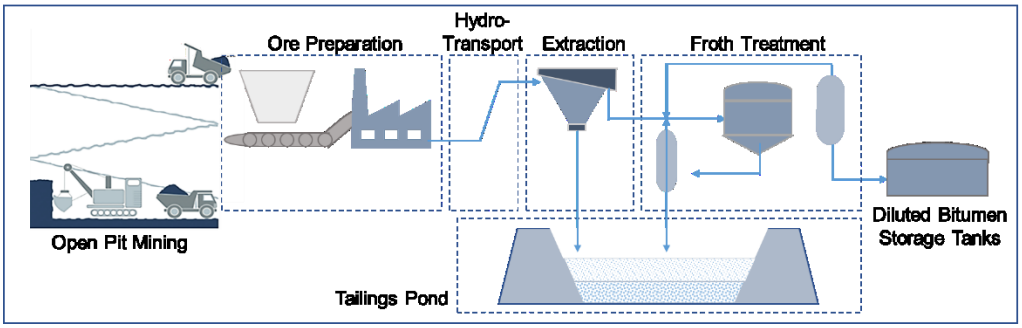

Figure 2.1 Program diagram of bitumen production from oil sands by open-pit mining technology[1].

The bitumen recovery process basically obeys the following procedures[2]:

1) Lump size reduction. In tumblers or hydrotransport pipelines, warm water heats up the lump surface, and the surface of lump is sheared away.

2) Bitumen liberation or separation. The influencing factors of the rate of this step are process temperature, mechanical agitation, chemical additives and interfacial properties.

3) The liberated bitumen attaches to an air bubble. The occurrence of bitumen attaching to an air bubble or engulfing an air bubble is determined by the process temperature. Under a low temperature (< 35˚C), the attachment of bitumen to air bubble takes place, while bitumen engulfs the air bubble in a warm (around 45 ˚C) or high (75~80 ˚C) temperature condition.

4) Bitumen flotation. After aeration, bitumen floats up to the top of the vessel and the bitumen froth can be recovered.

2.1.2 Bitumen extraction process influence factors

2.1.2.1 Slurry pH

In bitumen flotation, the induction time and contact angle can reflect the floatability and flotation rate. Wang et al.[3] measured the induction time in process water with different pH, and found out that the induction time changed marginally for pH 8 and 9 and increased significantly with a further increase in pH above 9.

The research of Liu et al.[4] reported that the solution pH greatly affected both the long-range and adhesion forces in a 1 mM KCl solution. The study showed that at low solution pH (say, pH < 7), the repulsive force between bitumen surfaces was low and the adhesion force was high, which was favorable for bitumen aeration but not favorable for bitumen liberation. The research also revealed that the contact angle changed slowly at pH below 8 and decreased drastically at pH 10.

Besides, the generation of the surfactants from the acids present in the bitumen is pH dependent. Increasing the slurry pH would lead to an enhanced natural surfactant generation.

2.1.2.2 Electric Surface Potential (Zeta Potential)

The electrokinetic behavior of bitumen in aqueous media is due to the interaction of polar groups contained by bitumen. Takamura and Chow[5] used the ionizable surface group model to explain the electrical properties of the bitumen/water interface, thus, the effect of pH and calcium ions on bitumen displacement from sand grain could be understood.

Liu et al.[6] reported the change of zeta potential of bitumen with solution pH at different levels of calcium addition. The results showed that higher solution pH and lower calcium concentration resulted in a system of more negative bitumen zeta potential, which is favorable for bitumen detachment from the silica surface.

2.1.2.3 Ions

Typically, industrial recycle process water contains various types and amount of inorganic ions, among which the dominant ions are Na^+, Cl^-, HCO^{3-}, SO_4^{2-} and a small portion of divalent cations of Ca^{2+} and Mg^{2+}.[7] In bitumen extraction, ions in the process water have a significant impact on bitumen recovery and bitumen froth quality.

- **Monovalent metal ions (Na^+, K^+)**

In industrial recycle process water, the concentration of sodium ions can reach up to 1000 ppm[8]. Coagulation would not take place at a low sodium concentration (e.g., below 10 mM), while a sodium concentration higher than 50-75 mM would cause coagulation, thus

reducing bitumen recovery[9–11]. However, the affiliation of sodium ions with anions (such as HCO_3^-) should also be taken into consideration.

- **Bicarbonate ions (HCO_3^-)**

As a dominant anionic species in process water, bicarbonate ions can help buffer the slurry in bitumen extraction at a mildly alkaline pH, which reduces the demand for caustic[7]. Besides, the presence of bicarbonate ions precipitated Ca^{2+} from the extraction process water, dispersed fine solids and reduced the bitumen-solid adhesion forces and thus improving the quality of bitumen extraction and bitumen froth.

Zhao et al.[7] found out that by adding small amount of acid (containing HCO^{3-}) into the water, the equilibrium of reactions (1.1) would be driven to the left side, and the happening of reaction (1.2) could increase the concentration of CO_3^{2-}, which caused the precipitation of Ca^{2+}. The mechanism can be seen as follows.

$$H_2CO_3 \Leftrightarrow H^+ + HCO_3^- \quad (1.1)$$

$$HCO_3^- \Leftrightarrow H^+ + CO_3^{2-} \quad (1.2)$$

$$Ca^{2+} + CO_3^{2-} \Leftrightarrow CaCO_3 \quad (1.3)$$

- **Divalent metal ions (Ca^{2+}, Mg^{2+})**

It was reported[12] that, in the water-based extraction of bitumen from oil sands, Ca^{2+} and Mg^{2+} in the process water had a great impact on the bitumen recovery. Ca^{2+} and Mg^{2+} were found to have a negative impact on bitumen liberation by Zhao et al.[13]. This is due to the increase of adhesion force and the decrease of long-range repulsive forces between silica and bitumen by the presence of the calcium and magnesium cations.

In aqueous based bitumen extraction system, calcium ion (Ca^{2+}) is one of the divalent ions added to alter the bitumen surface properties. According to the work by Liu et al.[4], calcium ions could absorb on the bitumen surface through a chemical bond with surface carboxylic groups (RCOO-) and thus affecting the bitumen surface properties. Besides, Ca^{2+} can also compress the electrostatic double layer. Their study indicated that the addition of Ca^{2+} weakened the attractive hydrophobic forces and the adhesion forces between bitumen surfaces, therefore the bitumen droplets could easily coagulate but were also easier to break up.

Calcium ions have a negative effect on bitumen liberation and oil sands lump crumbling due to their influence on reducing the receding rate of bitumen/liquid/solid three phase contact line[14,15]. Moreover, the presence of divalent ions can inhibit the ability of NaOH solution (pH = 11.8) to cause crumbling[16].

According to the work of Xu and Masliyah[17], the type of metal ions did not affect the bitumen recovery results, it was the valence that accounted for the depression effect. Besides, the reduction of bitumen recovery was not generated by the divalent cations alone, but because of their presence in combination with other factors, such as the existence of clay.

2.1.2.4 Surfactants

The addition of NaOH ionizes the organic acid in bitumen to generate surfactants, which is proposed to be able to establish a three-phase contact point to initiate bitumen recession from the sand grains and affect the electric surface potential of bitumen and fine solids. A mechanical model that the surfactants can reduce the oil solution interfacial tension has

been proposed to explain why the released surfactants contribute to bitumen separation, yet the model still remains to be verified[8]. However, it is a fact that alkaline pH environment can improve bitumen recovery due to increased activity of surfactants, negative charges on clay and sand surfaces, and reduced interfacial tension between bitumen droplets and solids[18].

2.1.3 Oil sands tailings

It was in 1967 when the Great Canadian Oil Sands (GCOS, now Suncor) learned that the fine solids in tailings could not settle nor consolidate fast, so that oil sands tailings started to become a problem because the tailings had to be stored in huge tailings ponds for a very long time[19]. With the rapid expansion of oil sands industry, this problem is becoming more and more intense, and the currently-existing tailings pounds occupy a total area of more than 130 square kilometers[20].

Oil sands tailings contain dissolved salts, organics, sands, fines (silts and clays), unrecovered bitumen, and a large amount of water that can be recycled as process water for the extraction process. The sand in the discharged slurry settles out quickly with the trap of some fines and water, but some fines take decades to settle, thus forming the three fractions as shown in Figure 2.2: (1) a clarified surface water layer (contains about 15-70 mg/L suspended solids); (2) a transition zone, in which the fines are settling; and (3) the fluid fine tailing (FFT) zone, which has 15%-30% solids content. With time, a higher solids content (>30%) tailings (mature fine tailing, shorted as MFT) is created with further settling[21].

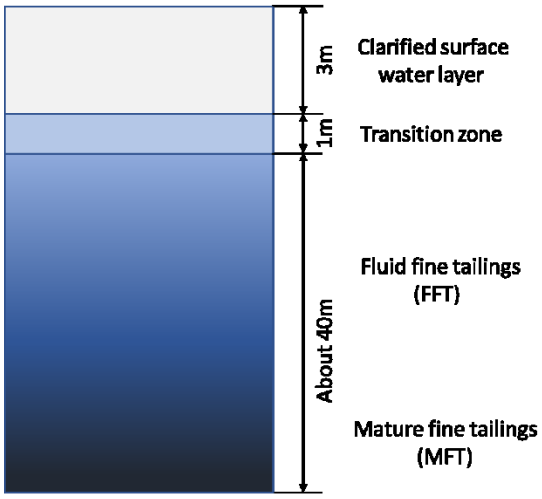

Figure 2.2 Formation of water layers in a tailings pond.

2.1.4 Tailings management methods

Since 1967, tailings management in oil sands industry has evolved for over 50 years, which can be divided into three overlapping development periods[21]:

1960s through 1980s: Waste management period. Large dams were built to store FFT, and space was left to long-term storage.

1990s through 2000s: Creating solid tailings landscapes. R & D of this period focused on sand capped composite tailings and water capped MFT end pit lakes.

2010s: Reducing the generation of tailings and speeding reclamation to meet new regulatory goals.

There are five process methods[22] currently being used to release water from oil sands tailings, which are described as follows:

Method I: In a solid-bowl scroll centrifuge, with the addition of coagulant such as gypsum, about 55% of the solids contents are consolidated into the centrifuge cake, which is deposited in relatively thin lifts of 2t/m^2-y in cells. After a winter freeze-thaw cycle, the cake will reach its peak shear strength before an additional lift is placed. Alternatively, the cake is continuously deposited into deep, in-pit deposits, the release of water can only depend on self-weight consolidation.

Method II: In-line flocculation of FFT is used, and the flocculated slurry is discharged into thin lifts into cells. The solids content is up to 60% after initial dewatering, and the dewatered material can be put into the overburden cells. Evaporation and freeze-thaw will help remove more water to form an integral part of a disposal structure.

Method III: In-line flocculated FFT is put in deep, large deposits. The water expressed from the deposit is decanted from the surface with the aid of rim-diching of the deposit or channels built on the surface. Further increase of the solids contents relies on the self-weight consolidation.

Method IV: The FFT is drawn from the extraction process to be flocculated and thickened in a mechanical thickener. The thickened tailings generated from this process are either placed in deep deposits for further dewatering by consolidation, or discharged in thin lifts.

Method V: FFT is blended with sand slurry with high solids content, and with the addition of flocculants or coagulants, a non-segregating mix with a moderately high sand-to-fines ratio is formed and then discharged into a deep deposit. If the source of the fines is mature fine tailings, the product is called composite tailings, otherwise, the product is called non-segregating tailings if the source of the fines is thickened tailings.

The following Table 2.1 lists the tailings management methods that are currently in commercial operation and that are still in R & D[19].

Table 2.1 Tailings management methods status

Status	Tailings management methods
In current commercial operation	Composite tailings, thickened tailings, in-line flocculation, thin-lift dewatering of MFT
Ready for commercial implementation	In-line flocculation, thin-lift dewatering of MFT, centrifugation, MFT spiking of whole tailings
In R& D	Freeze-thaw consolidation of fine tailings

2.2 An introduction to clay minerals

2.2.1 Definition of clay and clay minerals

Because clay scientists come from diverse disciplines, there are no uniform definitions for clay and clay mineral so far. The latest effort in this direction was made by the joint nomenclature committees (JNCs) of the Association Internationale pour L'Etude des Argiles (AIPEA) and the Clay Minerals Society (CMS). 'Clay' was defined by JNCs as "a naturally occurring material composed primarily of fine-grained minerals, which is generally plastic at appropriate water contents and will harden with dried or fired"[23], while 'clay mineral' was defined as "phyllosilicate minerals and minerals which impart plasticity to clay and which harden upon drying or firing" [24]. On top of this, Moore[25] pointed out that, although most of the minerals we have been dealing with are phyllosilicates, there are still

some exceptions. As researchers, first, we must separate the term 'clay' from 'clay mineral', and the differences between clay and clay mineral are listed in Table 2.2.

Table 2.2 Distinction between clay and clay minerals[24]

Clay	Clay mineral
Natural	Natural and synthetic
Fine-grained (< 2 μm or < 4 μm)	No size criterion
Phyllosilicates as principal constituents	May include non-phyllosilicates
Plastic	Plastic
Hardens on drying or firing	Hardens on drying or firing

Phyllosilicates, which mainly includes seven groups[25]: the 1:1 type serpentine-kaolin; the 2:1 type talc-pyrophyllite, smectite, vermiculite, true (flexible) mica, brittle mica, and chlorite.

Clay minerals, or more specifically, phyllosilicates, are characterized by the following properties[24]: i. a layered structure with nanometer range (the layer thickness of the 1:1 (TO) type is ~0.7 nm, and that of the 2:1 (TOT) type is ~1 nm); ii. the anisotropy of the layers or particles; iii. the existence of different types of topographies: external basal surfaces, edge surfaces, and internal (interlayer) surfaces; iv. the ease of surface modification (by adsorption, ion exchange, or grafting), typically external, and often internal surfaces; v. plasticity, and vi. hardening on drying or firing (with few exceptions).

2.2.2 Applications of clay minerals

Clay minerals are widely used in our daily life, modern industries, lab research, etc. The ever-growing applications of clay minerals make them a hot topic for scientists. Table 2.3 shows the common uses of clay minerals.

Table 2.3 Common uses of clay minerals

Layer type	Group	Industry field	Common application	Typical mineral	Chemical formula
1:1	Kaolin	Paper, plastics, rubber Pesticides Pesticides Ceramics	Filler, Carrier, diluent Porcelain,	Kaolinite	$Al_2Si_2O_5(OH)_4$
2:1	Talc	Plastics, rubber, paper industry Cosmetics, pharmaceutics Refractory industry	Filler Powders, pastes, lotions Refractories	Talc	$Mg_3Si_4O_{10}(OH)_2$
	Smectite	Building industry Pesticides Cosmetics	Brick, roofing tile Carrier Bases of creams	Montmorillonite	$(Na,Ca)_{0.33}(Al,Mg)_2(Si_4O_{10})(OH)_2 \cdot nH_2O$
	Vermiculite	Construction Package Foundries	Heat insulation, sound dissipation Shock proof materials, liquid absorption Thermal protection	Vermiculite	$(Mg,Fe,Al)_3(Al,Si)_4O_{10}(OH)_2 \cdot 4H_2O$
	Mica	Electrical industry Paints Cosmetics Coating	Insulation UV-, heat-stable and under-water paints Nacreous pigments Corrosion proof, polymer coating, underseal	Muscovite Illite	$KAl_2(AlSi_3O_{10})(OH)_2$ $(K,H_3O)(Al,Mg,Fe)_2(Si,Al)_4O_{10}[(OH)_2,(H_2O)]$
	Chlorite	Very few industrial uses	-	Clinochlore	$(Mg_5Al)(AlSi_3)O_{10}(OH)_8$

Source: adapted from Bergaya, F., 2006[24]

However, apart from all the useful applications in industry, clay minerals, such as kaolinite, chlorite, and smectite, can also be troublemakers in the purification of valuable mineral

resources and in the dewatering of tailings to achieve disposable sedimentation/ consolidation.

2.2.3 The anisotropic surface property of clay minerals

2.2.3.1 Structure of clay minerals

The structural elements of most clay minerals are based on two-dimensional arrays of Si-O tetrahedral sheet (T) and two-dimensional arrays of Al- or Mg-O-OH octahedral sheet (O)[26]. According to the ratio of T and O, phyllosilicates are classified as bilayer (1:1 type, TO) and trilayer (2:1, TOT). In 1:1 type structure, the unit layer is made of one T sheet and one O sheet, while the 2:1 type structure is characterized by one O sheet sandwiched between two T sheets. Individual layers are held together through interlayer cations, van der Waals interactions, electrostatic forces, and/or hydrogen bonding. The perfect tetrahedron and octahedron sheets are electrically neutral, but when higher valance cations are substituted by lower valence cations of similar sizes, (such as Si^{4+} is substituted by Al^{3+} in T, and Al^{3+} by Mg^{2+} in O), a net charge deficiency is generated. This phenomenon is called isomorphic substitution. The charge deficiency is balanced by interstitial compensating cations (K^+, Na^+, NH_4^+, Ca^{2+}, Mg^{2+}, Fe^{2+}, etc.) to make the clay minerals electrically neutral.

Due to the layered structure, a clay mineral consists of two different surfaces: the basal surface and the edge surface, as shown in the Figure 2.3.

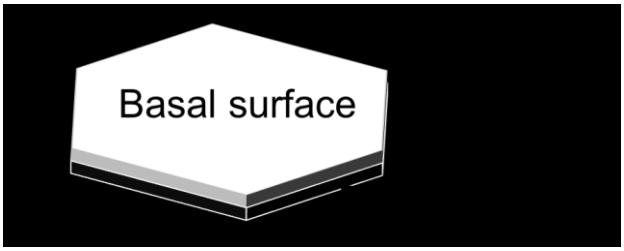

Figure 2.3 Schematics of phyllosilicates with anisotropic surfaces.

The tetrahedral sheet (as shown in Figure 2.4) is composed of silicon-oxygen tetrahedrons with oxygen atoms located on the four corners of each tetrahedron while the silicon atom sits in the center. Three out of the four oxygen atoms of a tetrahedron are shared by three neighboring tetrahedron, and the fourth oxygen atom (the apical oxygen) pointed downward and forms part of the adjacent octahedral sheet[26].

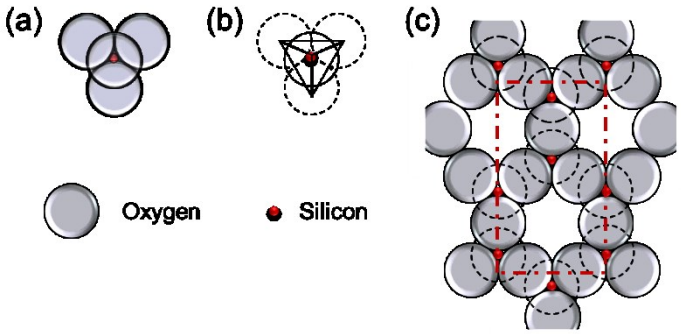

Figure 2.4 Structure of the tetrahedral sheet[27]. (a) tetrahedral arrangement of Si and O, (b) projection of tetrahedron on plane of sheet, (b) top view of tetrahedral sheet (dotted red line: unit cell area). Large grey circles represent oxygen; small red circles, silicon.

The octahedral sheet as shown in Figure 2.5 is linked laterally by sharing octahedral edges, in which, Al or Mg atoms are coordinated with six O atoms or OH groups which are located around the Al or Mg atom with their centers on the six corners of an octahedron. The O

atoms and the OH groups lie in two parallel planes with Al or Mg atoms between these two planes[26].

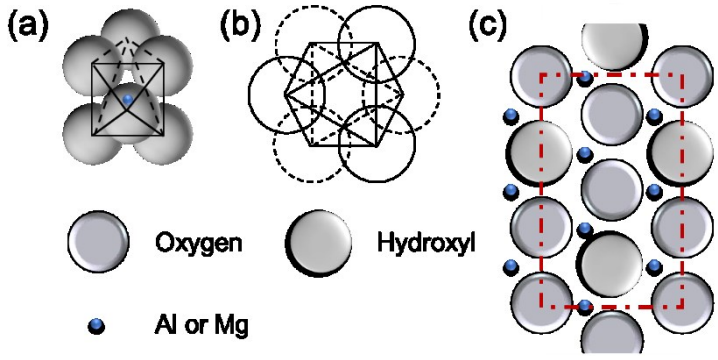

Figure 2.5 Structure of the octahedral sheet[27]. (a) octahedral arrangement of Al or Mg with O or OH, (b) projection of octahedron in two dimensions, and (c) top view of octahedral sheet (dotted red line: unit cell area). Large white circles represent oxygen atoms; large grey circles represent hydroxyl groups; small blue circles, aluminum atoms.

2.2.3.2 Layer/ surface charging mechanisms

For a phyllosilicate, the tetrahedral sheet and the octahedral sheet join together to form a layer, which can be electrically neutral or negatively charged. A electrically neutral layer case occurs when (i) two octahedral sites are occupied by trivalent cations (usually Al^{3+} and Fe^{3+}) in the O sheet, and leaves a vacancy in the third octahedron; (ii) all the octahedral sites are taken by divalent cations (usually Fe^{2+}, Mg^{2+}, Mn^{2+}); and (iii) all the tetrahedra in T sheet contains Si^{4+}. A negatively charged layer case comes from (i) isomorphic substitution of Al^{3+} for Si^{4+} in tetrahedral sites, and Mg^{2+} for Al^{3+} in octahedral sites; (ii) the existence of vacancies. Layer charge is of great significance to 2:1 phyllosilicates, because of which the exchangeable cations occupancy the interlayer space, and the negative layer charge varies from 0.2 to 2.0 per formula unit for different phyllosilicates.

For 1:1 type phyllosilicates, the layer charge is usually zero per formula unit, approximately[24].

The surfaces of a clay mineral can be negatively, positively charged, or electrical neutral due to different charging mechanisms on distinct surfaces. For basal surface, the prevailing charging mechanism is isomorphic substitution, while for edge surface, surface charges mainly come from the hydrolysis reactions of broken bonds[28].

When immersed in an aqueous environment, metal ions will be adsorbed on the mineral surfaces due to: (i) electrostatic interaction between metal cations and the negatively charged or neutral mineral surfaces; and (ii) specific adsorption of divalent cations and surface complexation.

2.2.3.3 Importance of anisotropic surface property

The layered structure of clay mineral makes the particle have distinct surfaces and thus, anisotropic surface property for each surface. Anisotropic surface property dominates the chemical and physical characteristics of clay minerals, such as colloidal stability, swelling, ion exchange, etc[28]. For example, in the dewatering of oil sands tailings, the maximum coagulation should occur at the point of zero charge (PZC) of the particles dispersed in the suspension, however, the PZC obtained from the correlation used to calculate the maximum coagulation point is only valid for isotropic particles, therefore, large discrepancy exists between the calculated PZC and the optimal pH condition for particle coagulation due to the anisotropic surface property of clay minerals. In this regard, the probing of the anisotropic surface properties of phyllosilicates is critical to the development of clay science and the applications of clay minerals in various fields.

2.2.4 Investigation techniques for surface property of clay minerals

The surface property of phyllosilicates is of significant importance and has been extensively studied using various techniques, which are mainly electrophoretic mobility (EPM) measurement, potentiometric titration, sum frequency generation spectroscopy and AFM. However, due to the limitation of individual technique, it is not surprising to see very distinct results for the same kind of clay mineral. Here we briefly introduce the pros and cons of commonly used investigation methods.

2.2.4.1 Electrophoretic mobility (EPM) measurement

Electrophoretic mobility measurement is one of the common methods used to yield the zeta potential of the particles when they are moving in an aqueous solution under the influence of an electric field. Sondi et al.[29] used the measurement of EPM to study the electrokinetic behavior of three pure clay minerals: montmorillonite, illite and chlorites, and the isoelectric point (IEP) of chlorite was found to be at pH 5.0 ± 0.2, while there were no IEP found for illite and montmorillonite. However, this method is used to deduce the zeta potential of the whole particle with assumption that the particles are spherical, which is far from the fact that phyllosilicates are platy and have anisotropic surface charging characteristics.

2.2.4.2 Potentiometric titration

The principle of potentiometric titration method is based on the ion exchange in solution, thus the results are not affected by the shape of the particles, but it still does not take the anisotropic property of clay minerals into consideration. Also, this method is limited to

systems without specific adsorbing ions in the solution. Therefore, the PZC of clay minerals determined by this method are not in good consistency[30].

2.2.4.3 Sum frequency generation (SFG) spectroscopy

SFG is used to explore the surface property of individual surface of clay minerals. In SFG method, two laser beams mix at an interface and generate an output beam. The frequency of the output is equal to the sum of the two input frequencies, and the direction of the output beam is given by the sum of the wavevectors of the two incident beams. When mineral particles are in contact of water at different pHs, protonation/deprotonation reactions happen and generate different interfacial water species. By analyzing the frequency intensities and the orientations of different interfacial water species at different pHs, the PZC of mineral particles can be estimated[31]. However, it is still a nascent technique without routine experimental setup and interpretation of the results[32], and there are few reports on the investigation of phyllosilicate surface properties using this method[28].

2.2.4.5 Atomic force microscopy

The atomic force microscope was invented by Gerber et al.[33] in the 1980s. AFM is a powerful and mature tool that can be used to image the topography of conducting and insulating surfaces with high resolution, and even with atomic resolution in some cases. In addition, AFM also allows the measurement of force-versus-distance curves, which can give us valuable information, such as the elasticity, hardness, surface potential, surface charge density, Hamaker constant etc. The single molecule force measurement of AFM, which mainly involves the rupture of single chemical bonds and the stretching of polymer chains, enables us to acquire the interactions of a single molecular pair[34].

The commercially fabricated tips used to scan the surfaces of clay minerals are silicon nitride (Si_3N_4) tip and silicon tip (Si), and the radii of the tips are usually between a few nanometers and a few tens of micrometers. In addition, the force measurement can be as sensitive as in pico-newton (pN) scale. So, AFM is very suitable for probing the surface property of clay minerals (whose size is usually in the scale of micron), and the interaction forces between AFM tip and clay surfaces in an aqueous/colloidal environment.

2.2.5 Probing anisotropic surface property of clay minerals using AFM

The use of AFM for surface property exploration of clay minerals was confined due to the challenge of creating smooth enough surface. In recent years, due to the development of ultramicrotome-cutting technology, which is able to provide surface smooth enough for AFM force measurement between AFM tip and the clay surface, AFM has been used in the study of the anisotropic surface properties of phyllosilicates, such as kaolinite, chlorite, mica, talc, MoS_2, illite, smectite, etc.

2.2.5.1 Sample preparation

When applying the AFM technique to determine the surface property of phyllosilicates, sample preparation is a critical step because a selected surface is hard to obtain and surface roughness greatly affects the accuracy of the results. A routine procedure has already been developed to make selected basal plane and edge surfaces.

Kaolinite, which is composed of one silica tetrahedral basal plane, one alumina octahedral basal plane, and edge surfaces, has been studied by Gupta[35], Liu[36], et al. The silica basal surface is believed to be negatively charged permanently, while the alumina basal surface is slightly pH-dependent. According to these charging characteristics, selected basal

surface can be prepared. In Gupta's work[35], silica basal surfaces were exposed by depositing kaolinite particles onto glass substrates (which carries negative charges at pH > 4, thus the positively charged alumina surfaces preferentially attached to the negatively charged glass substrate), and the alumina basal surfaces were exposed by depositing kaolinite particles on a fused alumina substrate (which carries positive charges at pH < 6). Liu et al.[36] completed the research on kaolinite by studying its edge surfaces through sandwiching kaolinite particles in the center of the epoxy resin, and the epoxy block was trimmed by a razor under optical microscope to obtain a prismatic sample with kaolinite particles exposed, then the sample was mounted into the slot of an ultramicrotome for cutting.

For talc, mica, and chlorite, which are easily cleaved phyllosilicates, cleaving these materials can expose atomically flat basal surfaces without contamination[37]. The preparation of edge surfaces of these phyllosilicates could also follow the above-mentioned experimental protocol for kaolinite edge surfaces.

2.2.5.2 Theoretical model

AFM force measurement between AFM tip and clay surfaces can be used to obtain the surface charging characteristics of phyllosilicates under aqueous environment. In such system, the interaction forces between phyllosilicate particle and AFM tip are governed by the sum of van der Waals (vdw) force and electrical double layer (EDL) force, which is the DLVO theory proposed by Derjaguin and Landau[38] and Verwey and Overbeek[39].

$$F_{DLVO} = F_{vdw} + F_{edl} \tag{2.1}$$

DLVO theory is commonly adopted to fit the force curves obtained from AFM measurement, and the derivation of the DLVO theoretical model for a pyramidal-shaped tip and a flat substrate has been conducted by Drelich et al.[40], which will be detailed explained in Chapter 3.

2.2.5.3 Reported results

Since the application of AFM technique has been used in the research of anisotropic surface properties of clay minerals, lots of the former results obtained from electrophoresis, titration have been shown to be not accurate enough. The more accurate surface charging characteristics of clay minerals should be achieved through this cutting-edge technique - AFM. The results are collected and listed in Table 2.4.

One thing that needs to be addressed here is the definition and difference between PZC and IEP, as they are frequently seen in reports to describe the zero charge characteristics of clay mineral surface, but which are also not clearly separated. The PZC is defined as the point at which the surface charge equals zero, and the IEP refers to the point at which the electrokinetic potential (or zeta potential) equals zero. More detailed difference between PZC and IEP was discussed by Kosmulski[41].

Table 2.4 Anisotropic surface properties of clay minerals studied by AFM

Group	Clay mineral	Cleavage (Basal) surface	Zero charge condition for basal surface	Zero charge condition for edge surface	Background electrolyte solution
Kaolin	Kaolinite[35,36]	T: Si-O-Si	IEP < pH 4, pH-dependent	PZC < pH 4, pH-dependent	Basal surface: 1 mM KCl solution Edge surface: 5 mM KCl solution
		O: Al-OH	pH 6 < IEP < pH 8, pH-dependent		
Talc	Talc[42]	T: SiOSi siloxane	~ 30 mV, pH-independent	PZC ~ pH 8, pH-dependent	1 mM KCl solution
Mica	Muscovite[42]	T: SiOSi siloxane	~ 70 mV, pH-independent	pH 7 < PZC < pH 8, pH-dependent	1 mM KCl solution
	Illite[43]	T: SiOSi siloxane	−18mV at pH 2.9, −37mV at pH 8.3, pH-dependent	-	1 mM KCl solution
Chlorite	Chlorite[44]	T: SiOSi siloxane	IEP < pH 5.6, pH-independent	IEP ~ pH 8.5, strongly pH-dependent	1 mM KCl solution
		O: MgOH hydroxyl	IEP > pH 9, slightly pH-dependent		
Sulfide mineral	Molybdenite	SMoS	None detected in pH 3.0-11.1	PZC ~ pH 3, pH-dependent	10 mM NaCl solution

2.2.6 Influence of anisotropic surface property

2.2.6.1 Influence on processing of clay minerals

Mineral processing is traditionally regarded as the processing of ores or other materials to obtain concentrated products[45]. Naturally, clays are mixtures of clay minerals and non-clay minerals, and in industry, extensive processing technologies are adopted to yield clay

minerals with a certain degree of purity. Typical processes for obtaining clay minerals may involve[24]:

i) purification;

ii) wet/dry processing;

iii) particle size separation;

iv) bleaching and magnetic separation;

v) flotation and selective flocculation;

vi) drying and calcination;

vii) chemical modification and activation.

The study on anisotropic surface properties of clay minerals can help us collect useful information, such as the clay mineral topography, surface charging characteristics, the suspension rheology[46], etc., which would be beneficial to clay mineral processing in various ways, for example[24]:

1) knowledge of the surface charging characteristics is useful in setting the optimal pH environment for the preparation of a stable dispersion of clays in wet processing, thus avoiding the aggregation of clay mineral particles;

2) rheology properties of soda-activated bentonites and the layer arrangement within individual montmorillonite particles determine the optimum addition of soda in the processing of raw bentonites;

3) particle shape and surface charge of clay minerals are important properties that affect the sedimentation or filtration process, which can be used to choose effective process aid agents.

2.2.6.2 Influence on industrial applications

As mentioned above, clay minerals have widely been used in numerous industrial applications. Anisotropic surface property of clay minerals will also affect their applications, such as:

1) in oil sands extraction, the understanding of the anisotropic surface-chemistry properties can guide the development of flotation reagent in the flotation separation process[47];

2) in oil sands tailings management, surface charging characteristics of kaolinite, chlorite, illite, etc. are critical in finding suitable coagulants or flocculants to accelerate the dewatering process[35,36,48];

3) in flotation process of molybdenite, the anisotropic surface properties can provide explanation of the variation in flotation recovery over the change of particle size[49].

2.3 Kaolinite

2.3.1 Background information for kaolinite

Kaolinite ($Al_2[Si_2O_5](OH)_4$) is a kind of phyllosilicates (sheet silicates), which accounts for about 69% of the clay in oil sands open pit mining, and other clay minerals include 28% illite, 0.3% smectite, and 1% chlorite, and 1.7% mixed layer clay, as shown in Figure 2.6. This overwhelming majority proportion of kaolinite makes it significantly important to

deeply and thoroughly understand its crystal structure and surface properties, which govern the wettability, aggregation, dispersion and flotation of kaolinite[50,51]. Therefore, the aggregation of kaolinite particles could be manipulated so as to benefit the treatment of oil sands tailings.

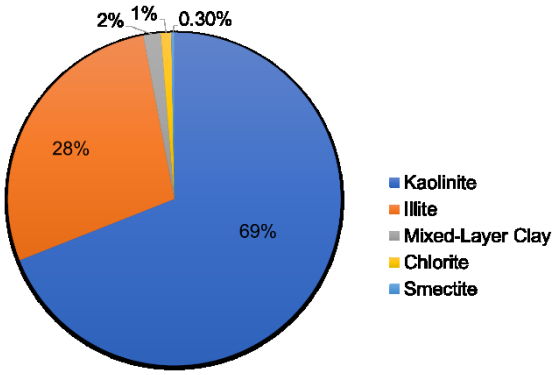

Figure 2.6 Relative amounts of clay minerals in oil sands deposits[52].

2.3.2 Structure of kaolinite

Kaolinite is usually white and soft with a hardness of 2-2.5[53]. Kaolinite has a perfect two-layer clay as shown in Figure 2.7, which is composed of three kinds of surfaces, one silica tetrahedral basal plane, one alumina octahedral basal plane, and edge surfaces. The bilayers are bonded together by hydrogen bonds between the hydroxyl ions of the octahedral sheet and the oxygen atoms of the silica tetrahedral sheet[54]. The non-expandable kaolinite has a low isomorphous substitution (which leads to a relatively low permanent charge) and a low cation exchange capacity (CEC).

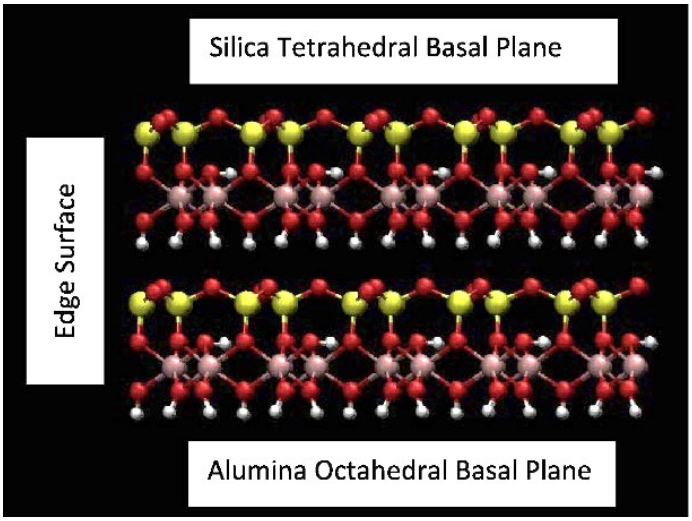

Figure 2.7 Structure of kaolinite clays[36]. Red: oxygen; yellow: silicon; purple: aluminum; white: hydrogen.

The different surfaces of kaolinite have different charging characteristics, which is governed by distinct charging mechanisms: isomorphous substitution on the basal plane and hydrolysis reactions of broken bonds on the edge surface[24].

In aqueous solution, the departure of the compensating cations results in the appearance of a surface charge on the external basal surfaces and near the layer edges of kaolinite. The silica basal plane is negatively charged permanently, and pH independent, while the alumina basal plane is slightly pH-dependent. The exposed aluminum hydroxyl surface can be protonated at low pH and deprotonated at high pH by following hydrolysis reactions, so the Al-OH surface is positively charged at low pH and negatively charged at high pH[55]. Whether the edges carry positive or negative charges strongly depends on pH and Si-Al ratio, so the PZC varies[24]. PZC is an important parameter because particles carry a net negative charge when the pH is above PZC, otherwise, particles carry a net positive surface charge while below PZC.

Table 2.5 Summary of reported PZC and IEP for kaolinite.

PZC	Measurement method	IEP	Measurement method
6-6.5[55]	Potentiometric titration	<2.4[56]	ζ-potential measurements
~4.5[57]	Titration	<3[27]	Electrophoresis measurements
<4[36]	AFM	2. 9[58]	ζ-potential measurements

The IEP reported are consistent. However, the indirect derivations of the surface charges of kaolinite particle vary over a wide range, and some of them can even be very misleading. Therefore, a reliable experimental measurement of the charging characteristics of kaolinite surfaces is necessary[53].

2.3.3 Particle aggregation

In hydrous dispersions, the dispersed clay particles can be observed to collide frequently due to the Brownian motion, but they separate again after the collision. However, this situation can be changed by just adding a small amount of salt. The clay particles stick together upon collision, and this phenomenon is called flocculation or coagulation[52]. The generation of this phenomenon can be explained by the theory of the stability and flocculation of colloidal dispersions. The attraction between dispersed particles is because of the van der Waals attraction force, while the repulsive force comes from the electrical nature. The particle charge can be altered by the presence or absence of ionized salt in the solutions, and the phenomenon mentioned above is because repulsion decreases when the ion concentration increases.

The interaction between kaolinite particles are governed by van der Waals force, electrical double layer force, hydrophobic force, and hydration force, etc., and according to the three different surfaces of kaolinite, there are three possible kinds of particle association modes: F(face) to F, E (edge) to F, and E to E. As show in Figure 2.8, a card-house structure was proposed for the kaolinite particle aggregates in suspension[26].

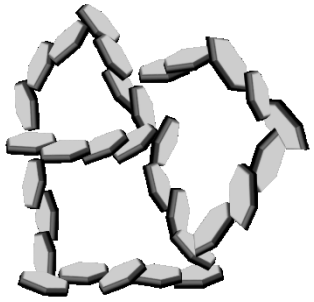

Figure 2.8 Stairstep card-house structure of aggregated kaolinite particles[53].

AFM is capable of measuring the above mentioned long-range and short-range interaction forces between particles, and of characterizing the surfaces for microscopic clay particles. Combined with DLVO theory, the analysis of AFM-measured forces can be used to compare the experimental results with the theoretical model predictions, and derive the surface potentials/charge densities, which are very useful for predicting the particle aggregation formation and thus guiding the dewatering process in oil sands tailings treatment[40].

2.4 Ion distribution at a solid-liquid interface

Generally, an aqueous environment containing various ions is inevitable when utilizing or removing clay mineral particles, and therefore the importance of studying ion adsorptions and ion distributions at the charged clay-liquid interface is self-evident.

2.4.1 Electric double layer theory

The study of charged interfaces can be traced back to about two hundred years ago. The first theoretical model for the charge distribution at the electrified interface was brought up by Helmholtz[59], which is the simplest model of electric double layer (EDL). The Helmholtz model treated the charge distribution on a solid surface as a plane layer of counter ions absorbed on the surface and neutralized the surface charges, which was unrealistic especially for solid-liquid interface. Gouy[60] and Chapman[61] developed the Helmholtz model by taking into account the diffusion and thermal motion of ions. In 1924, Stern[62] divided the EDL into an inner layer, the Stern layer, and an outer layer, the diffuser layer or Gouy layer. The Stern layer starts from the inner Helmholtz plane (IHP) where the specific adsorption occurs, and ends at the outer Helmholtz plane (OHP) where the non-specific adsorption of hydrated counterions starts. The Stern model can give a good account of the ion adsorption behavior at the solid-liquid interface in dilute electrolyte solutions[63]. For decades, the theoretical EDL models and corresponding calculations and experiments served for solving a universal question: how and where the ions adsorb on charged surfaces in liquid? Different approaches led to inconsistent conclusions.

2.4.2 Debate on ion adsorption mechanisms

Although there was consensus that monovalent ions (for example, Na^+, K^+, Cl^-) were "indifferent" ions because they could not change the point of zero charge (PZC) of oxide surfaces, there was a debate on whether monovalent ions could adsorb at the Stern layer. Some believed that monovalent cations were strongly hydrated and could only interact with the surface beyond the OHP, whilst monovalent anions behaved like individual ions and could adsorb specifically at the interface[64] because they were less hydrated. Another

explanation to the unchanging PZC of metal oxide in simple electrolyte solutions was equal adsorption of monovalent cations and anions in the inner layer at the PZC[65].

Divalent cations were regarded as specifically adsorbed at the solid-liquid interface at all times[65,66]. When Ardizzone et al.[66] observed the cadmium ions and lead ions started to strongly adsorbed onto the hematite surface at pH above 7 and above 4, respectively, the high adsorption value ascribed to bare ions alone seemed implausible. James and Healy[67–69] attributed the specific adsorption to the partially hydrolyzed species of divalent cations ($M(OH)^+$), and they believed that divalent metal ions had little contributions to the adsorption in the inner region of electrical double layers.

2.4.3 Atomic resolution imaging

The identification of specific adsorption has been ambiguous because previous experiments were mostly indirect (for example, depending on the examination of PZC) and corresponding analysis or calculations had to rely on the model of EDLs. All models were based on various levels of assumptions with specific constrains. Therefore, a completely model-independent method to identify specific adsorption at solid-liquid interface has been imperative.

AFM is a powerful tool to study the surface morphology, which has been successfully used to provide atomic resolution imaging on synthesized and natural clay particles. Gan et al.[70,71] obtained hexagonal lattice arrangement with a periodicity of about 0.47 nm of sapphire (0001) surface. Mugele and Siretanu et al.[72,73] studied ion adsorption on perfectly-cleaved mica and synthesized gibbsite surfaces, and they observed the surface structure of mica changed from hexagonal rings to rectangular symmetry due to high concentration of

divalent cation adsorption. Mugele and Siretanu et al. [74] went further to explore the atomic structure and surface defects of natural clay mineral, such as kaolinite, montmorillonite, etc.. In this work, we used the technique of atomic resolution imaging to compare the surface lattice structure before and after monovalent and divalent cations addition at low and high solution pHs, hoping to prove the ion adsorption mechanisms we proposed during the exploration of the influence of cations on the Stern potentials of different kaolinite surfaces.

Chapter 3 Materials and Methods

3.1 Materials

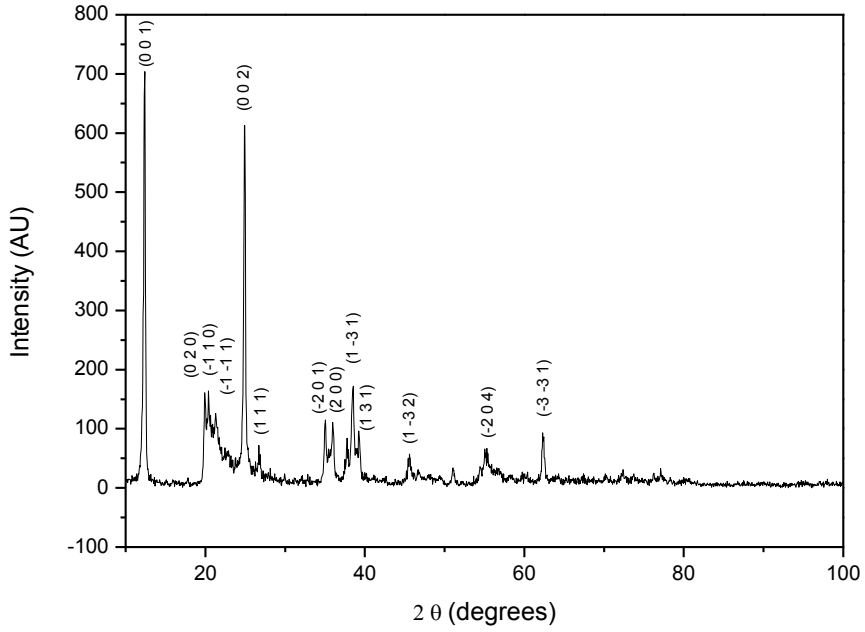

Figure 3.1 X-ray diffraction (XRD) analysis of kaolinite.

Preparation of kaolinite suspension: kaolinite particles used in this research were obtained from IMERYS kaolinite, Inc., and were used as received. X-ray diffraction (Rigaku XRD Ultima IV, Rigaku Corporation) pattern of the kaolinite sample shown in Figure 3.1 fits very well with XRD pattern of 80-0886, which represents kaolinite with chemical formula of $Al_2Si_2O_5(OH)_4$. Original kaolinite suspension (3.0 wt%) was prepared in high purity Milli-Q water (Millipore Inc.) with a resistivity of 18.2 MΩ·cm^{-1}. The suspension was magnetically stirred for 20 min, and then adjusted to pH 9 using 0.1 M HCl and 0.1 M KOH solutions, followed by five minutes of sonication to fully disperse the particles. After two hours of gravity settling (or four hours for edge surfaces preparation), the sediment of the suspension was discarded to remove the large particles, and the supernatant was

centrifuged at 500 g for 30 min in an Ultra Centrifuge (Sorvall WX80, Thermo Scientific Inc.) to remove the super-fine particles. The sediment was collected and centrifuged at 300 g for another 30 min. The supernatant was again decanted and the centrifuge cake was diluted in Milli-Q water (to about 3 wt% of clay) and then sonicated for 20 min to be fully dispersed. The re-dispersed kaolinite suspension was adjusted to about pH 5 for kaolinite basal planes preparation, and to pH 9 for kaolinite edge surfaces preparation.

The average particle size of the original kaolinite suspension was determined using MasterSizer 3000 (Malvern Instruments Ltd., UK) to be 6.6 μm. The re-dispersed kaolinite particles have the average size of 868 nm and 660 nm for two-hour and four-hour gravity settling, respectively, which were measured by a ZetaSizer Nano (Nano ZS, Malvern Instruments Ltd., UK).

3.2 Sample preparation

The sample preparation procedure developed by Gupta et al.[35] and the ultramicrotome cutting technique adopted by Yan et al.[42] enabled us to expose the two basal planes and the edge surface of kaolinite, respectively, to investigate the surface charging properties. At certain pH, the siloxane basal plane of kaolinite (referred to as Si-basal plane) is negatively charged while the aluminum oxy-hydroxyl basal plane of kaolinite (referred to as Al-basal plane) is positively charged. By using this property, Gupta et al.[35] successfully exposed the Si-basal plane and Al-basal plane by depositing kaolinite suspension onto a negatively charged glass substrate and a positively charged alumina substrate, respectively. To expose the edge surfaces, Yan et al.[42] embedded a thin piece of phyllosilicate clay in a resin block

and cut the cross section using an ultramicrotome. The schematics of the preparation of kaolinite basal planes and edge surfaces can be seen in Figure 3.2.

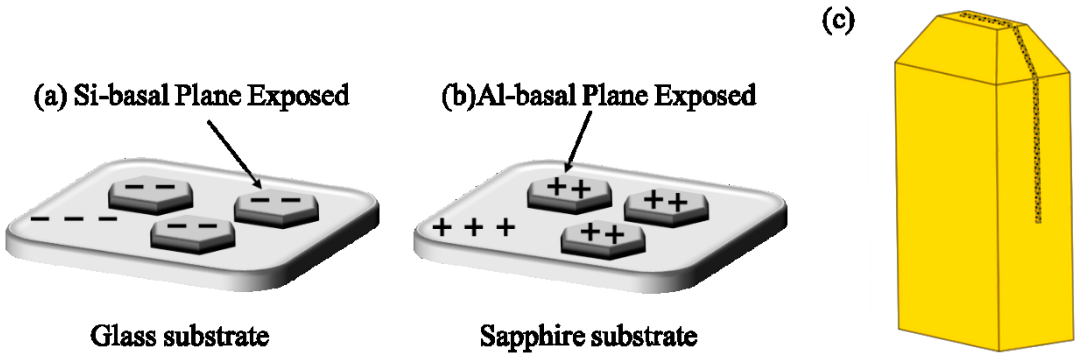

Figure 3.2 Schematics of preparing kaolinite (a) Si-basal plane, (b) Al-basal plane, and (c) edge surfaces.

3.2.1 Kaolinite basal planes

The microscopic glass slides (Fisher Scientific Inc.), the silica wafer (NanoFab, University of Alberta, CA) and the sapphire wafer (C-plane, (0001), University Wafer Inc.) were cut into 10-by-10-mm pieces. The glass slides, sapphire wafers and silica wafers were cleaned with piranha solution, composed of three volumes of sulfuric acid (H_2SO_4 96%) and one volume of hydrogen peroxide (H_2O_2 30%), for 30 min, followed by rinsing with large amounts of Milli-Q water, sonicating for 15 minutes in Milli-Q water, and blowing dry with ultra-high purity N_2 gas. It was expected that this process would remove the organic and inorganic contaminations on the substrates.

Two drops of the kaolinite suspension at pH 5 were put on the clean glass and sapphire substrates, which were placed on a ~70˚C hot plate to dry. The purpose of this technique was to expose the kaolinite Si-basal plane and Al-basal plane, respectively.

3.2.2 Kaolinite edge surfaces

The re-dispersed kaolinite suspension was pipetted onto a layer of hardened epoxy resin (Electron Microscopy Sciences, Hatfield, PA, USA), which was placed on a hot plate at about 120 ˚C. The kaolinite particles were expected to flatly and evenly spread over the resin surface in such way. Another layer of the epoxy resin was put on top of the dried kaolinite particles. The two layers of the epoxy resin and the kaolinite particles in the center together, formed a resin block with a sandwich structure. The resin block was trimmed by a trimmer (Leica EM TRIM2, Leica Microsystems Inc.) to create a tetragonal top surface and four trapezoid side faces as shown in Figure 3.2(c). The tetragonal top surface should be as small as possible to reduce the friction generated during the ultramicrotome cutting procedure. The trimmed resin block was then mounted as perpendicular as possible on the ultramicrotome (Leica EM UC7, Leica Microsystems Inc.) for cutting. After cutting with a diamond knife on the ultramicrotome, the resin block was rinsed with Milli-Q water and blown dry with high-pressure ultrapure N_2 gas to remove the remained flakes on the surface, and it was then glued on a clean glass substrate. Before being used in AFM force measurement, the resin block was put in a UV-ozone for five minutes, rinsed with a large amount of Milli-Q water, and blown dry with ultra-high purity N_2 gas to remove the organic contaminants.

3.3 Atomic force microscopy

3.3.1 AFM force measurement

An Atomic Force Microscope (Bruker Dimension Icon-PT, Bruker Corporation) was used to measure the interaction forces between the AFM tip and the kaolinite surfaces. Silica

nitride tips (DNP-10, Bruker AFM Probes, Bruker Nano Inc.) with a tip radius of about 20 nm were used in the research of kaolinite basal planes. Because the width of the edge surfaces is between 30 nm and 80 nm, silicon tips (SNL-10, Bruker AFM Probes, Bruker Nano Inc.) with a smaller tip radius of about 2 nm were used to study kaolinite edge surfaces. The spring constant of each cantilever was evaluated by the Thermal Tune Function provided in the NanoScope Software V8.15 (Bruker Corporation). Dimensional analysis of the probes was carried out on the SEM images of the probes.

The influence of pH on the Stern potentials of kaolinite surfaces was studied at pH 3, 5, 6, 8, and 10 in 10 mM KCl solutions. The effect of divalent cations were studied in 10 mM KCl solutions with different concentrations of Ca^{2+} and Mg^{2+} at pH 8 and 11, respectively.

In 10 mM KCl solution, the thickness of the electrostatic double-layer (κ^{-1}) is about 3.03 nm, which is much smaller than the thickness of kaolinite particle (see Figure 3.3), so the tip-substrate electrostatic double-layer would not overlap with the tip-kaolinite surface electrostatic double-layer[75]. When divalent cations were added into the 10 mM KCl background solutions, the thickness of the electrostatic double-layer would be compressed even more.

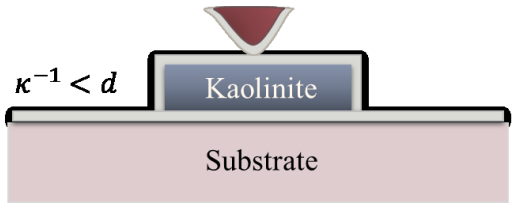

Figure 3.3 Illustration of the electric double layer (shown as grey thin layer) surrounding the AFM tip, kaolinite and substrate in electrolyte solutions with κ^{-1} less than the thickness (d) of the kaolinite particle.

Force measurements between the AFM tip and the sample surface were performed after the tip-solution-sample surface system was stabilized for 30 min. The topography image of the kaolinite surfaces was scanned and captured under contact mode by the Point and Shoot Function provided in the NanoScope Software V8.15, and then the interaction force curves were taken 5 times at each chosen location on this image. For each background solution condition, more than 500 force curves were taken at 3 ~ 4 different places on every sample to guarantee the reproducibility of the data. The measured force curves were fitted with theoretical DLVO force curves to derive the Stern potentials of kaolinite surfaces.

The raw force curves were Deflection Error-Z distance data, which were converted to Force-Separation distance curves by NanoScope Analysis Version 1.8 (Bruker Corporation). Baseline corrections of the force curves were also conducted before they are fitted with theoretical DLVO force curves.

3.3.2 AFM tip evaluation

The geometry of the AFM probes was obtained by analyzing the images of the probes (see Figure 3.4), which were captured by a Scanning Electron Microscope (SEM)/Mineral Liberation Analyzer (Quanta 250, FEI Company). The pyramid-shape probe was composed of a spherical apex and a conical tip.

The curvature and the conical angle of the spherical apex of the tip were determined by fitting it with a circle. The curvatures for Si_3N_4 tip and Si tip were determined to be about 60 nm and 30 nm, respectively. The conical angle (2β) of the Si_3N_4 tip and Si tip were around 40˚ and 35˚, respectively. SEM images were taken to check the status of the probe.

If they showed that the probe was worn or damaged after the force measurement, the experimental results obtained by this tip would not be used any further.

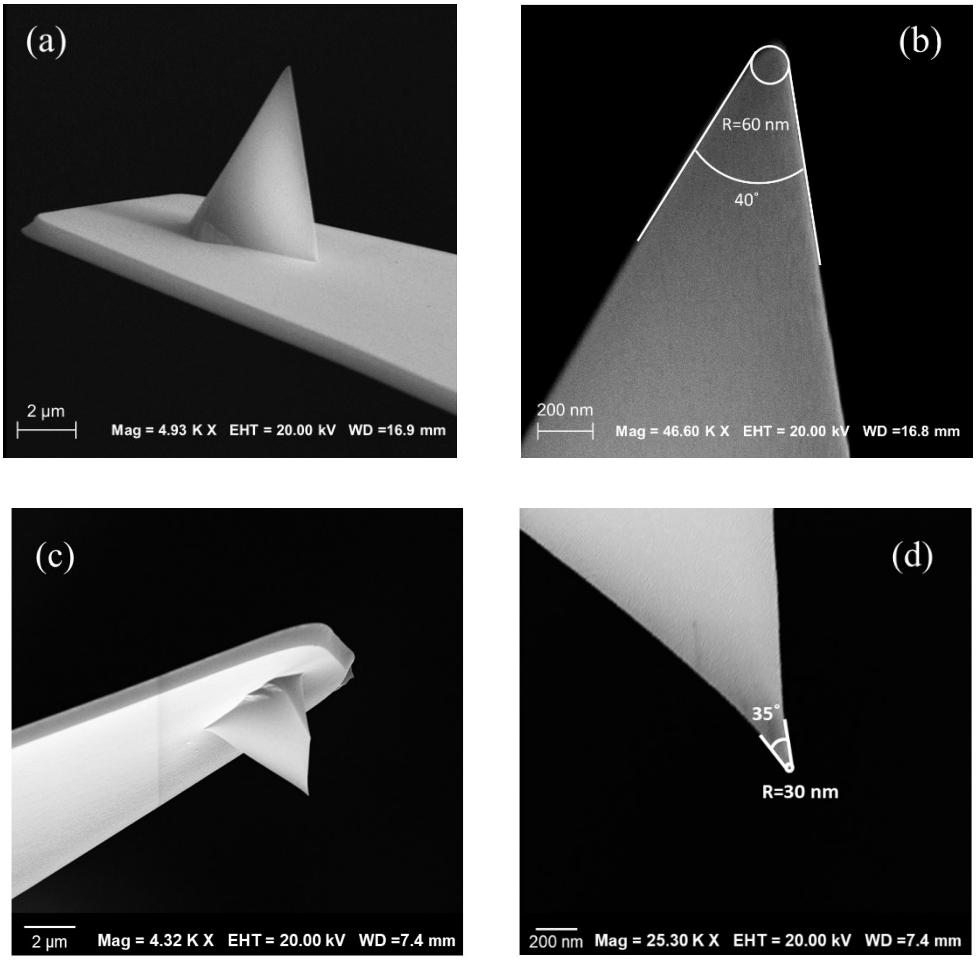

Figure 3.4 SEM images of the side view of (a) a cantilever with a DNP-10 AFM tip on top at low magnification, (b) DNP-10 AFM tip at high magnification, (c) cantilever with a SNL-10 AFM tip on top at low magnification, and (d) SNL-10 AFM tip at high magnification.

3.3.3 Atomic resolution imaging by AFM

Atomic resolution imaging was performed using a Dimension ICON-ScanAsyst AFM (Bruker Dimension Icon-PT, Bruker Corporation). Fastscan-C probes with a tip radius of

5 nm, a cantilever of 40 μm and a spring constant of 0.8 N/m were used. Kaolinite samples were rinsed with Milli-Q water and blown dry with ultra-pure N_2 gas to remove loosely attached particles. Kaolinite sample was immersed in background electrolyte solutions for 30 min before performing the AFM imaging. ScanAsyst mode with auto-control was first used to find a kaolinite particle firmly attached to the substrate. The tip was then withdrawn from the sample surface. After turning off the auto-control, the peak force engage setpoint was set as 0.04 V and the tip was engaged in contact with the kaolinite particle surface again. To improve the quality of images, scanning parameters were carefully adjusted after zoom-in on a kaolinite particle. To reduce the drift, the scan rate was increased to 2 Hz for 512 (Samples/Line) × 512 (Lines) data format. The obtained images were treated using NanoScope Analysis Version 1.8 (Bruker Corporation), and the image processing procedure was provided in Appendix A.

3.4 Theoretical model

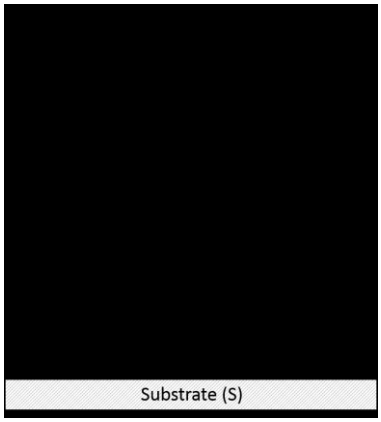

Figure 3.5 Schematic illustration of the AFM tip-flat surface system used in the theoretical calculation. Angles α and β are the geometrical angles for the spherical cap at the tip apex and the conical tip body, respectively, and $\alpha + \beta = 90°$; D refers to the separation between

the end of the tip apex and the surface of the substrate; L is the distance from the AFM tip to the substrate; R is the radius of the spherical cap at the tip apex; r is the radius of the tip at a given vertical position[40].

The geometry of the pyramidal-shape tips shown in Figure 3.5 can be reasonably approximated as a cone with a spherical cap at its apex as illustrated in Figure 3.5. The interaction force between an AFM tip and a flat sample surface is dominated by van der Waals force and electrostatic double-layer force, which is described by the classical DLVO theory[39].

The derivation of the DLVO theory that can be applicable to the AFM tip-flat substrate system was reported in the literature[40,49] and only the final equations are listed below:

$$F_{DLVO} = F_{vdw} + F_{edl} = F_{TS}^{S} + F_{TS}^{C} \tag{3.1}$$

van der Waals force:

$$F_{vdw} = \frac{A}{6}\left[\frac{(R+D)-2L_1}{L_1^2} - \frac{R-D}{D^2}\right] - \frac{A}{3\tan^2\alpha}\left(\frac{1.0}{L_1} + \frac{R\sin\alpha\tan\alpha - D - R(1-\cos\alpha)}{L_1^2}\right) \tag{3.2}$$

where A is the combined Hamaker constant[76] for the tip-solution-substrate system. Based on the Lifshitz theory[77], the nonretarded Hamaker constant for two macroscopic phases 1 and 2 interacting across a medium 3 is expressed by[78]:

$$A = \frac{3}{4}k_B T\left(\frac{\varepsilon_1-\varepsilon_3}{\varepsilon_1+\varepsilon_3}\right)\left(\frac{\varepsilon_2-\varepsilon_3}{\varepsilon_2+\varepsilon_3}\right) + \frac{3h\nu_e}{8\sqrt{2}}\frac{(n_1{}^2-n_3{}^2)(n_2{}^2-n_3{}^2)}{(n_1{}^2+n_3{}^2)^{1/2}(n_2{}^2+n_3{}^2)^{1/2}\{(n_1{}^2+n_3{}^2)^{1/2}+(n_2{}^2+n_3{}^2)^{1/2}\}} \tag{3.3}$$

where ε_1, ε_2, and ε_3 are the static dielectric constants of the three media; n_1, n_2, and n_3 are the refractive indexes for three media; k_B is the Boltzmann constant, 1.38×10^{-23}J/K; T

is the absolute temperature in Kelvin; h is the Planck's constant, 6.626×10^{-34} J·s; ν_e is the main electronic absorption frequency in the UV region, which is assumed to be the same ($3.0 \times 10^{15}\mathrm{s}^{-1}$) for all materials in this work.

Table 3.1 Values used to calculate the Hamaker constants.

Materials	Static Dielectric Constant ε	Refractive Index n	Hamaker Constant A
Silica[79]	3.82	1.448	
Water[79]	78.5	1.333	
Silicon nitride[79]	7.4	1.988	
Alumina[78]	10.1-11.6	1.753	
Silicon[78]	11.6	3.44	
Silicon nitride-water-silica wafer			2.01×10^{-20}J
Silicon nitride-water-silica basal plane of kaolinite			2.01×10^{-20}J
Silicon nitride-water-alumina basal plane of kaolinite			6.33×10^{-20}J
Silicon-water-silica wafer			4.33×10^{-20}J
Silicon (A_{11})[36]			1.36×10^{-19}
Kaolinite edge surface (A_{22})[57]			1.20×10^{-19}
Water (A_{33})[78]			3.70×10^{-20}
Silicon-water-edge surface of kaolinite			2.72×10^{-20}J

Due to the lack of the information of the dielectric constant and refractive index of kaolinite edge surface, the combined Hamaker constant for silicon-water-kaolinite edge surface was estimated by the following equation[78]:

$$A = (\sqrt{A_{11}} - \sqrt{A_{33}}) \times (\sqrt{A_{22}} - \sqrt{A_{33}}) \tag{3.4}$$

where, A_{11}, A_{22} and A_{33} refer to the Hamaker constants of individual medium 1, 2 and 3, respectively. In this case, A_{11}, A_{22} and A_{33} are the Hamaker constants of silicon, kaolinite edge surface and water, respectively.

All the values needed by the calculation of the Hamaker constants are listed in the above Table 3.1.

Electrostatic double-layer force:

For the case of constant surface potential boundary condition (BC):

$$F_{edl} = 4\pi\varepsilon_0\varepsilon\psi_T\psi_S(a_0e^{-\kappa D} - a_1e^{-\kappa L_1}) - 2\pi\varepsilon_0\varepsilon(\psi_T^2 + \psi_S^2)(a_2e^{-2\kappa D} - a_3e^{-2\kappa L_1}) + \frac{4\pi\varepsilon_0\varepsilon\kappa}{tan\,\alpha} \cdot \left\{b_1\psi_T\psi_S e^{-\kappa L_1} - b_2\frac{(\psi_T^2+\psi_S^2)}{2}e^{-2\kappa L_1}\right\} \tag{3.5}$$

For the case of constant surface charge density BC:

$$F_{edl} = \frac{4\pi}{\varepsilon_0\varepsilon\kappa^2}\sigma_T\sigma_S(a_0e^{-\kappa D} - a_1e^{-\kappa L_1}) + \frac{2\pi}{\varepsilon_0\varepsilon\kappa^2}(\sigma_T^2 + \sigma_S^2)(a_2e^{-2\kappa D} - a_3e^{-2\kappa L_1}) + \frac{4\pi}{\varepsilon_0\varepsilon\kappa\tan\alpha} \cdot \left\{b_1\sigma_T\sigma_S e^{-\kappa L_1} + b_2\frac{(\sigma_T^2+\sigma_S^2)}{2}e^{-2\kappa L_1}\right\} \tag{3.6}$$

Theoretically, the electrostatic double-layer force was derived under either the constant surface potential or the constant surface charge density BC. However, in reality, especially at a short distance, the electrical double-layer force would lie between the two conditions[28].

For the case that one surface is under constant surface potential condition and the other is under constant surface charge density condition, the mixed BC should be adopted to fit the measured force curves, and the equations[49] for this case are given as follows:

$$W_{edl}^{S} = \pi R\left[2\psi_s\sigma_T\int_D^{L_1}\operatorname{sech}(\kappa L)dL + \left(\frac{\sigma_T^2}{\varepsilon\varepsilon_0\kappa} - \varepsilon\varepsilon_0\kappa\psi_s^2\right)\times\int_D^{L_1}(\tanh(\kappa L)-1)dL\right] \quad (3.7)$$

$$W_{edl}^{C} = \frac{\pi b_3}{\tan\alpha}\left[2\psi_s\sigma_T\int_{L_1}^{\infty}\operatorname{sech}(\kappa L)dL + \left(\frac{\sigma_T^2}{\varepsilon\varepsilon_0\kappa} - \varepsilon\varepsilon_0\kappa\psi_s^2\right)\int_{L_1}^{\infty}(\tanh(\kappa L)-1)dL\right] +$$

$$\frac{\pi}{\tan\alpha}\left[2\psi_s\sigma_T\int_{L_1}^{\infty}\operatorname{sech}(\kappa L)LdL + \left(\frac{\sigma_T^2}{\varepsilon\varepsilon_0\kappa} - \varepsilon\varepsilon_0\kappa\psi_s^2\right)\int_{L_1}^{\infty}(\tanh(\kappa L)-1)LdL\right] \quad (3.8)$$

$$W_{edl}^{\psi-\sigma} = W_{edl}^{S} + W_{edl}^{C} \quad (3.9)$$

$$F_{edl}^{\psi-\sigma} = -\left(\frac{\partial W_{edl}^{\psi-\sigma}}{\partial D}\right) \quad (3.10)$$

where,

$L_1 = D + R(1-\cos\alpha)$, $a_0 = \kappa R - 1$, $a_1 = \kappa R\cos\alpha - 1$, $a_2 = a_0 + 0.5$, and $a_3 = a_1 + 0.5$

$$b_1 = \left[R\sin\alpha - \frac{D+R(1-\cos\alpha)}{\tan\alpha}\right] + \frac{1}{\tan\alpha}\cdot\left[\left(L_1 + \frac{1}{\kappa}\right)\right]$$

$$b_2 = \left[R\sin\alpha - \frac{D+R(1-\cos\alpha)}{\tan\alpha}\right] + \frac{1}{\tan\alpha}\cdot\left[\left(L_1 + \frac{1}{2\kappa}\right)\right]$$

$$b_3 = R\sin\alpha\tan\alpha - L_1$$

Here, superscripts S and C refer to the spherical cap of the tip apex and the conical tip body, respectively; subscripts S and T refer to the substrate and the AFM tip, respectively; ε and ε_0 are dielectric constant of the medium and the permittivity of vacuum, respectively; e is the electronic charge, 1.602×10^{-19}C; ψ is the surface potential; σ is the surface charge density; κ is the reciprocal of the Debye length[80], which is a characteristic parameter describing the thickness of EDL or decay of the electric potential:

$$\kappa^{-1} = \left(\frac{\varepsilon\varepsilon_0 k_B T}{\sum_i n_{i0} e^2 {z_i}^2}\right)^{1/2} \tag{3.11}$$

where n_{i0} is bulk concentration of electrolyte i, ions/m^3; z_i is the valence of ion i.

The surface potential and the surface charge density are linked to each other by the Grahame equation[81]:

$$\sigma = \sqrt{8 c_0 \varepsilon\varepsilon_0 k_B T}\sinh\left(\frac{e\psi}{2k_B T}\right) \tag{3.12}$$

where c_0 is the bulk concentration of the salt; k_B is the Boltzmann constant, 1.38×10^{-23}J/K; and T is the absolute temperature.

Chapter 4 Determination of Stern Potentials of Kaolinite Surfaces: Effect of Divalent Cations and Solution pH

4.1 Introduction

In the processing of valuable resources, such as flotation or tailings treatment, divalent cations should be removed to promote flotation efficiency or added to reclaim more process water since they can alter the surface potentials of clay minerals. The concentration of divalent cations is essential in their applications in industry. In real systems, a much lower dosage of divalent cations than the critical coagulation concentration is enough to achieve effective coagulation, as the specific adsorption nature of the corresponding monohydroxyl ions would lead to charge reversal of clay particles. However, the impact of divalent cations on the Stern potentials of kaolinite still lacks investigation. Therefore, in this work, we focused on the anisotropic surface properties of kaolinite particles and took a deeper look at the potential determining abilities of different divalent cations by AFM force measurements. The interaction forces between the AFM tip and distinct kaolinite basal planes in 10 mM KCl solutions containing Ca^{2+} and Mg^{2+} were fitted using DLVO theory to derive the Stern potentials of different kaolinite surfaces. In addition, we explored the mechanisms of divalent cations adsorbing on different kaolinite surfaces based on the experimental results, aiming to provide clear insights into the colloidal behavior of kaolinite that governs its vast applications in lab research and industry.

4.2 Results and discussion

4.2.1 AFM tip calibration

To obtain the Stern potential of selected kaolinite surface through the measured interaction force between kaolinite surface and AFM tip, we first examined the Stern potential carried by the AFM tip. Since the Stern potentials of silica wafer in 10 mM KCl solutions at different pH environments were well studied and showed good consistency[82–84], silica wafer was thus used to obtain the Stern potential of the AFM tip. Stern potentials of silica wafer in 10 mM KCl solutions with divalent cations have not been investigated. Therefore, the zeta potentials of the silica wafer (see Figure 4.1) measured by SurPASS Electrokinetic Analyzer (Anton Paar USA Inc.) using streaming potential method were adopted to calibrate the AFM tips.

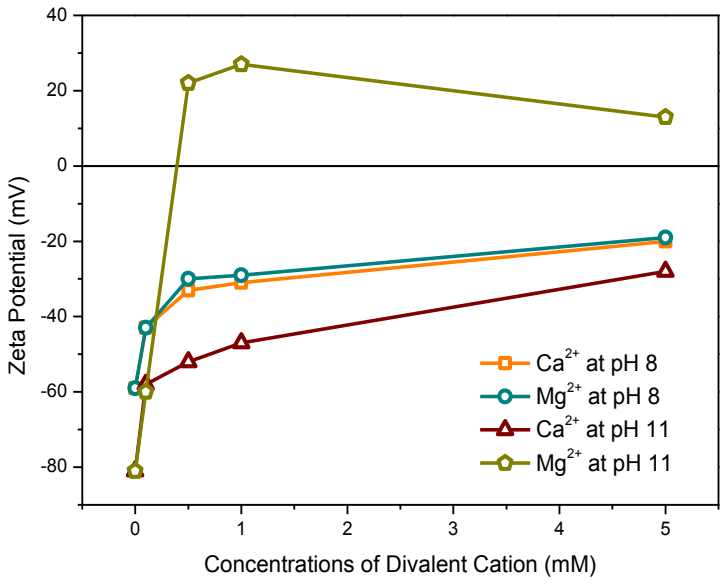

Figure 4.1 Zeta Potential of silica wafer in 10 mM KCl solutions at pH 8 and 11 with varying concentrations of divalent cations (Ca^{2+} and Mg^{2+}, respectively) determined using the streaming potential method.

It can be seen in Figure 4.1 that the zeta potential of silica wafer is -52 mV in 10 mM KCl solution at pH 8, which is slightly lower in magnitude than the Stern potential of silica wafer (-59 mV) under this condition. This is because the Stern potential was measured at a closer distance to the solid surface than the zeta potential. The zeta potential of the silica wafer was determined to be -43 mV when 0.1 mM Ca^{2+} was added into the solution, and it reached to -33 mV and -31 mV at 0.5 mM and 1 mM additions of Ca^{2+}, respectively. The zeta potential of silica wafer changed considerably to -20 mV when the concentration of Ca^{2+} was increased to 5 mV. The zeta potentials of silica wafer in KCl solutions with the addition of Mg^{2+} were found to be very close to those with the addition of Ca^{2+}.

Yan et al.[85] reported that the difference between the Stern potential and the zeta potential became smaller when the electrostatic double-layer was further compressed by adding higher concentrations of divalent cations. When 0.1, 0.5, 1 and 5 mM divalent cations were added into the 10 mM KCl solution, the Debye length of a solid surface was compressed from 3.03 nm to 2.99, 2.83, 2.66, and 1.92 nm, respectively. When the electrostatic double-layer was further compressed by adding higher concentrations of divalent cations, the difference between the Stern potential and the zeta potential became smaller. Therefore, it is feasible to use the zeta potentials of silica wafer to evaluate the Stern potentials of the AFM tips when divalent cations are added to the KCl solution.

Their conclusion was also confirmed by comparing the measured zeta potentials (using ZetaSizer Nano) of Si_3N_4 nano particles with the Stern potentials of AFM Si_3N_4 tip calibrated by AFM force measurement using silica wafer (see Figure 4.2).

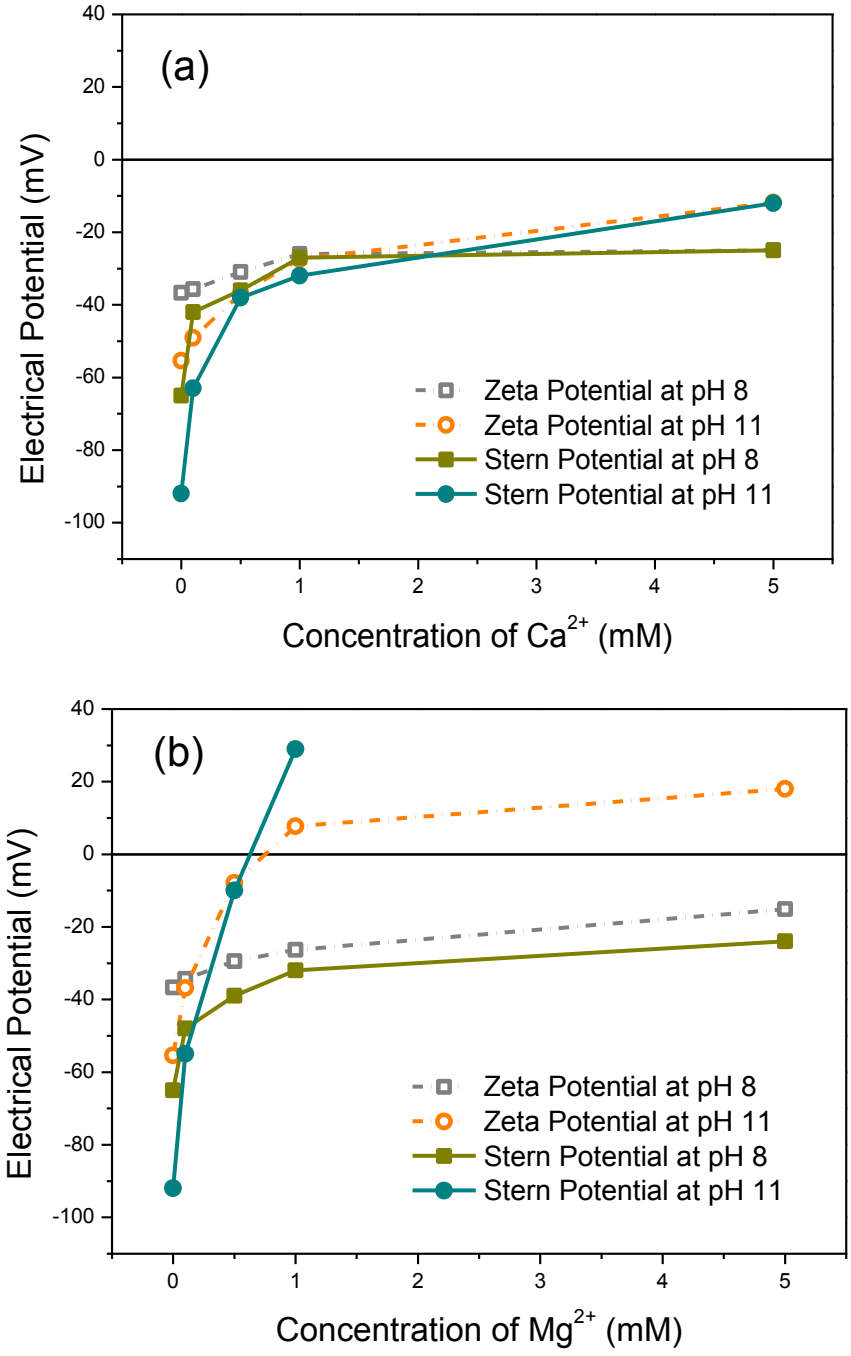

Figure 4.2 Comparison of the zeta potential of Si_3N_4 nano particles with the Stern potential of AFM Si_3N_4 tip in 10 mM KCl solutions at pH 8 and 11 containing different concentrations of (a) Ca^{2+} and (b) Mg^{2+}.

In this research, pH 3 was used instead of pH 4 to avoid the PZC of silica nitride tip, which was reported[86] to be near pH 4. The measured force curves of the interaction between the AFM tips and the silica wafer (see Figure 4.3 and Figure 4.4 for silicon nitride tip and silicon tip, respectively) were fitted with the theoretical force curves calculated based on the classical DLVO theory, which were computed using MATLAB (The MathWorks Inc.), to derive the Stern potentials of the AFM tips. The experimental data fitted well with the theoretical data at the separation distance > 3 nm, but they deviated at a very short separation. This phenomenon was also observed in the investigation of the charging characteristics of different kaolinite surfaces, and it is probably a consequence of the surface roughness and the repulsive, short-distance and non-DLVO hydration force between the AFM tip and the substrate/sample surface, which was not taken into consideration in this study. More details about the error analysis can be found in Appendix B. Therefore, the experimental force curves were always higher than the corresponding DLVO force curves when the separation was less than 3 nm. Also, the "jump-to-contact" point can be observed at the separation distance < 2 nm.

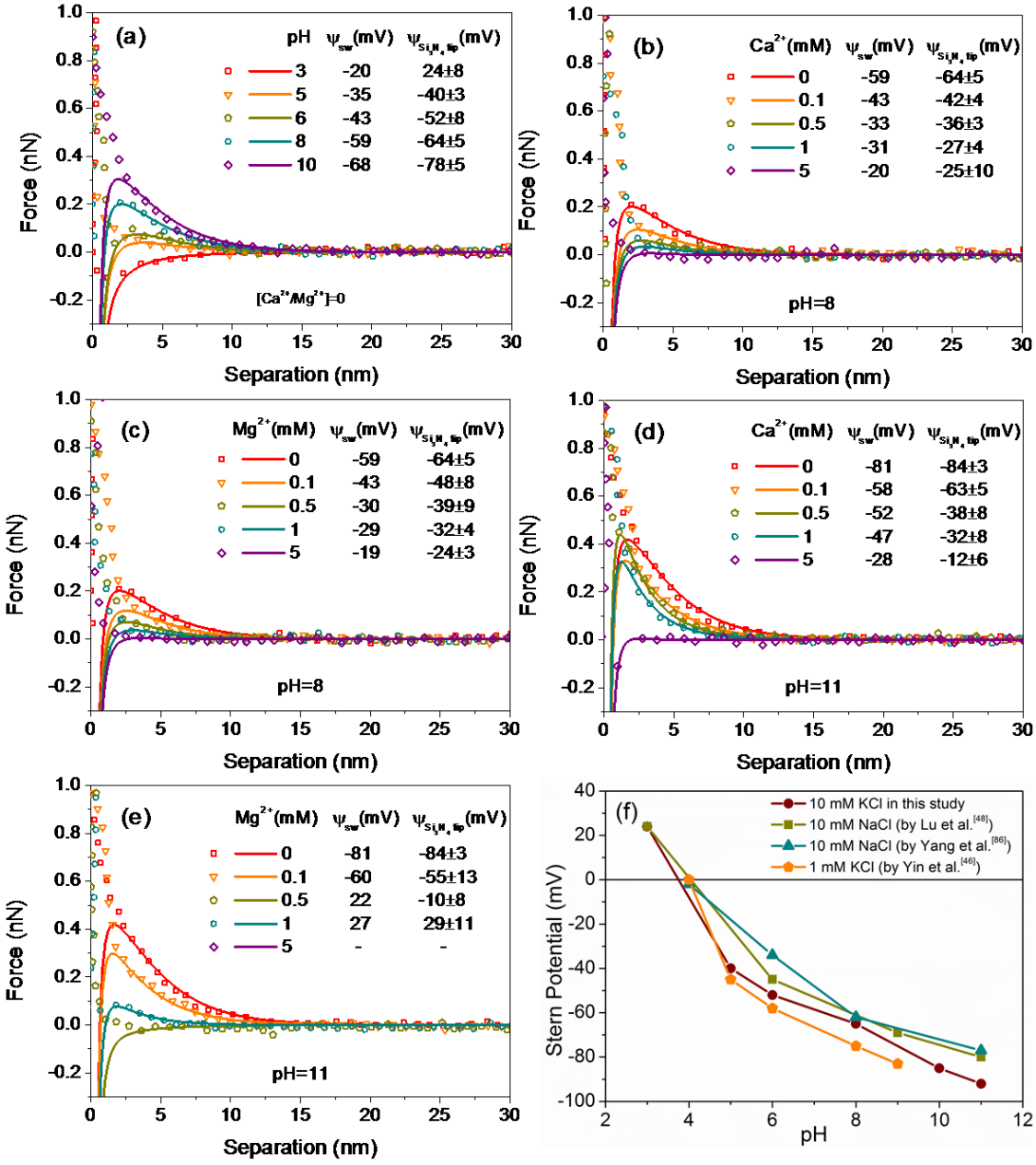

Figure 4.3 Interaction forces between the AFM Si_3N_4 tip and the silica wafer in 10 mM KCl solutions (a) at different pH, (b) at pH 8 containing different concentrations of Ca^{2+}, (c) at pH 8 containing different concentrations of Mg^{2+}, (d) at pH 11 containing different concentrations of Ca^{2+}, and (e) at pH 11 containing different concentrations of Mg^{2+}; and

(f) Comparison of the Stern potentials of the AFM Si_3N_4 tip obtained in this this study with those reported in literature.

In a liquid medium, the charging of a surface mainly occurs in three different ways[63,80]:

(1) by surface ionization or dissociation (which is the dominant charging mechanism for oxides, e.g. SiO_2, TiO_2, Al_2O_3);

(2) by adsorption or binding of ions from solution (such as ion exchange);

(3) by crystal lattice defects (e.g. isomorphic substitution for clay minerals).

When two surfaces approach each other, if the surface charge comes from irreversible ion adsorption, dissociation of strong surface groups, or lattice defects, the surface charge density, which is independent of the surface potential and finally of the separation distance, remains constant during the approach; if the surface charging mechanism is dominated by reversible ion adsorption, the surface potential can be assumed constant because the adsorption-desorption equilibrium responds immediately to every configuration of the interacting surfaces[87]. However, constant charge or constant potential are ideal and extreme cases, and the interaction force between two interacting surfaces in reality would lie in between.

The charging mechanism for clean silica wafer (which carries many hydroxyl groups in aqueous solutions) in a solution is chemical adsorption of ions[88] and the surface takes up or releases a proton according to the solution pH:

$SiOH_2^+ \rightleftharpoons SiOH + H^+$ (takes place at extremely low pH < 3)

$SiOH \rightleftharpoons SiO^- + H^+$

and

$SiO^- + M^+ \rightleftharpoons SiOM$ (can be adapted for multivalent cations being added into the solution)

Therefore, the silica wafer in inert electrolyte solutions (KCl solution in this case) is considered to be a constant potential surface. Because silicon nitride is prone to oxidize[34] towards SiO_2 and the change of its surface charge according to solution pH is due to the oxidization at its surface[81], it is reasonable to assume the surface potential of AFM Si_3N_4 tip is constant. Consequently, in Figure 4.3, DLVO force curves calculated by constant surface potential equation were used to fit the experimental data. The determined Stern potentials of Si_3N_4 tip are reported in Figure 4.3 (f), showing good agreement with literature values[49,85,86,89].

When Ca^{2+} and Mg^{2+} are added into the 10 mM KCl solution, the adsorption mechanisms of metal cations on oxide/clay surface in aqueous solutions mainly consist of: electrostatic attraction and surface complexation or specific adsorption at the solid-solution interface. The adsorption of metal ions at the solid-solution interface is highly pH-dependent. In pH 8 KCl solutions, there is no formation of $Ca(OH)^+$ and very few $Mg(OH)^+$, so there is almost no specific adsorption of metal cations on the solid surface[63,90]. However, the amphoteric SOH surface groups (where S refers to surface Si or Al atoms) on oxide or clay surfaces can form outer-sphere surface complexes with metal cations[91], which can be expressed with the following equation: $\equiv \mathrm{SOH} + \mathrm{M(H_2O)_6}^{2+} \leftrightarrow \mathrm{SO(H_2O)M(H_2O)_5}^{+} + \mathrm{H}^+$, (where M represents Ca or Mg). The strong surface complexes had a significant effect on the Stern potential of oxide/clay surface, which also impacted the selection of the

equation used in the fitting process. A clean silica wafer, which has many hydroxyl groups on its surface, is greatly affected by metal cations. As a consequence, the interaction force curves between the silica wafer and the AFM tip were better fitted with the mixed BC equation rather than the constant surface potential equation when divalent cations were added into the KCl solution.

At pH 11, there were more and more $Ca(OH)^+$ and $Mg(OH)^+$ as higher concentration of Ca^{2+} and Mg^{2+} were added to the KCl solutions. According to the speciation diagram (see Figure C1 in Appendix C), $Ca(OH)^+$ starts to be present at about pH 10.3 and keeps increasing as solution pH increases to 11, however, the first-order metal hydroxyl species of magnesium starts to exist at near pH 6 and reaches its peak at pH 10, and then starts to form metal hydroxide precipitates[90]. The magnesium hydroxide precipitates at pH 11 would disturb the laser deflection signal, hindering the force measurements when 5 mM Mg^{2+} was added into the background electrolyte at pH 11. As more and more irreversible specific adsorption of first-order metal hydroxyl species occurred on the silica wafer, the data became better described by the constant surface charge density equation instead of the mixed BC equation.

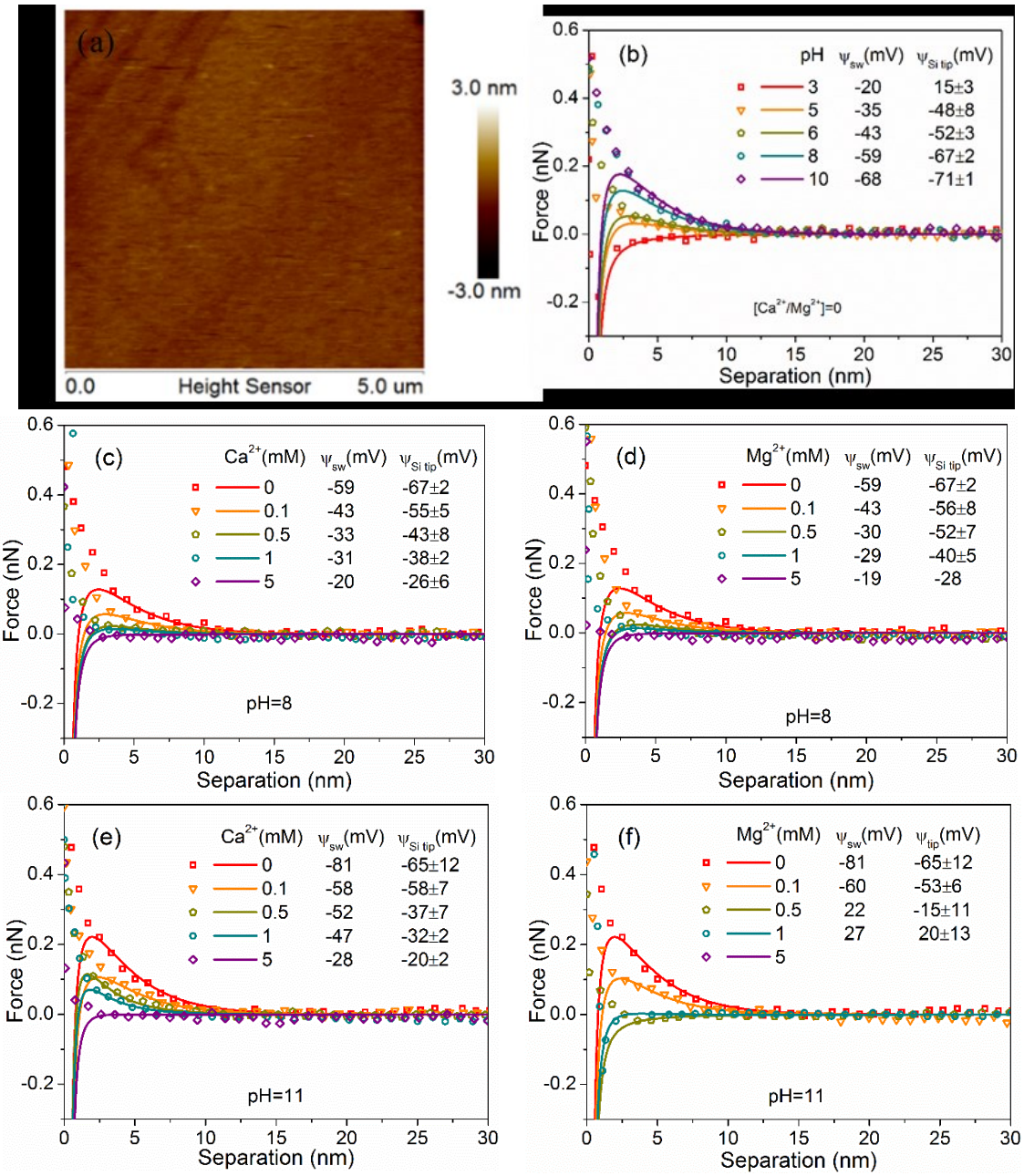

Figure 4.4 (a) Representative AFM image of a silica wafer surface; and typical interaction forces (solid lines represent theoretical DLVO forces, open symbols represent experimental data) between the AFM Si tip and the silica wafer in 10 mM KCl solutions (b) at different pH, (c) at pH 8 containing different concentrations of Ca^{2+}, (d) at pH 8

containing different concentrations of Mg^{2+}, (e) at pH 11 containing different concentrations of Ca^{2+}, and (f) at pH 11 containing different concentrations of Mg^{2+}.

Figure 4.4 (a) shows a representative image of a silica wafer surface used for colloidal force measurements, and the root-mean square roughness (Rq) of the silica wafer was 0.22 nm over a 25.0 μm^2 area. The results in Figure 4.4 (b) showed that the AFM Si tip was positively charged at pH 3, and negatively charged at pH 5-10, which means that the PZC of silicon tip was about pH 3 in 10 mM KCl solutions. This conclusion is consistent with reported PZC of silicon powder, which was pH 2.8[92] in 10 mM KNO_3 solutions.

For 10 mM KCl solutions, experimental force curves were found to be better fitted by the mixed BC equation than the constant surface potential equation. The derived Stern potentials of silicon tip were also different from those of silica wafer. These two findings indicated that silicon did not carry a constant surface potential like silica, which is probably because silicon was not fully oxidized to SiO_2 or due to the semiconductor nature of silicon. Under the effect of Ca^{2+} and Mg^{2+}, the equation adopted in the fitting process gradually changed from mixed BC equation to constant surface charge density equation. The change of fitting equation is based on the corresponding charging mechanisms of the tip and the silica wafer. At pH 8, Ca^{2+} and Mg^{2+} would form surface complex with the Si-OH groups on tip and silica wafer surfaces. However, at pH 11, the first-order metal hydroxyl species of calcium and magnesium ions specifically adsorbed on the Si-OH groups. When the concentration of calcium and magnesium ions were increased to be higher than 0.1 mM, more specific adsorption happened, and caused both tip and silica wafer surfaces to carry constant surface charges.

4.2.2 Characterization of kaolinite samples

4.2.2.1 Samples of kaolinite basal planes

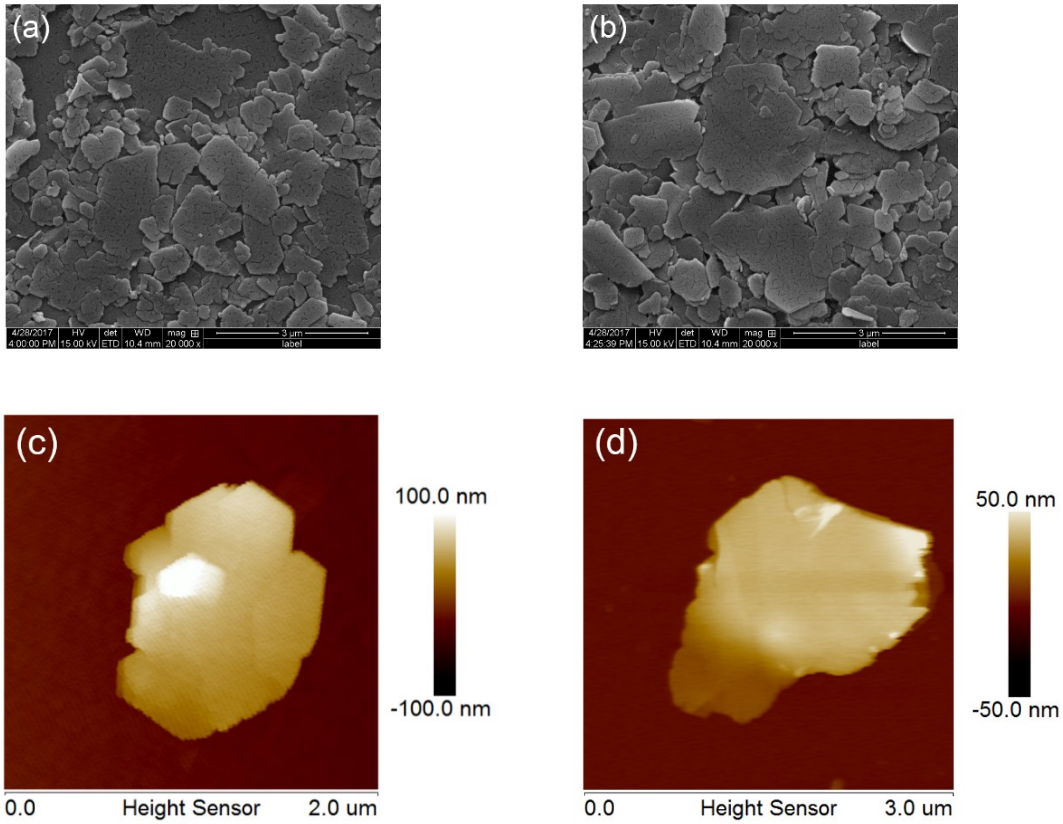

Figure 4.5 SEM images of kaolinite particles deposited on (a) glass substrate and (b) sapphire substrate after drying on a hot plate; AFM images of kaolinite particles deposited on (c) glass substrate and (d) sapphire substrate, after the substrate was rinsed with Milli-Q water and blown dry.

To obtain accurate and reproducible AFM force curves, it is vital to know that the measurements are performed on the right basal surface of kaolinite particle, and that the surfaces are smooth enough (surface roughness less than 1 nm). SEM images of the substrates with deposited kaolinite particles show that the kaolinite basal planes are very

flat (see images (a) and (b) in Figure 4.5), so they can orderly stack layer by layer, with a negatively charged kaolinite Si-basal plane of one kaolinite particle attached to the positively charged kaolinite Al-basal plane of another kaolinite particle. Finally, the positively charged Al-basal plane of the last layer of kaolinite particles will attach to the negatively charged glass substrate, so that the top layer surfaces would be the Si-basal planes of kaolinite particles, vice versa, when kaolinite particles are deposited on a positively charged sapphire substrate, the Al-basal planes of kaolinite particles are exposed at the top layer. It can be seen from the images that the exposed kaolinite basal planes are flat enough for AFM force measurement, which are confirmed by the AFM images shown in Figures 4.5 (c) and 4.5 (d). The root-mean-square roughness (Rq) of selected locations on both imaged kaolinite particles deposited on glass substrate and sapphire substrate was determined by AFM to be lower than 1 nm.

Because super-fine particles are loosely attached to the substrate, they need to be rinsed off by large amounts of Milli-Q water before the AFM force measurements. It can be seen from Figures 4.5 (c) and 4.5 (d) that most of the particles that can stay on the substrate after rinsing, and especially after scanning by AFM tip, are 1-2 μm in size because they have a larger contact area with the substrate, which can provide more electrostatic attraction between the kaolinite particles and the substrate. Micron size particles are also better than nano size particles for AFM force measurement, because the interaction force between the AFM tip and the kaolinite surfaces would be less affected by the substrate.

To make sure the opposite basal surfaces of kaolinite were exposed on glass substrate and sapphire substrate, respectively, interaction forces were measured between the AFM tip

and the particles sitting on the two substrates in 10 mM KCl solution of pH 5, as shown in Figure 4.6.

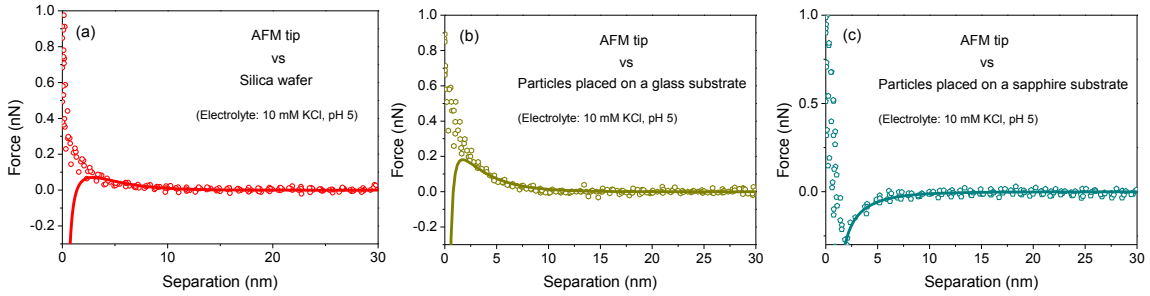

Figure 4.6 Interaction forces between an AFM tip and silica wafer (a), kaolinite particles sitting on a glass substrate (b), and particles sitting on a sapphire substrate (c) in 10 mM KCl solutions of pH 5 (open symbols represent experimental data, and solid lines represent theoretical DLVO forces).

Using a SurPASS Electrokinetic Analyzer (Anton Paar USA Inc.), zeta potential of silica wafer in 10 mM KCl solution of pH 5 was determined to be -32 mV. The repulsive interaction forces between silica wafer and the *AFM* tip shown in Figure 4.6 (a) mean that the *AFM* tip is negatively charged. As repulsive forces were obtained between the negatively charged tip and the kaolinite particles attaching to the glass substrate, the negatively charged Si-basal plane surfaces were obtained. In contrast, the attractive forces shown in Figure 4.6 (c) indicate a positively charged Al-basal plane on the other side of kaolinite particles was exposed on the sapphire substrate as anticipated.

4.2.2.2 Sample of kaolinite edge surfaces

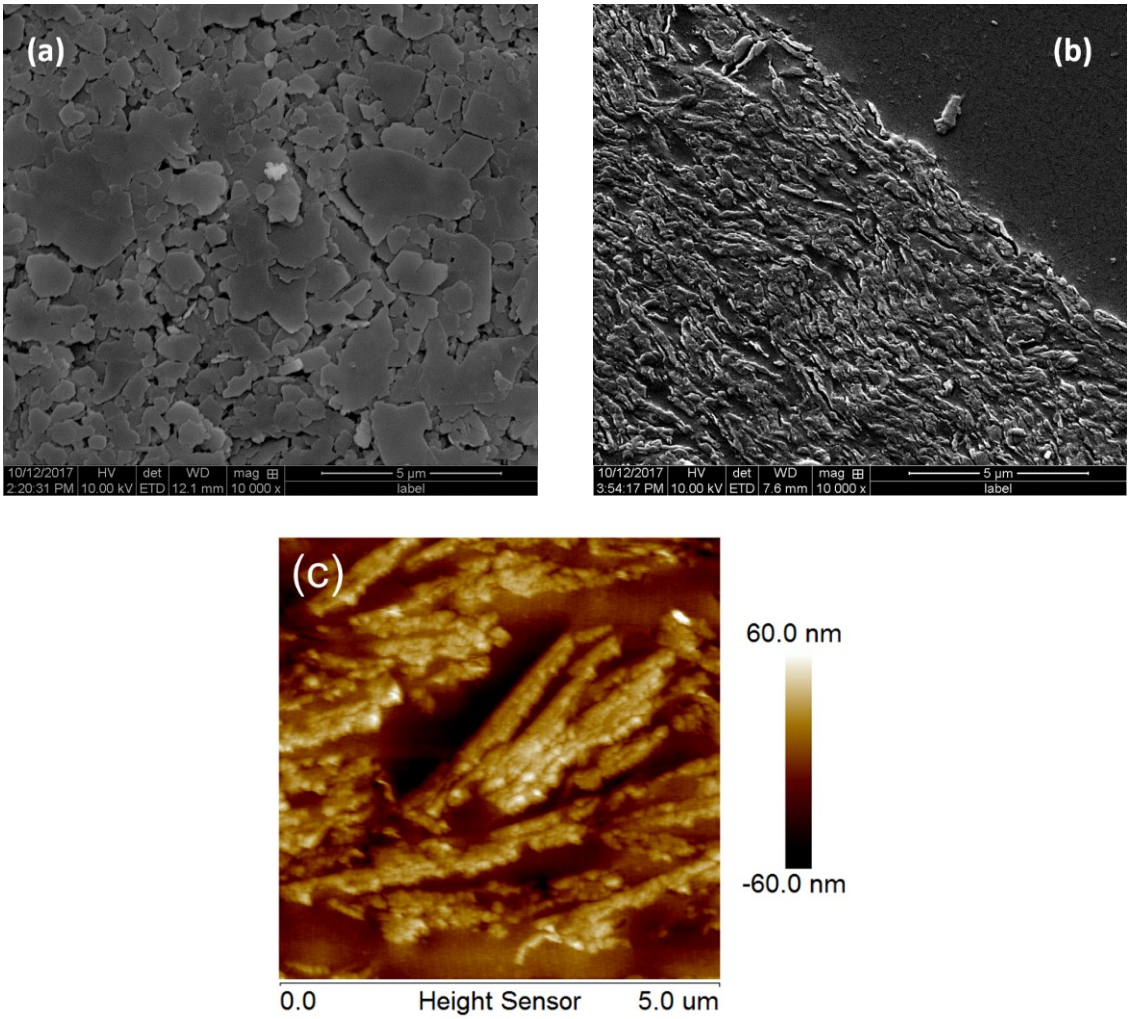

Figure 4.7 SEM images of (a) kaolinite particles deposited on the resin surface, and (b) kaolinite edge surfaces prepared by ultramicrotome cutting technique; and (c) AFM image of kaolinite edge surfaces.

The SEM imaging of kaolinite particles deposited on the resin surface (see Figure 4.7 (a)) shows that most of the particles lie flatly and orderly on the resin surface with kaolinite basal planes facing up. Therefore, mainly the kaolinite edge surfaces will be exposed after the resin block sandwiched with kaolinite particles in the middle being cut by

ultramicrotome. The aspect ratio of the kaolinite surfaces seen in Figure 4.7 (b) is much higher than the aspect ratio of kaolinite surfaces seen in Figure 4.7 (a), which proves that the edge surfaces of kaolinite particles have been successfully prepared.

Surface roughness is a vital parameter for acquiring accurate and reproducible data from AFM force measurements. After being cut by ultramicrotome, the surface of the resin block sandwiched with kaolinite particles in the middle was imaged by AFM and shown in Figure 4.7 (c). The Rq of the resin surface after cutting is less than 1 nm. The whole image Rq of Figure 4.7 (c) is 18.3 nm over 25 μm^2, and the Rq values of local parts vary between 1 to 2 nm, which means the edge surface is smooth enough for nanoscale study on the charging properties of kaolinite edge surfaces.

4.2.3 Effect of divalent cations on Stern potential of kaolinite Si-basal planes

AFM images were taken before and after the force measurements to make sure the kaolinite particles were still attached to the substrate. If the particles were no longer attached onto the substrate after the force measurements, the force curves taken on those particles would not be used in the following fitting process.

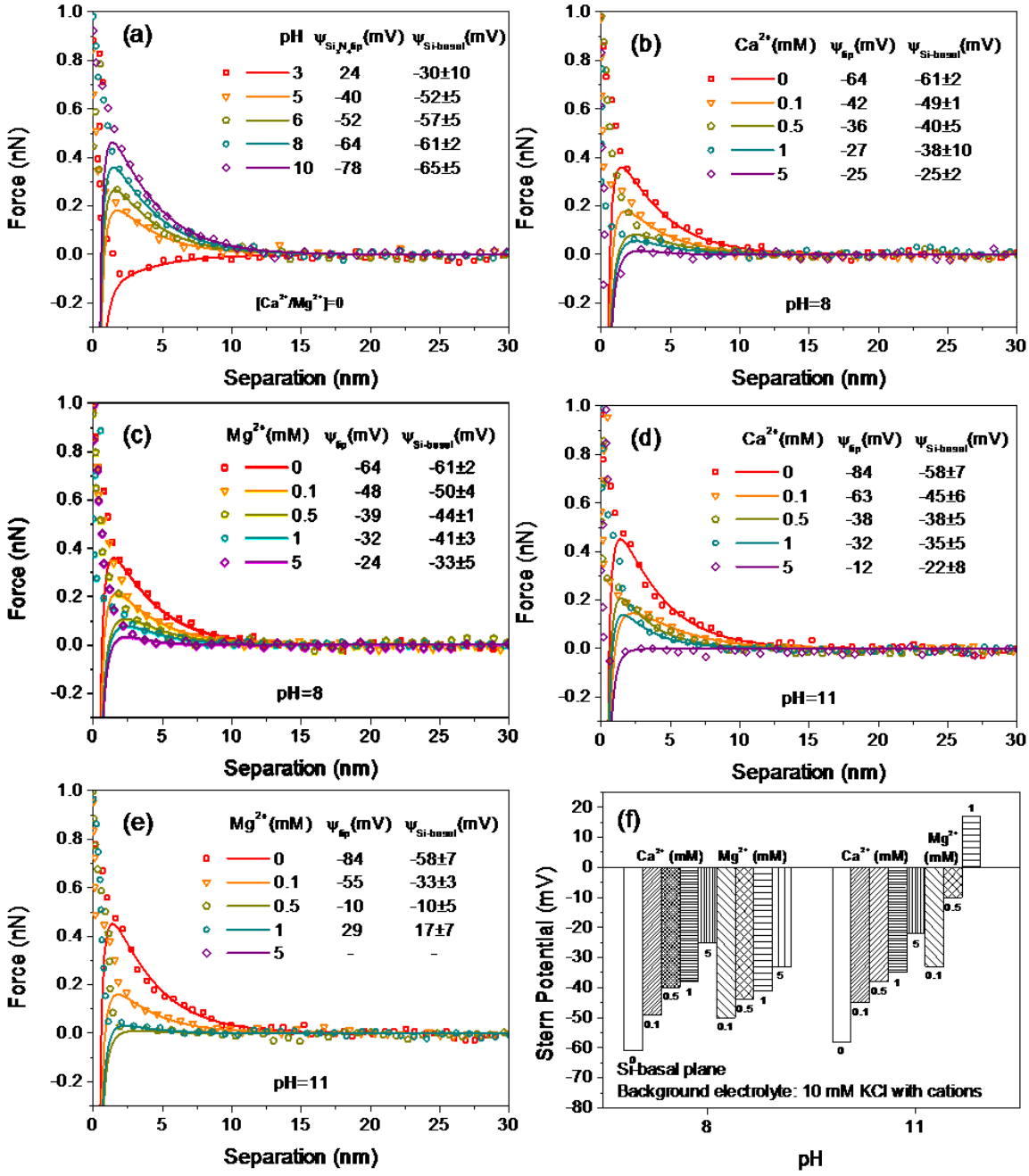

Figure 4.8 Interaction forces between the AFM Si_3N_4 tip and the kaolinite Si-basal plane in 10 mM KCl solutions (a) at different pH, (b) at pH 8 containing different concentrations of Ca^{2+}, (c) at pH 8 containing different concentrations of Mg^{2+}, (d) at pH 11 containing different concentrations of Ca^{2+}, and (e) at pH 11 containing different concentrations of

Mg^{2+}; and (f) Summary of the Stern potential of kaolinite Si-basal plane at pH 8 and 11 in 10 mM KCl solutions containing different concentrations of Ca^{2+} and Mg^{2+}.

Typical approaching force curves between AFM tip and kaolinite Si-basal plane in 10 mM KCl solution under various pH environments are shown in Figure 4.8 (a). The siloxane surface of kaolinite carries constant surface charge[20] because: 1) the surface charge of the siloxane surface mainly arises from isomorphic substitution, which leads to a permanent-negative charge; and 2) the hydrolysis of siloxane bonds is slow unless at extremely high pH. Therefore, a mix BC equation was applied to fit the experimental forces between the AFM Si_3N_4 tip with a constant surface potential and the kaolinite siloxane basal plane with a constant surface charge. For kaolinite Si-basal plane, repulsive interactions were found from pH 5 to pH 10, and the attractive interaction force occurred at pH 3 was attributed to the positively charged AFM Si_3N_4 tip under this condition. Therefore, kaolinite Si-basal plane carried negative charges from pH 3 to pH 10 in 10 mM KCl solutions. Moreover, because the Stern potentials of Si-basal plane changed dramatically at pH 3, the PZC of the siloxane surface of kaolinite was determined to be below, and near pH 3. According to the results in this study, the Stern potential of kaolinite siloxane surface almost did not change except at pH 3, which proves that the Si-basal plane of kaolinite carries a permanent surface charge that is negative and pH-insensitive[20].

At pH 8, 10 mM KCl solutions with various concentrations of divalent cations (0, 0.1, 0.5, 1, and 5 mM) were used as the background electrolytes. The interaction forces between AFM tip and kaolinite Si-basal plane were measured and shown in Figures 4.8 (b) and (c). The long-range repulsion was found in all conditions but was depressed with the increasing addition of divalent cations. When the concentration of Ca^{2+} or Mg^{2+} was increased to 5

mM, the interaction force was almost negligible, yet still repulsive. According to the Stern potentials, kaolinite Si-basal plane was found to be relatively less affected by the divalent cations compared to the silica wafer because the siloxane groups on this basal plane are hard to be hydrolyzed into ≡ SiOH, thus they are harder to form surface complexes with metal cations. Hence, the decrease of the Stern potentials of kaolinite Si-basal plane with the increase of divalent cation concentrations is attributed to the increasing electrostatic interaction between the negatively charged basal plane and the divalent cations. When the concentration of metal cations was increased to 5 mM, the local concentration of metal cations on the surface became as high as $[M^{2+}]_0 \approx 5 \times 10^{-3} e^{+200/25.7} \approx 12M$[80]. At such high surface concentration, divalent ions can chemically bind to negative surface sites[80], therefore considerably lowering the Stern potential of kaolinite Si-basal plane. Comparing Figures 4.8 (b) and (c), Ca^{2+} and Mg^{2+} have similar magnitude of effect on kaolinite Si-basal plane.

At pH 11, when specific adsorption of $Ca(OH)^+$ and $Mg(OH)^+$ on kaolinite Si-basal plane becomes more and more significant as the increase of initial divalent cation concentration, the experimental force curves should be fitted by the theoretical DLVO force curves calculated under constant charge density. Charge reversal was found at 1 mM Mg^{2+} addition, but not with any concentrations of Ca^{2+}, indicating a stronger impact of Mg^{2+} than Ca^{2+} at pH 11. This phenomenon was also observed by Gan et al.[90] on their investigation of the impact of divalent cations on the zeta potential of quartz. In the sulfonate flotation, at pH 11, the flotation recovery of sulfonate in the presence of 0.1 mM magnesium ions could reach 100%, while the flotation recovery was only about 20% with the same concentration of calcium ions[31].

According to the speciation diagram for 1 mM Ca^{2+} and Mg^{2+} (see Figure C1 in Appendix C), the concentration of $Ca(OH)^{+}$ and $Mg(OH)^{+}$ are both about 10^{-5} mol/L at pH 11. However, the hydroxide precipitate amounts of Ca and Mg vary a lot, which are 10^{-8} mol/L and 10^{-5} mol/L, respectively. Therefore, the difference between the impact of Ca^{2+} and Mg^{2+} at pH 11 is probably caused by the magnesium hydroxide precipitate on kaolinite Si-basal plane. For the Stern potential of kaolinite basal plane to reverse sign by Mg^{2+} addition, the suggested mechanism involves nucleation and growth of magnesium hydroxide precipitate at the basal surfaces. Following the formation of the precipitate, the basal surfaces of kaolinite are postulated to have the electrokinetic features of magnesium hydroxide[93], and this would result in more charge in the Stern layer[94].

$Mg(OH)_2$ was found to strongly adsorb on the quartz surfaces by Gan et al.[90], because their XPS results of Mg adsorbed on the glass slide at pH 10.9 before and after rinsing showed that the surface atomic concentration of Mg still remained high after rinsing.

4.2.4 Effect of divalent cations on Stern potential of kaolinite Al-basal planes

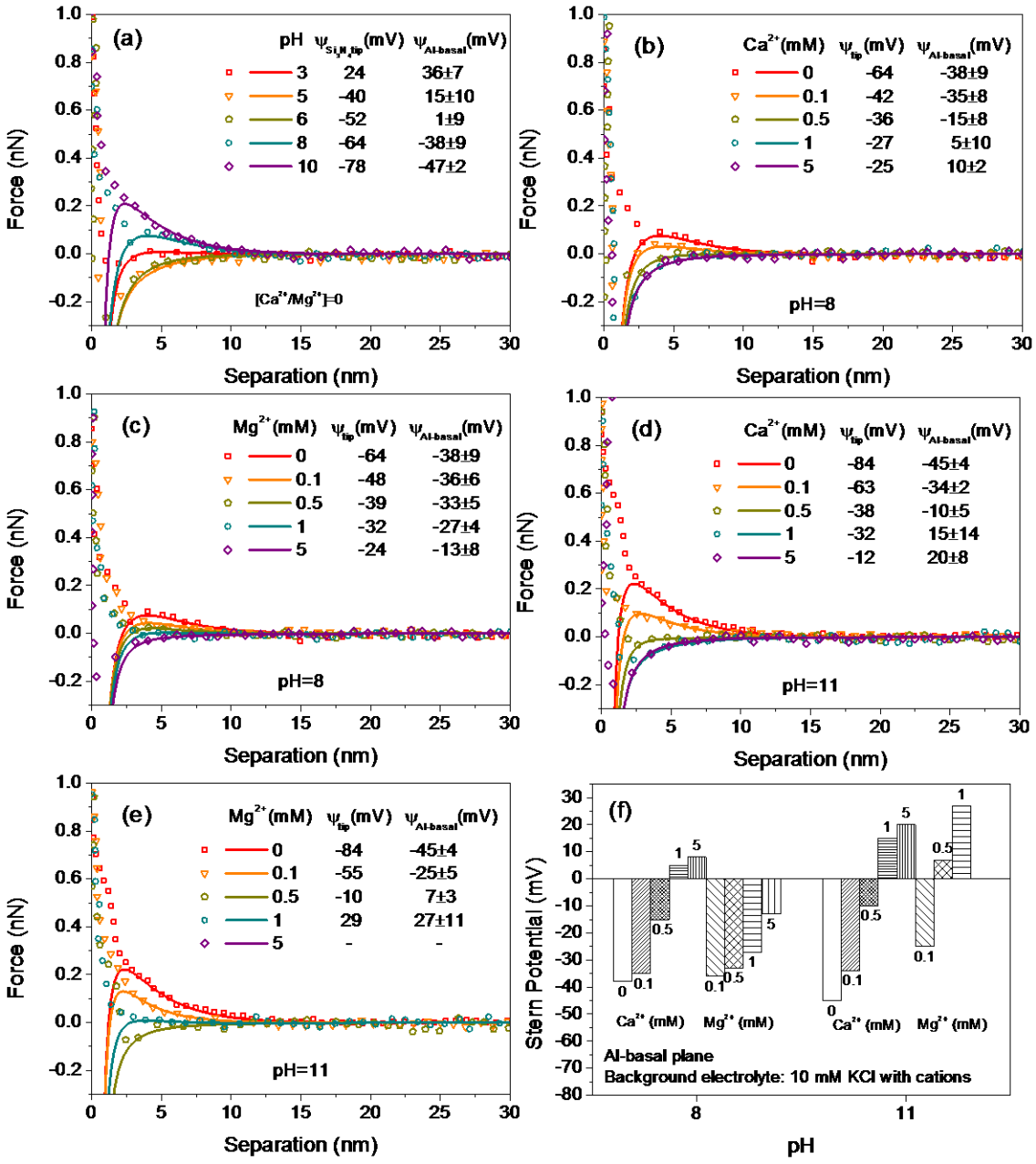

Figure 4.9 Interaction forces between the AFM Si_3N_4 tip and the Al-basal plane of kaolinite in 10 mM KCl solutions (a) at different pH, (b) at pH 8 containing different concentrations of Ca^{2+}, (c) at pH 8 containing different concentrations of Mg^{2+}, (d) at pH 11 containing

different concentrations of Ca^{2+}, and (e) at pH 11 containing different concentrations of Mg^{2+}; and (f) Summary of the Stern potential of kaolinite Al-basal plane at pH 8 and 11 in 10 mM KCl solutions containing different concentrations of Ca^{2+} and Mg^{2+}.

Interaction force curves between the AFM tip and the aluminum oxy-hydroxyl surface of kaolinite (Al-O-OH) in 10 mM KCl solution under various pH environments are shown in Figure 4.9 (a). The protonation and deprotonation of the exposed Al-OH surface groups are responsible for the formation of a net surface charge. However, constant surface potential equation could hardly be used to fit the experimental force curves. A better fitting result was obtained using the mixed BC equation, which may be caused by: 1) isomorphic substitution of Al^{3+} by Mg^{2+} in the octahedron sheet; 2) the pulling effect of surface groups from the T sheet. Repulsive interaction force found at pH 3 indicates that Al-basal plane of kaolinite is positively charged under this condition. Attraction force curves occurred at pH 5 and 6 meaning that this surface still carries positive charge. However, when the solution pH was increased to 8 and 10, the kaolinite Al-basal plane became negatively charged because repulsive force curves were obtained between the negatively charged AFM tip and the particle surface. Hence, the PZC of kaolinite Al-basal plane was found to be between pH 6 and 8, which agrees well with the result reported by Gupta et al[35]. These findings also proved that the Al-basal plane is slightly pH-sensitive because its Stern potential changed only slightly, except when the solution pH was close to its PZC.

Significant impact of divalent cations on the amphoteric Al-OH surface groups was observed due to the formation of surface complexes ($AlO(H_2O)Ca(H_2O)_5^+$ and $AlO(H_2O)Mg(H_2O)_5^+$) and electrostatic attraction. The mixed BC equation was adopted in the fitting process. Figure 4.9 (b) reveals the influence of Ca^{2+} on the charging

characteristics of kaolinite Al-basal plane. When the concentration of Ca^{2+} was increased from 0 to 0.1 mM, and to 0.5 mM, the interaction forces were repulsive, but when the addition of Ca^{2+} was further increased to 1 mM, the interaction forces became net attractive, which demonstrates that the Stern potential of kaolinite Al-basal plane was reversed from negative to positive at the addition of 1 mM Ca^{2+} in 10 mM KCl solutions at pH 8. The interaction force reduced to almost zero when the addition of Ca^{2+} was increased to 5 mM due to large extent of the electrical double-layer compression. However, the interaction forces between the AFM tip and the kaolinite Al-basal plane were found to be monotonically repulsive with the addition of Mg^{2+} varying from 0.1 to 5 mM at pH 8. The addition of 1mM Ca^{2+} resulted in charge reversal of the Al-basal plane while 1 mM Mg^{2+} did not. This implies that Ca^{2+} has a stronger effect than Mg^{2+} on the Stern potential of kaolinite Al-basal plane at pH 8. According to the quantitative model for the adsorption of hydrolysable metal ions on oxide-liquid interface proposed by James and Healy[69], the free energy change of adsorption is the sum of the change in coulombic energy, the change in secondary solvation energy and the change in a specific 'chemical' interaction, that is: $\Delta G^0{}_{ads_i} = \Delta G^0{}_{coul_i} + \Delta G^0{}_{solv_i} + \Delta G^0{}_{chem_i}$. At pH 8, $\Delta G^0{}_{chem_i}$ is negligible because there is almost no specific adsorption reaction for both cations. Generally, for two metal ion species of the same charge, the larger the ionic dimension, the more negative the sum of the coulombic and solvation energy change, which means larger ion is more favorable to the adsorption process. Moreover, Yan et al.[85] reported that the less hydrated Ca^{2+} could be more proximal to the oxide surface than Mg^{2+} due to its lower hydration enthalpy. As a result, compared to Mg^{2+}, Ca^{2+}, which has a larger ionic dimension and is less hydrated,

gets closer to the clay surface, thus generating a stronger impact on the Stern potential of kaolinite Al-basal plane.

Comparing (b) and (d), (c) and (e) in Figure 4.9, the effect of the first-order metal hydroxyl groups on the Al-basal surface is clearly seen when the solution pH was increased from 8 to 11. The surface charge reversal point for Ca^{2+} addition are the same (1mM addition) at pH 8 and 11, but because the concentration of $Ca(OH)^{+}$ increases significantly with solution pH, the main binding mechanism with Al-OH changes from surface complexion of $Ca(H_2O)_6^{2+}$ to specific adsorption of $Ca(OH)^{+}$. Therefore, the equation needed to fit the experimental forces changes from mixed BC equation at pH 8 to constant surface charge density equation at pH 11. Charge reversal occurred at 0.5 mM Mg^{2+} addition at pH 11 implies that $Mg(OH)^{+}$ becomes dominant, which leads to the formation of a strong covalent bond ($AlOMg^{+}$) with the surface Al-OH groups. Magnesium ions were also found to have bigger impact than calcium ions on the Stern potential of kaolinite Al-basal plane at pH 11, probably due to the formation of magnesium hydroxide precipitate on the surface.

4.2.5 Effect of divalent cations on Stern potential of kaolinite edge surfaces

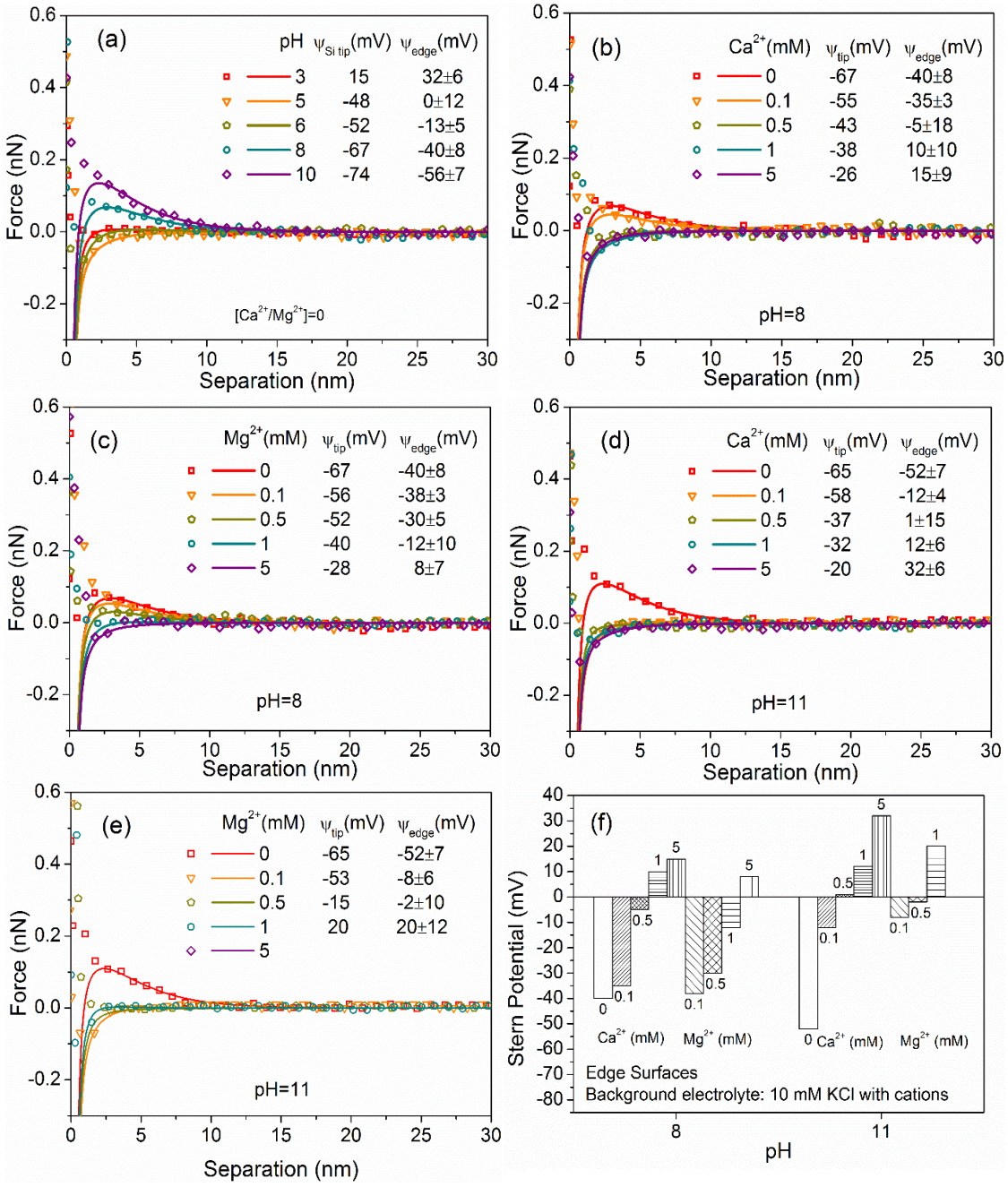

Figure 4.10 Typical interaction forces between the AFM Si tip and kaolinite edge surface in10 mM KCl solutions (a) at different pH, (b) at pH 8 containing different concentrations

of Ca^{2+}, (c) at pH 8 containing different concentrations of Mg^{2+}, (d) at pH 11 containing different concentrations of Ca^{2+}, and (e) at pH 11 containing different concentrations of Mg^{2+}; and (f) summary of the Stern potentials of kaolinite edge surfaces.

Interaction force curves between AFM Si tip and the edge surfaces of kaolinite shown in Figure 4.10 (a) manifest that the edge surface of kaolinite was positively charged at pH 3, and negatively charged from pH 6 to 10 in 10 mM KCl solutions. The PZC of the kaolinite edge surface was found to be around pH 5 because positive, zero, and negative surface potentials were all obtained during the fitting process. Because the surface groups of kaolinite edge surface are broken Si-O and Al-O bonds, which are easily hydrolyzed into Si-OH and Al-OH in KCl solutions. Si-OH and Al-OH would be protonated or deprotonated according to solution pH, so kaolinite edge surface carries a constant surface potential. Therefore, mixed BC equation was used to fit the experimental force curves in 10 mM KCl solutions.

In this research, the impacts of Ca^{2+} and Mg^{2+} on the surface potential of kaolinite edge surface were explored for the first time. Interaction force curves between the edge surfaces of kaolinite and the AFM Si tip in 10 mM KCl solutions with varying concentration of divalent ions are shown in Figure 4.10 (b)-(e). The interaction force curves were repulsive at the additions of 0 and 0.1 mM Ca^{2+}, which became attractive when the concentration of Ca^{2+} was increased to 0.5, 1 mM and 5 mM at pH 8. The interaction forces were still repulsive at 0.5 mM Mg^{2+} addition, albeit very weak. This means the impact of Mg^{2+} is smaller compared to Ca^{2+}, which matches well with what we found for kaolinite basal planes. At pH 11, when the concentration of divalent ions was increased to 0.5 mM, the fitting equation was changed from mixed boundary equation to constant surface charge

density equation because more specific adsorption happened. Ca^{2+} can reverse the surface charge sign at 0.5 mM addition, pH 11, due to specific adsorption. Again, the Stern potential of about 20 mM was obtained with 1 mM Mg^{2+} addition at pH 11, which is caused by magnesium hydroxide precipitation.

What needs to be mentioned is that typical force curves between AFM Si tip and kaolinite edge surfaces are quite different from the force curves between AFM Si tip and resin surface/cavity, which are extremely weak and very bumpy, respectively.

4.3 Summary

Following the successful preparation of micron-sized and smooth kaolinite basal planes, the Stern potentials of different surfaces were studied in 10 mM KCl solutions in the absence and presence of divalent cations (Ca^{2+} and Mg^{2+}, respectively) at different pH. The Stern potentials were derived by fitting the calculated DLVO force curves with the measured interaction force curves between the AFM tip and the basal planes. Proper boundary conditions were applied during the fitting processes. According to the experimental results, we can achieve the following understanding of the anisotropic surface charging properties and mechanisms of different kaolinite surfaces:

(1) The Stern potentials of the siloxane basal plane of kaolinite were negative from pH 3 to 10 in 10 mM KCl solutions, which barely changed with the variation of solution pH. The aluminum oxy-hydroxyl basal plane of kaolinite was slightly pH-sensitive and its PZC was found to be between pH 6 to 8. The pH-sensitive kaolinite edge surfaces had a PZC of about pH 5. These findings match well with previous research and generally accepted theory[35,36].

(2) For the siloxane basal plane of kaolinite, when Ca^{2+} was added into the 10 mM KCl solution at pH 8 and 11, the Stern potential became less negative without changing to positive with the additions increasing from 0.1 to 5 mM. When varying concentrations of Mg^{2+} were added into the background electrolyte, although the Stern potential remained negative at pH 8, it became positive at 1 mM Mg^{2+} addition at pH 11.

(3) For the aluminum oxy-hydroxyl basal plane of kaolinite, when the concentration of Ca^{2+} was increased from 0.1 to 0.5 mM at pH 8 and 11, the Stern potentials were both depressed without changing from negative to positive. When the addition of Ca^{2+} was further increased to 1 mM, the Stern potential of Al-basal plane was reversed to positive at both pHs. In the study of Mg^{2+}, the addition of Mg^{2+} did not have the ability to achieve charge reversal at pH 8, however, Mg^{2+} began to make serious impact on the Stern potential of the Al-basal plane at pH 11. At pH 11, 0.5 mM addition of Mg^{2+} could reverse the Stern potential from negative to positive.

(4) For kaolinite edge surfaces, the addition of Ca^{2+} can cause charge reversal at 1 mM and 0.5 mM, at pH 8 and 11, respectively. Charge reversal did not happen with the addition of Mg^{2+} at pH 8. However, with more formation of $Mg(OH)^{+}$ at pH 11, stronger specific adsorption reversed the surface charge sign of kaolinite edge at 1 mM addition.

(5) The Stern potentials of three kaolinite basal planes responded differently to solution pH due to different dominant charging mechanisms: isomorphic substitution for the Si-basal plane and protonation/deprotonation for the Al-basal plane and edge surfaces. At pH 8, the distinct responses to divalent cations of the three surfaces imply distinct binding mechanisms: electrostatic attraction dominates for the Si-basal plane and the formation of

strong surface complexes prevails on the Al-basal plane and edge surfaces (reactions and schematic of the adsorption mechanisms at pH 8 can be seen in Figure 4.11). Moreover, Ca^{2+} was found to be more favorable to the adsorption process than Mg^{2+} at pH 8, which is attributed to the larger ionic dimension and less hydrated nature of calcium ions than magnesium ions. At pH 11, Mg^{2+} had more significant impact on both basal planes than Ca^{2+}, and this is due to the nucleation and growth of magnesium hydroxide precipitate at the basal surfaces (reactions and schematic of the adsorption mechanisms at pH 11 can be seen in Figure 4.12). With the formation of the precipitate, the kaolinite basal and edge surfaces start to have the electrokinetic features of magnesium hydroxide, which accounts for the charge reversal occurred on all three kinds of surfaces with 1 mM Mg^{2+} addition at pH 11.

The possible reactions between the studied ions with kaolinite surfaces under different liquid environments were summarized as follows, and the corresponding schematics of the ion adsorption on kaolinite surfaces were illustrated in Figure 4.11 and 4.12.

At pH 8:

Electrostatic attraction: $\| XO^- + M(H_2O)_6{}^{2+} \leftrightarrow \| XO^-M(H_2O)_6{}^{2+}$ (4.1)

Outer-sphere complex: $\| XOH + M(H_2O)_6{}^{2+} \rightarrow \| XO(H_2O)M(H_2O)_5{}^{+} + H^+$ (4.2)

Here, X stands for Si or Al.

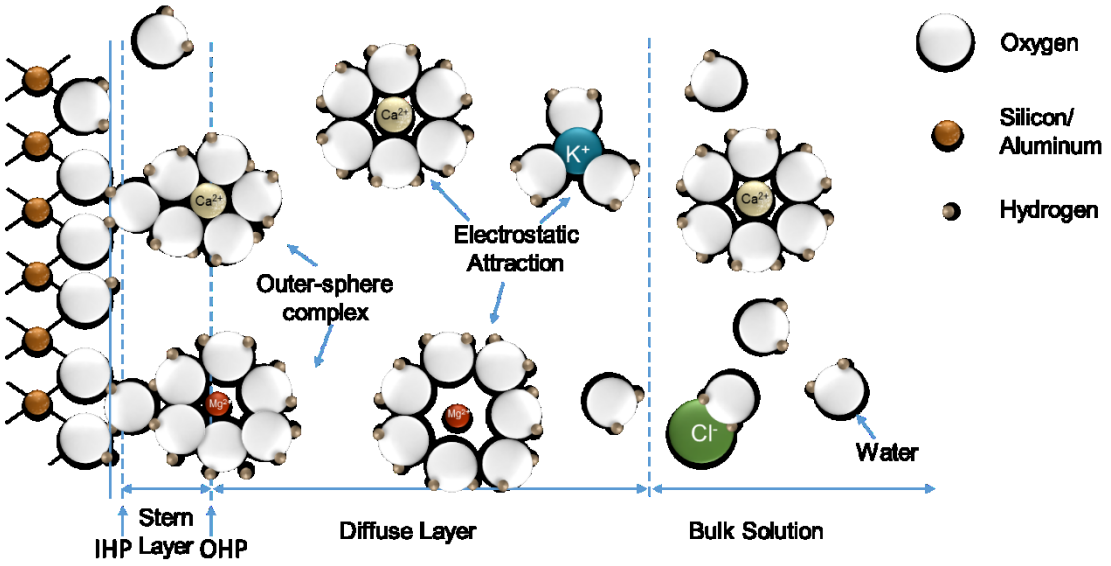

Figure 4.11 Schematics of the adsorption of divalent cations on kaolinite surfaces at pH 8.

At pH 11:

Specific adsorption: $\| \text{XOH} + \text{M(OH)}^{+} \rightarrow \| \text{XOM}^{+} + \text{HOH}$ (4.3)

Surface precipitation: $\| \text{XOH} + \text{Mg}^{2+} + 2\text{H}_2\text{O} \rightarrow \| \text{XOH}[\text{Mg(OH)}_2] + 2\text{H}^{+}$ (4.4)

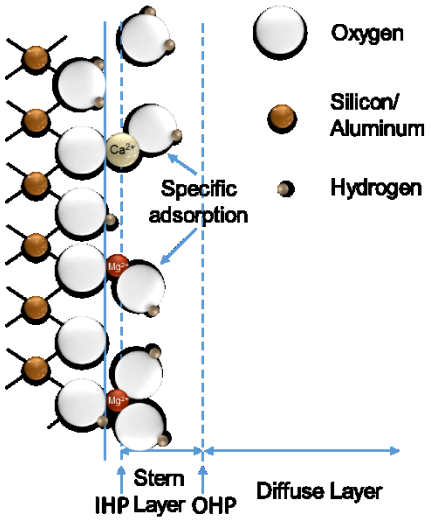

Figure 4.12 Schematics of the adsorption of divalent cations on kaolinite surfaces at pH 11.

In conclusion, we investigated the influence of divalent cations (Ca^{2+} and Mg^{2+}) on the anisotropic charging characteristics of kaolinite, which is a valuable clay mineral and has abundant applications. The new information on the Stern potentials of kaolinite basal planes in 10 mM KCl solutions with the presence of Ca^{2+} and Mg^{2+} gives insights into their adsorption mechanisms on distinct basal planes. Direct force measurements using AFM on carefully prepared kaolinite basal planes described in this research can be extended to other phyllosilicates to explore their surface properties and colloidal behaviors, which could lead to great contributions to the processing and utilization of broad natural resources.

Chapter 5 Imaging of Ion Adsorptions on Kaolinite Basal Planes

5.1 Introduction

In this chapter, atomic resolution imaging was performed on kaolinite basal planes to directly see the ion distributions on kaolinite surfaces. By this model-independent way, proposed ion adsorption mechanisms (in Chapter 4) were confirmed.

5.2 Results and discussion

In chapter 4, we reported the effect of divalent cations on the Stern potentials of kaolinite surfaces, and brought up possible ion adsorption mechanisms under different solution conditions. To further confirm our speculation, atomic resolution imaging was performed on kaolinite basal surfaces to explore the ion distribution. The atomic resolution imaging technique was described in Chapter 3, and the imaging processing procedure was provided in Appendix A.

5.2.1 Ion adsorption of monovalent ions

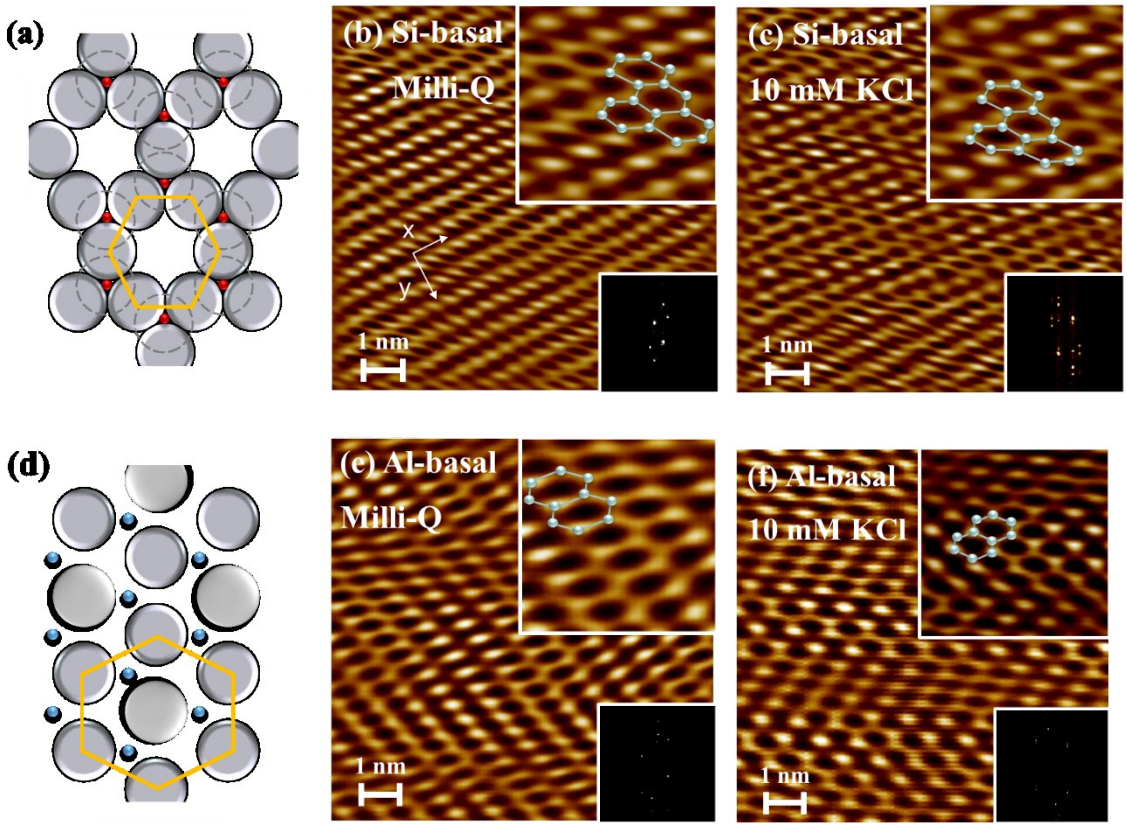

Figure 5.1 Surface lattice structure of kaolinite: Top view of the T sheet (a), and atomic resolution images of kaolinite Si-basal plane in Milli-Q water (b) and 10 mM KCl solution (c) at pH 5; Top view of the O sheet (d), and atomic resolution images of kaolinite Al-basal plane in Milli-Q water (e) and 10 mM KCl solution (f) at pH 5; with insets being high resolution views (top) and 2D spectrum (Fast Fourier Transform) image of the same data (bottom) (large white, solid circle represents oxygen; large, dotted circle shows the fourth oxygen atom of each tetrahedron pointing downward; small red circle represents silicon; large grey, solid circle represents hydroxyl; small blue circle represents aluminum).

The top view of the T sheet (Figure 5.1 (a)) and O sheet (Figure 5.1 (d)) shows hexagonal rings composed of outer oxygen atoms, with silicon/aluminum atoms residing below the

top oxygen plane. The hexagonal rings were clearly observed from the atomic resolution images of both kaolinite Si-basal plane and kaolinite Al-basal plane taken in ultrapure Milli-Q water, as shown in Figures 5.1 (b) and (e). In Figure 5.1 (b), the spacing between unit cells in x and y directions for kaolinite Si-basal plane was 0.514 nm and 0.996 nm, respectively. In Figure 5.1 (e), the spacing between unit cells for kaolinite Al-basal plane was 0.481 nm and 0.939 nm in x and y directions, respectively (the measurements of the spacing are provided in the supporting information). These spacing values agree well with the values reported in literature, which are given in Table 5.1.

Table 5.1 Comparison of the unit cell spacing of kaolinite basal planes

Method	Kaolinite Si-basal plane	Kaolinite Al-basal plane	Reference
XRD	x = 0.515 nm y = 0.89 nm		26
AFM	x = 0.514 nm y = 0.996 nm	x = 0.481 nm y = 0.939 nm	This work
	x = 0.51 nm y = 0.92 nm	x = 0.50 nm y = 0.905 nm	74
	x = 0.50 ± 0.04 nm	x = 0.36 ± 0.04 nm	95

The adsorption of K^+ and Cl^- on oppositely charged kaolinite basal planes was studied at pH 5. According to Hunter[63], specifically adsorbed ions can penetrate into the inner region to have a strong and short-range interaction with the surface. If K^+ or Cl^- can adsorb specifically at the interface, the strong binding between K^+ and Si-basal plane or between Cl^- and Al-basal plane would be able to alter the surface lattice structure. However, comparison of Figures 5.1 (b) and (c), (e) and (f) shows no visible change in the surface

lattice structure. Therefore, strong binding of monovalent ions (K^+ and Cl^-) on negatively and positively charged clay surfaces were not detected, regardless whether they were hydrated or not.

5.2.2 Ion adsorption of divalent ions

In Chapter 4, kaolinite Si-basal plane and Al-basal plane were determined to be negatively charged in KCl solutions at pH above 8. According to the speciation diagram (see Figure C1 in Appendix C) of 1 mM Ca^{2+}, the concentration of $Ca(OH)^+$ is negligible at pH < 8, and it increases dramatically with solution pH. The surfaces of the two basal planes were imaged when 1 mM Ca^{2+} was added into the KCl solution at pH 8 and 11, respectively. Figures 5.2 (a) and (b) show the surface structures of the two basal planes in 10 mM KCl + 1 mM Ca^{2+} aqueous solutions of pH 8. The periodic hexagonal rings remained on Si-basal planes as shown in Figure 5.2 (a) although it was not as sharp as in the case without calcium ions as shown in Figure 5.1 (c). In contrast, a distorted structure was seen on the Al-basal plane as shown in Figure 5.2 (b) in comparison with the case in the absence of calcium as shown in Figure 5.1 (e). However, the hexagonal rings completely disappeared on the Si-basal plane, so did the distortion on Al-basal plane, which were replaced by clear, periodic and rectangular structures on both surfaces when the solution pH was increased to 11.

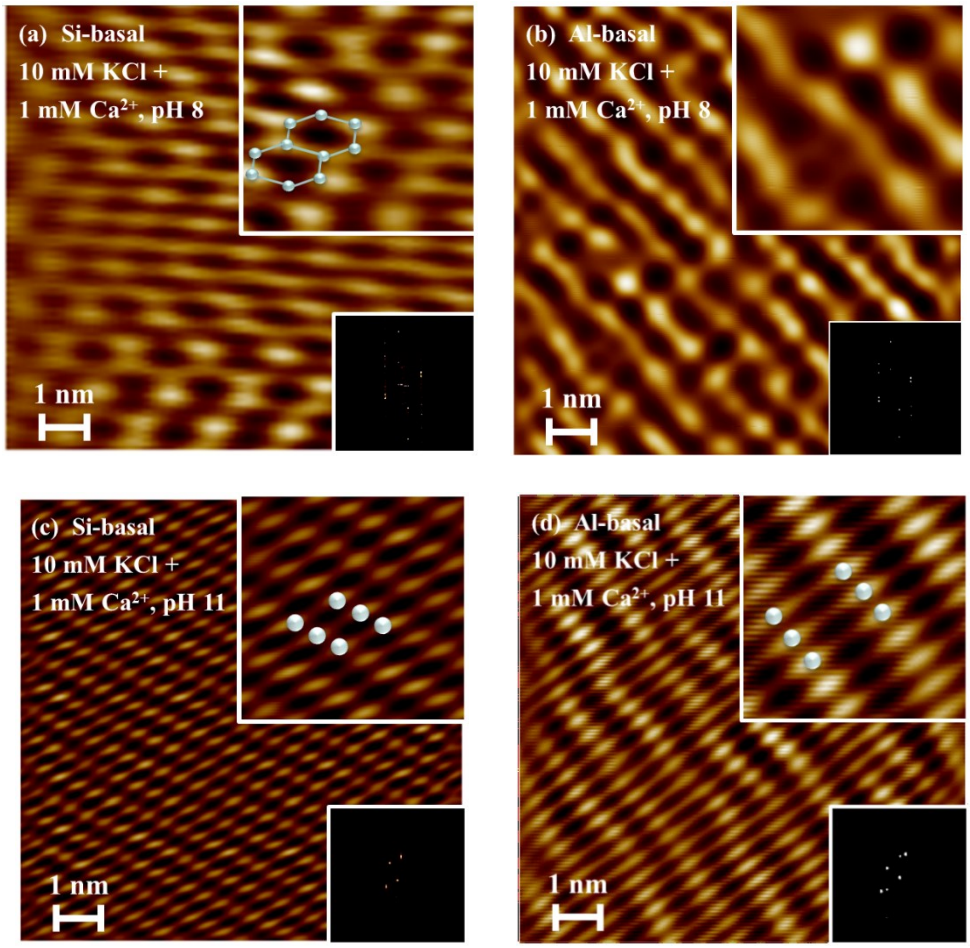

Figure 5.2 Atomic resolution images of kaolinite Si-basal (a), and Al-basal plane (b) in 10 mM KCl + 1 mM Ca^{2+} at pH 8; kaolinite Si-basal plane (c), and Al-basal plane (d) in 10 mM KCl + 1 mM Ca^{2+} at pH 11.

Although both basal planes were negatively charged at pH 8, the surface charging mechanisms are completely different. The surface siloxane (SiOSi) groups of Si-basal plane could be considered inert with the negative surface charges permanently carried by the Si-basal plane being mainly from isomorphic substitution. When Ca^{2+} were added at pH 8, the highly hydrated divalent calcium ions ($Ca(H_2O)_6^{2+}$) could only interact with the negatively charged surface through electrostatic attraction in the diffuse electrical double layer. When the AFM tip was scanning over the surface, the tip would easily push the

hydrated calcium ions away, which explains why the hexagonal surface structure was not affected. On the contrary, the amphoteric Al-OH surface groups on the Al-basal plane are pH-responsive and can form surface complexes with hydrated calcium ions[91]. The outer-sphere complexes ($AlO(H_2O)Ca(H_2O)_5^+$) would interfere with the hexagonal structure seen on bare Al-basal plane as revealed in Figure 5.2 (b). The scanning of the AFM tip over the charged solid surface is schematically illustrated in Figure 5.3.

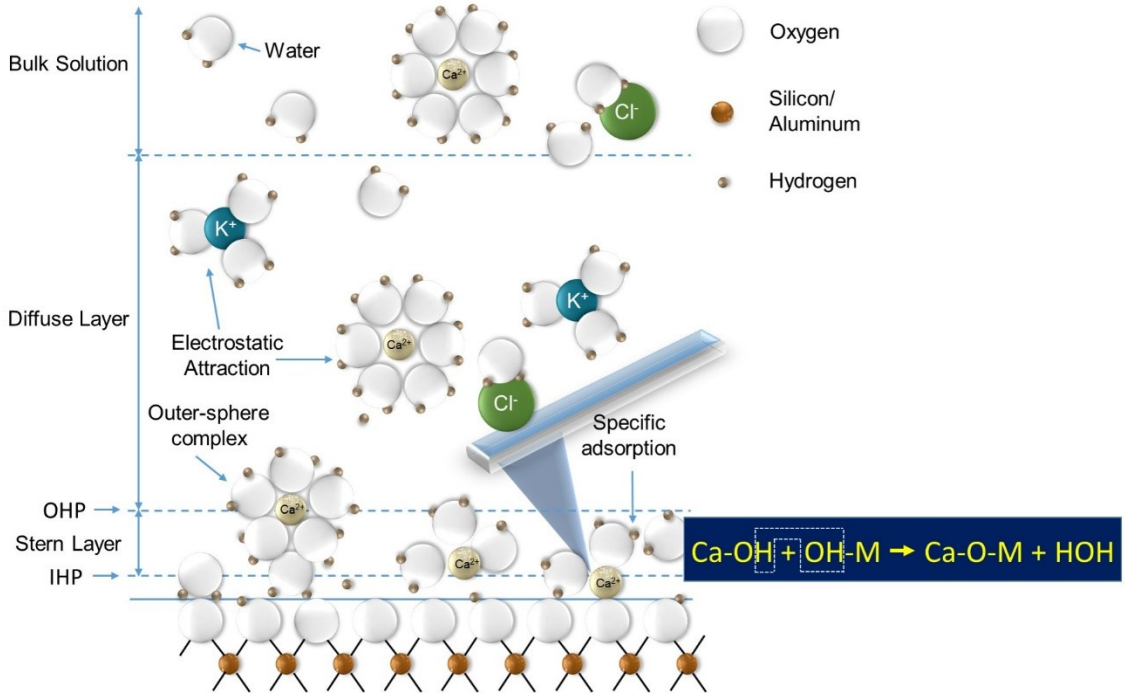

Figure 5.3 Schematic of AFM tip scanning surface in solution.

When the solution pH was 11, both basal planes showed rectangular structures. Because calcium ions would be highly hydrated in solution, they are unable to penetrate into the inner region and interact directly with the surfaces[63]. Therefore, the structure change coming from very strong surface binding should be attributed to the $Ca(OH)^+$ formed at high pH. The strong binding of $Ca(OH)^+$ at pH 11.7 was also seen on a glass slide by Gan

et al.[90] using XPS, which showed a rather higher ratio of Ca/Si after the glass slide was blown dry compared to the ratio obtained at pH 6. Therefore, it is only possible that the strong binding of $Ca(OH)^+$ (that can resist air blowing or AFM scanning) caused the change of the surface structure. This strong, direct surface binding of $Ca(OH)^+$ on kaolinite basal planes was the so-called specific adsorption.

5.3 Summary

According to the atomic resolution imaging on kaolinite surfaces under different background electrolytes, monovalent ions were not able to alter the surface lattice structure of kaolinite basal surfaces, no matter whether they were hydrated or not. The observed change in morphology of kaolinite basal plane surfaces in calcium solutions of increasing pH suggests strong and chemical binding of divalent cations on clay surfaces, mostly in the form of surface complexation and specific adsorption under low pH and high pH solution environment, respectively, following possible reactions (4.1), (4.2), and (4.3) proposed in Chapter 4.

Chapter 6 Understanding Rheology and Settling Behaviors of Kaolinite Suspension

6.1 Understanding the rheology behavior of kaolinite suspension

6.1.1 Calculation of interaction energy

After determining the Stern potentials of distinct kaolinite surfaces, the interaction energy between different surfaces could be calculated based on DLVO theory.

The van der Waals interaction energy per unit area between planar surfaces is calculated by:

$$U^{vdw} = -\frac{A}{12\pi D^2} \tag{6.1}$$

The electrical double-layer interaction energy per unit area between two planar surfaces is given by the following equations[85,96,97] under different boundary conditions:

For constant surface potential BC:

$$U^{\psi-\psi} = \frac{\varepsilon\varepsilon_0\kappa}{2}\{(\psi_a^2 + \psi_b^2)[1 - coth(\kappa D)] + 2\psi_a\psi_b cosech(\kappa D)\} \tag{6.2}$$

For constant surface charge density BC:

$$U^{\sigma-\sigma} = \frac{1}{2\varepsilon\varepsilon_0\kappa}\{(\sigma_a^2 + \sigma_b^2)[coth(\kappa D) - 1] + 2\sigma_a\sigma_b cosech(\kappa D)\} \tag{6.3}$$

For mixed BC:

$$U^{\sigma-\psi} = \frac{1}{2}\left\{2\psi_a\sigma_b sech(\kappa D) + \left(\frac{\sigma_b^2}{\varepsilon\varepsilon_0\kappa} - \varepsilon\varepsilon_0\kappa\psi_a^2\right) \times [tanh(\kappa D) - 1]\right\} \tag{6.4}$$

6.1.2 Shear yield stress measurement

Kaolinite suspension (35 wt%) was prepared in 10 mM KCl solutions and thoroughly mixed by IKA RW-20 overhead digital impeller (IKA Works, Inc., US) at 600 rpm for 30 min. The impeller was gently removed from the suspension, and the suspension was slowly poured into a beaker for pH adjustment. The suspension was put into a vacuum aspirator for one hour to remove the entrained air, and left overnight before proceeding to rheology testing.

An AR-G2 rheometer (TA instruments, DE) and a concentric cylinder geometry were used to study the rheology. The final pH of the kaolinite suspension was measured before the shear stress measurement. Rheological properties of kaolinite suspension were obtained by steadily increasing , then decreasing the shear rate (1 to 10 1/s) of the rotating spindle while measuring the shear stress. The suspension showed non-Newtonian behavior and the yield stress was obtained by extrapolation from the linear part of the rheometer data, using the Bingham model[98]:

$$\tau = \tau_B + \eta_P \gamma \tag{6.5}$$

where, τ is the shear stress, τ_B is the Bingham yield stress, η_P is the plastic viscosity and γ is the shear rate.

6.1.3 Understanding kaolinite suspension rheology behavior through interaction energy calculation

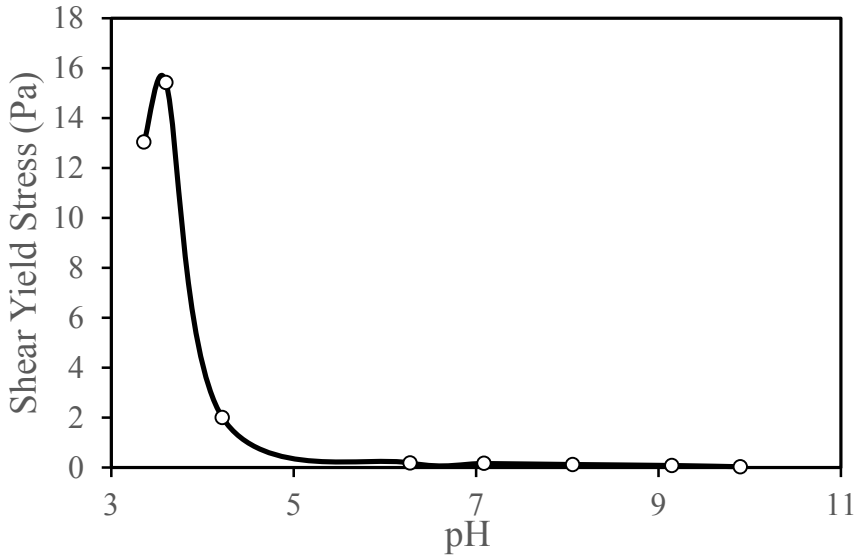

Figure 6.1 Impact of solution pH on the shear yield stress of kaolinite suspension.

The shear yield stress of kaolinite suspension was investigated in 10 mM KCl solutions from pH 3 to 10. The shear yield stress was about 13 Pa at pH 3, which increased to a maximum value of 15.4 Pa at pH 3.6. The shear yield stress started to decrease sharply from pH 3.6 to pH 4.3, and became almost neglectable from pH 5 to pH 10.

Kaolinite has three different surfaces: Si-basal plane, Al-basal plane and edge surface. In a kaolinite suspension, different surfaces would interact with each other, thus forming six kinds of inter-particle pairs: Si-basal plane vs Si-basal plane (Si vs Si), Al-basal plane vs Al-basal plane (Al vs Al), edge surface vs edge surface (E vs E), Si-basal plane vs Al-basal plane (Si vs Al), Si-basal plane vs edge surface (Si vs E) and Al-basal plane vs edge surface (Al vs E). Based on the Stern potential results in 10 mM KCl solutions at different pH, the

interaction energy per unit area for these six kinds of associations was calculated and shown in Figure 6.2.

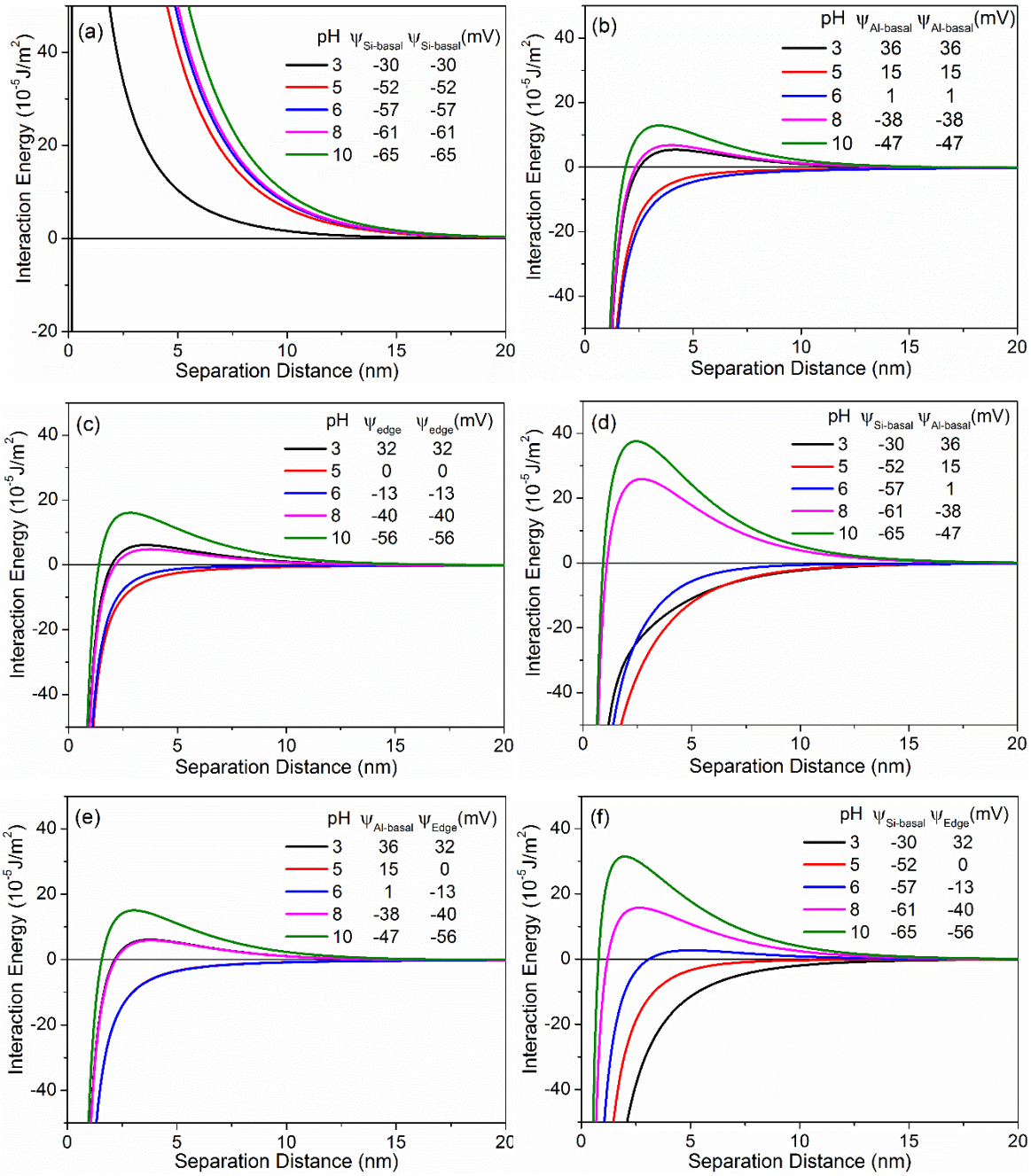

Figure 6.2 Interaction energy/unit area between different kaolinite surfaces in 10 mM KCl solutions at different pHs.

The aggregation structure among charged clay particles is mainly determined by the repulsive and attractive forces between two surfaces. We can see from Figure 6.2 (a) that, at pH 3, the repulsive force between Si-basal plane and Si-basal plane is significantly smaller than all other cases. The net repulsive forces between Al-basal planes and edge surfaces (shown in Figure 6.2 (b) and (c)) at pH 3, 8 and 10 are not very different, and they gradually change to small attraction at pH 5 and 6. Although the interaction energy was calculated between two same surfaces and they carried the same surface charges/Stern potentials, the interaction energy could be attractive when the Stern potentials were low (pH 5 and 6, in this case). This is because the attractive VDW force overcomes the repulsive EDL force, and becomes dominant in these cases. In Figure 6.2 (d), we can see that the attraction between Si-basal plane and the Al-basal plane became significant at pH 3 and 5, especially at pH 5. Attractive interaction was obtained when Al-basal plane interacted with edge surface at pH 5 and 6, which became slightly repulsive at pH 3 and 8, and the repulsion reached its maximum at pH 10. The interaction between Si-basal plane and edge surfaces gradually changed from attractive to repulsive as the solution pH increased from 3 to 10. Based on the calculated interaction energy profiles given in Figure 6.2, we can predict the pH of the maximum shear yield stress for different pairs of surfaces, which is listed in Table 6.1.

Table 6.1 Prediction of the pH of the maximum shear yield stress for different pairs of surfaces from the calculated interaction energy profiles.

Pairs of surfaces	Predicted pH of the maximum shear yield stress
Si vs Si	3
Al vs Al	6
E vs E	5
Si vs Al	5
Si vs E	5
Al vs E	3

It can be seen from Table 6.1 that, among the six kinds of pairs of surfaces, the maximum yield stress of two kinds (Si vs Si, and Al vs E) would occur at pH 3, and three kinds (E vs E, Si vs Al, and Si vs E) would occur at pH 5. Therefore, it is reasonable to predict that the maximum shear yield stress for the whole system may occur between pH 3 and 5. Moreover, according to the calculation results showed in Figure 6.2, it can be concluded that at pH 3, the interaction among kaolinite particles in a suspension was dominated by big attraction between Si-basal plane vs edge surfaces, and Si-basal plane vs Al-basal plane. The repulsion between same surfaces at pH 3 are relatively small compared to pH 6, 8 and 10, and it became even smaller when solution pH increased from 3 to 5. The particles tend to come closer and form card house structure (see Figure 6.3 (a)) via attractions between basal planes and edge surfaces at pH around 3, which explains why the highest shear-yield stress was obtained at pH 3.6 (see Figure 6.1).

At pH 5, the attractive interaction between particles come from Al-basal vs Al-basal, edge vs edge, Si-basal vs Al-basal and Si-basal vs edge. The shear-yield stress became rather small but still not negligible, which means the newly formed structure at pH 5 was not the strong card house structure that can introduce high shear-yield stress. Therefore, the

dominated attraction should come from Si-basal plane vs Al-basal plane and Al-basal plane vs Al-basal plane, and the particles would form basal plane vs basal plane (mainly dominated by Si-basal) stacking structure as illustrated in Figure 6.3 (b).

When the solution pH was further increased to 6, 8 and 10. Net repulsion occurred at almost all inner particle associations, so the particles could not get closer to each other, and thus staying dispersed in the solution (see Figure 6.3 (c) for the dispersed structure). This is also why kaolinite particles are hard to settle down in a pH 8 process water in oil sands tailings.

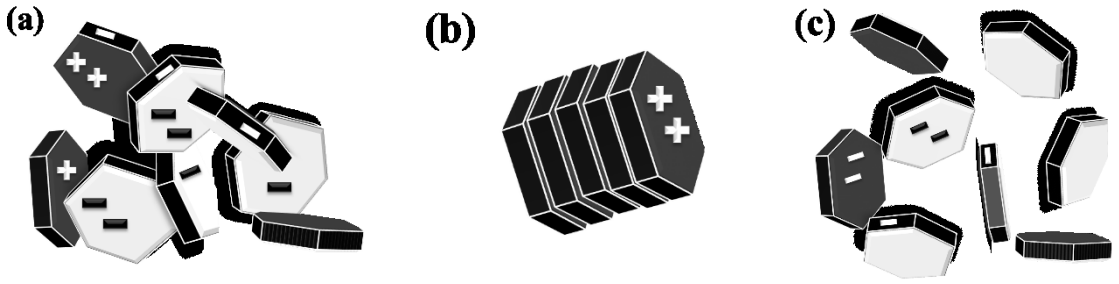

Figure 6.3 Proposed aggregate structures: (a) card house structure; (b) parallel stacking; (c) dispersed structure.

6.2 Understanding the settling behavior of kaolinite suspension

6.2.1 Settling test

Because the pH of oil sands tailings is about 7.5 to 8, and at this pH, Ca^{2+} and Mg^{2+} have similar effect on the kaolinite particles, the settling tests were only conducted in 10 mM KCl solutions with the addition of Ca^{2+} at pH 8. To investigate the impact of magnesium precipitate, settling tests were also performed with 5 mM Ca^{2+} and Mg^{2+} addition at pH 11. Kaolinite suspensions (5%) were prepared in 10 mM KCl solutions containing various concentrations of calcium chloride. The suspensions were mixed by IKA RW-20 overhead

digital impeller (IKA Works, Inc., US) at 600 rpm for 5 min. The pH of the well-dispersed suspensions were adjusted to 8 using 1 M HCl and 1M KOH while being magnetically stirred. The prepared suspenisons were transferred into graduate cylinders (100 mL) for settling test.

6.2.2 Understanding kaolinite suspension settling behavior through interaction energy calculation

The mudline, i.e., the interface between the supernatant and sediments, was recorded as a function of the settling time. The mudline height was calculated using the absolute height of the mudline divided by the total height of the suspension. The settling curves describe the change of the mudline height vs settling time, which were shown in Figure 6.4. The initial settling rate (ISR) was defined as the initial slope of the settling curve.

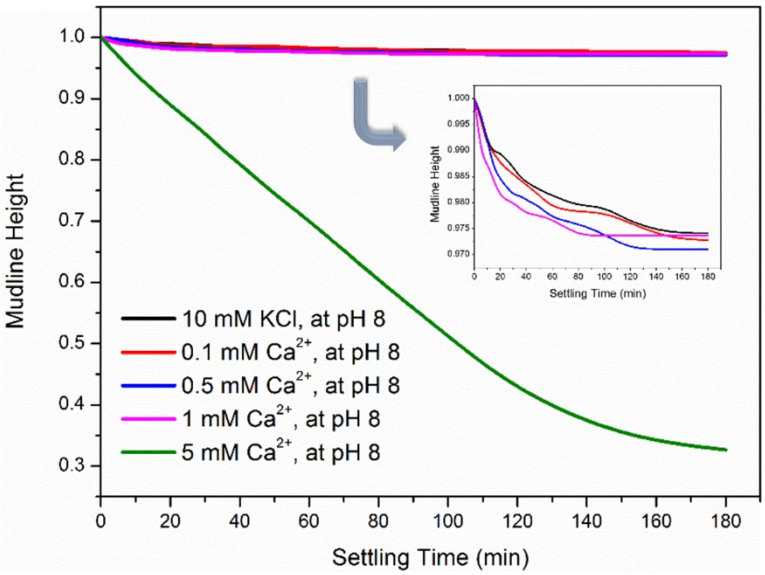

Figure 6.4 Settling performance of kaolinite suspension.

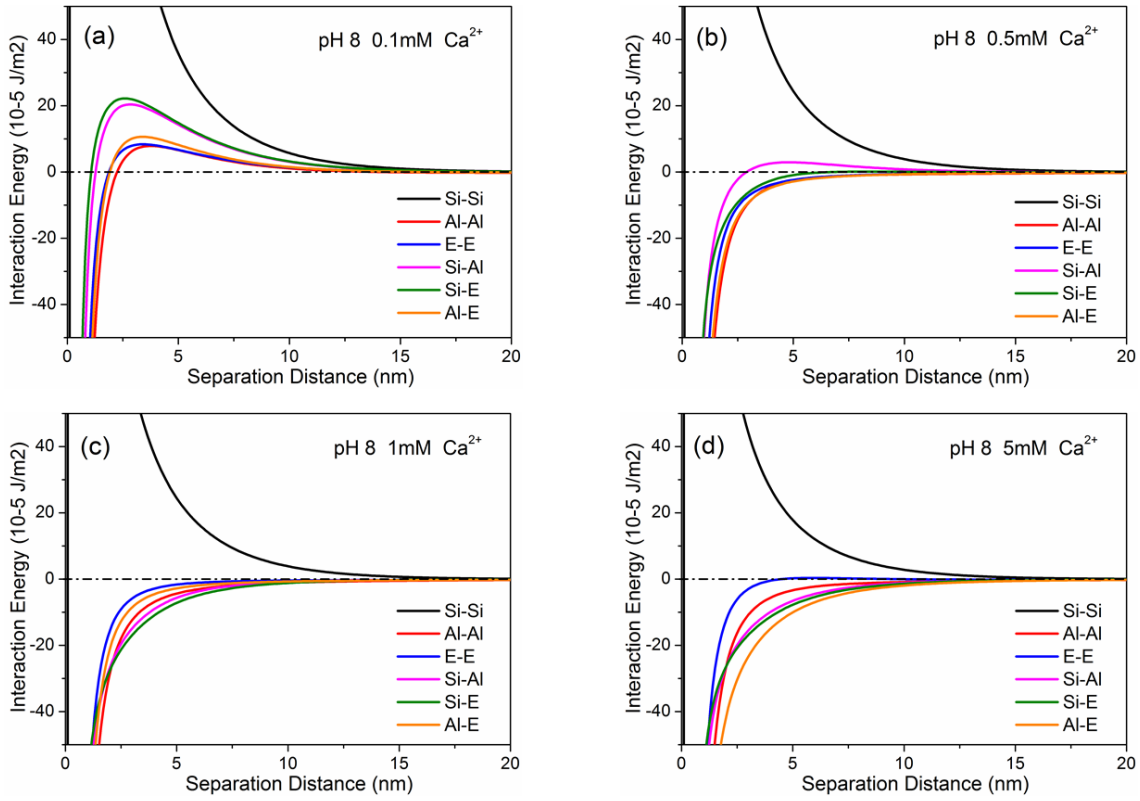

Figure 6.5 Impact of divalent cations on the interaction energy/unit area between different kaolinite surfaces.

When Ca^{2+} were added into the suspension, it can be seen in Figure 6.4 that the IRS increased very slowly when the concentration of Ca^{2+} was increased from 0 to 1 mM, but the IRS increased sharply when the concentration increased to 5 mM. This suggested that the addition of divalent cations can fasten the settling of kaolinite particles in a kaolinite suspension when the Stern potentials were highly decreased for all surfaces.

When 0.1 mM Ca^{2+} were added into the kaolinite suspension, the calculated interaction energies showed that the repulsion between different surfaces were highly reduced. However, all of the interaction energies were still repulsive, so the IRS with 0.1 mM divalent cation addition is almost the same as the IRS in 10 mM KCl solution, and only the

final mudline height of 0.1 mM Ca^{2+} addition is lower than that of 10 mM KCl solution case (see Figure 6.4).

Because the Stern potentials of kaolinite surfaces were further reduced with 0.5 and 1 mM Ca^{2+} addition, the interaction energies between surfaces changed from repulsive to attractive (see Figure 6.5), even between same surfaces, which is because the attractive VDW force became dominant. As we can see from Figure 6.4 that, the IRS for 0.5 mM divalent cation addition was still very close to that of 10 mM KCl solution case, and the IRS only increased a little at 1 mM divalent cation addition, which was not increased as expected. This is because the attraction among particles are still dominated by both basal vs basal and basal vs edge (see Figure 6.5 (b) and (c)), so the structure of the aggregation formed at these two conditions are card-house structure as shown in Figure 6.6 (b). The card house structure is able to trap a large amount of water and slows the settling process.

If we keep increasing the addition of divalent cations, the Stern potentials of kaolinite Al-basal and edge surfaces could be reversed from negative to positive, and the Stern potential of kaolinite Si-basal planes were also highly depressed according to the findings in Chapter 4. The interaction energies between kaolinite surfaces (see Figure 6.5 (d)) showed strong attraction except Si-Si, and the attraction among particles is dominated by Al-E and Si-E. The dominating attraction coming from basal vs edge may cause the formation of a brush-like aggregation structure, as shown in Figure 6.6 (c). This dense compact will ultimately lead to a fast settling result shown in Figure 6.4. Moreover, the final mudline height with 5 mM Ca^{2+} addition was much lower than other cases, which is about 0.326.

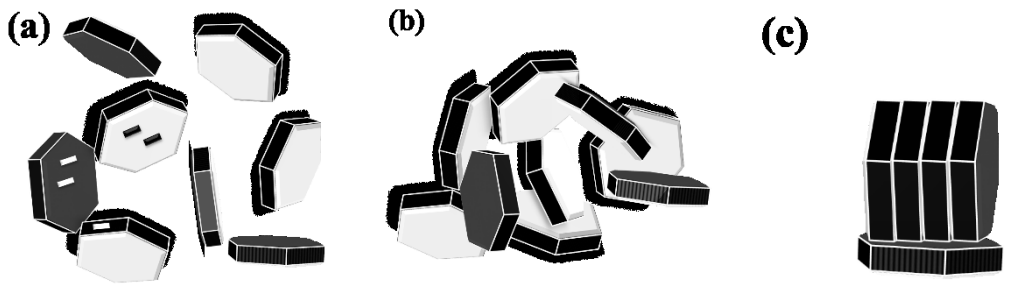

Figure 6.6 Proposed aggregate structures in 10 mM KCl solutions with 0, 0.1 mM Ca^{2+} addition (a), with 0.5 and 1 mM Ca^{2+} addition (b), and with 5 mM Ca^{2+} addition (c).

According to the Stern potential study in Chapter 4, the Stern potentials of the three kaolinite surfaces were all negative at pH 8 when there were 0, 0.1 mM addition of calcium ions added into 10 mM KCl solutions, so the kaolinite particles were repelling to each other in such suspensions as shown in Figure 6.6 (a). When 0.5 and 1 mM Ca^{2+} addition highly reduced the negative Stern potentials or even caused charge reversal of Al-basal and edge surfaces, card-house structure shown in Figure 6.6 (b) would reappear. When more calcium ions were added, the dominating attraction started to come from Al-basal planes vs edge surfaces, and from Si-basal planes vs edge surfaces, thus forming a brush-like structure as we can see from Figure 6.6 (c). Faster settling was observed when the addition of Ca^{2+} was increased as predicted, which is because of the compression of edl increased with the concentration of divalent cations, and the repulsive forces among particles were gradually reduced. The fast settling achieved at 5 mM Ca^{2+} addition is caused by the formation of the compact brush-like structure.

Settling tests were also performed in 5 mM addition of Mg^{2+} at pH 8 and 11 to see how the surface precipitation impacts the particle stacking style in a suspension. The results are shown in Figure 6.7.

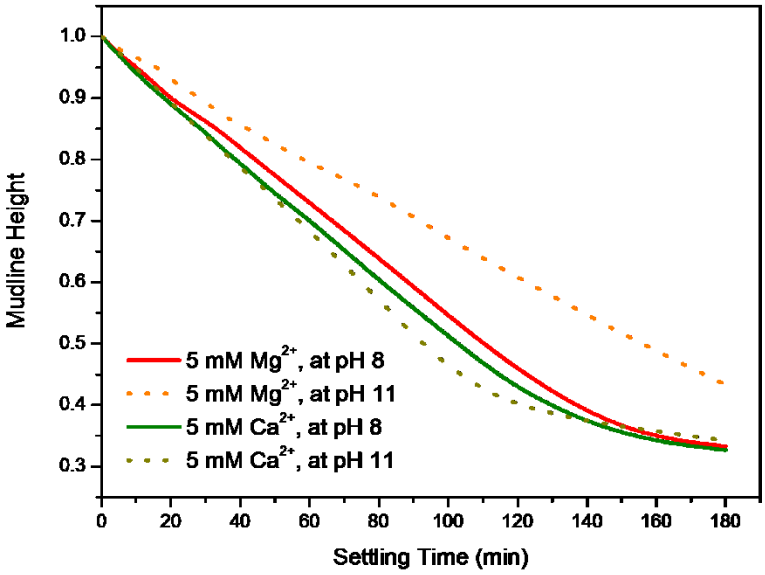

Figure 6.7 Impact of Mg^{2+} on the settling performance of kaolinite suspension.

As we can see from Figure 6.7 that the settling performance of kaolinite suspension in 10 mM KCl solution with 5 mM Mg^{2+} addition is very similar to the settling performance observed with the same concentration of Ca^{2+} addition. However, when the pH of electrolyte solutions was increased to 11, the ISR increased a little for Ca^{2+} addition due to stronger EDL compression. As anticipated, due to more formation of magnesium precipitate at high concentration of Mg^{2+} dosage at pH 11, all three kinds of kaolinite surfaces started to have the electrokinetic features of magnesium precipitate. Thus, the repelling forces among kaolinite particles increased, resulting in a smaller ISR.

Chapter 7 Conclusions and Future Work

7.1 Conclusions

In this research, the influence of divalent cations (Ca^{2+} and Mg^{2+}) on the anisotropic charging characteristics of kaolinite were thoroughly studied. The new information on the Stern potentials of kaolinite surfaces in 10 mM KCl solutions in the presence of Ca^{2+} and Mg^{2+} gives insights into their adsorption mechanisms on distinct kaolinite surfaces. Direct force measurements using AFM on kaolinite basal planes and edge surfaces described in this research can be extended to other phyllosilicates to explore their surface properties and colloidal behaviors, which could lead to great contributions to the processing and utilization of broad natural resources.

To further investigate the ion adsorption mechanisms, atomic resolution imaging was performed. As a sophisticated technique, atomic resolution imaging is of great application potentials in colloids and interface field. A detailed operation procedure was described in this work. In-situ observation of ion distribution at the solid-liquid interface allowed us to understand the interaction between divalent cations and kaolinite surfaces. When calcium ions were added into the background solution at high pH, we could see from the in-situ images that kaolinite surface lattice changed from hexagonal rings to rectangular arrays, which was caused by the strongly and specifically adsorbed $Ca(OH)^{+}$.

Finally, the calculation of the interaction energy between kaolinite surfaces explained the macroscopic behaviors of kaolinite suspension under different solution conditions. The success link between the microscopic world and the macroscopic world not only provides

valuable fundamental guidance for industry application, but also proves that our methods used in the Stern potential study are feasible and reliable.

In conclusion, the major contributions of this work are:

1) in this study, the method used to obtain the Stern potential of a sample surface based on ion adsorption mechanism were discussed in detail, which can lead to more accurate Stern potential results;

2) based on the knowledge of the Stern potential of phyllosilicate clay, the aggregate structure of the clay particles can be predicted by calculating the interaction energies among the interacting surfaces. This not only laid a good foundation for future research in tailings treatment, but can also be used to other research areas, such as controlling nano-structure of catalyst, synthesizing structural materials, etc.

3) with the presence of Ca^{2+} in the electrolyte solution of high pH, in situ imaging of the ion distribution at kaolinite-electrolyte interface directly showed the existence of specific adsorption for the first time. This technique can also be applied to explore the interaction mechanisms between reagents and mineral surfaces (e.g., the effect of citric acid on reducing coagulation of bitumen with kaolinite), to investigate the impact of ambient conditions on the nanostructure features of material surfaces (such as membranes, semiconductors, etc.), and so on.

7.2 Recommendations for future work

- In this study, the force fitting process can only achieve good fit at the separation distance > 3 nm from the surface. To obtain a better fit, future research may

consider including the repulsive non-DLVO hydration force into the calculation of theoretical interaction force:

$$F = F_{vdw} + F_{edl} + F_{hydration}$$

The calculation of the hydration force suitable for this AFM tip-solution-substrate system has been provided by Drelich et al. [75]

- Calculate the surface charge density of kaolinite basal surfaces when divalent cations were added into the 10 mM KCl solution. Use the impact of the divalent cation on the surface charge density to prove the feasibility of obtaining the surface lattice structure change seen in Chapter 5.
- When 1 mM Ca^{2+} added into the background solutions of pH 11, in order to confirm the change of the crystal lattice structure observed on Si-basal plane and Al-basal plane of kaolinite was caused by specifically adsorbed calcium ions, TOM-SIMS or DFT calculation could be done in the future to provide further information.
- Determine the ratios of solid to cation used in the Stern potential study, and calculate the usage of cation for settling test using the same solid to cation ratios. Then conduct settling tests again to see how divalent cations affect the settling behavior of kaolinite suspension.
- Divalent cations can affect kaolinite aggregate structure by influencing the thickness of electrical double-layer and the Stern potentials of kaolinite surfaces. To find the link between the divalent cation and the kaolinite aggregate structure, the settling performance of kaolinite suspension should be investigated under different concentrations of divalent cations (from 1 mM to 10 mM). This link can be used to find the optimum dosage of divalent cations for achieving fast settling.

Bibliography

(1) WATER MANAGEMENT IN OIL SANDS MINING FACILITIES. http://www.oilsandsmagazine.com/technical/mining/water-management?rq=water (accessed in Nov. 19, 2016).

(2) Masliyah, J. H. Bitumen Extraction, Extraction and Upgrading of Oil Sands Bitumen. Keyano College, Fort McMurray, AB 2003.

(3) Wang, L.; TRONG, D.-V.; Xu, Z.; Masliyah, J. H. Use of Short-Chain Amine in Processing of Weathered/oxidized Oil Sands Ores. *Energy & Fuels* **2010**, *24* (MAIJUN), 3581–3588.

(4) Liu, J.; Xu, Z.; Masliyah, J. Colloidal Forces between Bitumen Surfaces in Aqueous Solutions Measured with Atomic Force Microscope. *Colloids Surfaces A Physicochem. Eng. Asp.* **2005**, *260* (1), 217–228.

(5) Takamura, K.; R.S., C.; D.L., T. The Prediction of Electrophoretic Mobilities and the Coagulation Behavior of Bitumen-in-Water Emulsions in Aqueous NaCl and CaCl2 Solutions Using Ionizable Surface-Group Model. In *Proceedings of the Symposium on Flocculation in Biotechnology and Separation Systems*; San Francisco, CA.

(6) Liu, J.; Xu, Z.; Masliyah, J. Studies on Bitumen-Silica Interaction in Aqueous Solutions by Atomic Force Microscopy. *Langmuir* **2003**, *19* (9), 3911–3920.

(7) Zhao, H.; Dang-Vu, T.; Long, J.; Xu, Z.; Masliyah, J. H. Role of Bicarbonate Ions in Oil Sands Extraction Systems with a Poor Processing Ore. *J. Dispers. Sci. Technol.* **2009**, *30* (6), 809–822.

(8) Masliyah, J.; Zhou, Z.; Xu, Z.; Czarnecki, J.; Hamza, H. Understanding Water-Based Bitumen Extraction from Athabasca Oil Sands. *Can. J. Chem. Eng.* **2004**, *82* (4), 628–654.

(9) Takamura, K.; Wallace, D. The Physical Chemistry of the Hot Water Process. *J. Can. Pet. Technol.* **1988**, *27* (6).

(10) Takamura, K.; Wallace, D. Experimental and Theoretical Studies of the Hot Water Processability of Different Grades of Athabasca Oil Sands. In *Flocculation in biotechnology and separation systems*; Attia, Y. A., Ed.; Elsevier Science: Amsterdam, The Netherlands, 1987; pp 579–597.

(11) Hepler, L. G.; Smith, R. G. The Alberta Oil Sands: Industrial Procedures for Extraction and Some Recent Fundamental Research, AOSTRA Technical Publication Series# 14. *Alberta Oil Sands Technol. Res. Authority, Edmonton, AB* **1994**.

(12) Fong, N.; Ng, S.; Chung, K. H.; Tu, Y.; Li, Z.; Sparks, B. D.; Kotlyar, L. S. Bitumen Recovery from Model Systems Using a Warm Slurry Extraction Process: Effects of Oilsands Components and Process Water Chemistry. *Fuel* **2004**, *83* (14–15), 1865–1880.

(13) Zhao, H.; Long, J.; Masliyah, J. H.; Xu, Z. Effect of Divalent Cations and Surfactants on Silica-Bitumen Interactions. *Ind. Eng. Chem. Res.* **2006**, *45* (22), 7482–7490.

(14) Basu, S.; Nandakumar, K.; Lawrence, S.; Masliyah, J. Effect of Calcium Ion and Montmorillonite Clay on Bitumen Displacement by Water on a Glass Surface. *Fuel* **2004**, *83* (1), 17–22.

(15) Takamura, K.; Chow, R. S. A Mechanism for Initiation of Bitumen Displacement from Oil Sand. *J. Can. Pet. Technol.* **1983**, *22* (6).

(16) Currie, D. J.; Hathaway, A. P.; Isaacs, E. E.; Mar, A.; Morrison, D. N.; Richmond, C. The Potential of the Crumble Tests as a Tool for Oil Sands Research. In *30th Can. Chem. Eng. Conference*; 1980; Vol. 4, pp 1125–1142.

(17) Xu, Z.; Masliyah, J. H. *Effect of Recycle Water from CT Process on Bitumen Recovery from Oil Sands, Progress Report #2, A Joint Project with Syncrude, Suncor Albian and NSERC*; 2001.

(18) Kasperski, K. L. Review of Research on Aqueous Extraction of Bitumen from Mined Oil Sands. Unpublished Report. CANMET Energy Technology Centre, Natural Resources Canada, Devon, Alta. 2003.

(19) Sobkowicz, J. C. History and Developments in the Treatment of Oil Sands Fine Tailings. In *Keynote address in Proc. 14th International Conference on Tailings and Mine Waste, Vail, Colorado, USA*; 2010; pp 11–30.

(20) Masliyah, J. H.; Czarnecki, J.; Xu, Z. *Handbook on Theory and Practice of Bitumen Recovery from Athabasca Oil Sands - Volume 1: Theoretical Basis*; 2011.

(21) John, S. Oil Sands Tailings Technology Deployment Roadmap Project Report – Volume 2: Component 1 Results http://www.cosia.ca/uploads/documents/id10/Tailings Roadmap Volume 2 June 2012.pdf.

(22) Technical Guide for Fluid Fine Tailings Management http://www.cosia.ca/uploads/documents/id7/TechGuideFluidTailingsMgmt_Aug2012.pdf.

(23) Guggenheim, S.; Martin, R. T. Definition of Clay and Clay Mineral: Joint Report of the AIPEA Nomenclature and CMS Nomenclature Committees. *Clays Clay Miner.* **1995**, *43* (2), 255–256.

(24) Bergaya, F.; Theng, B. K.; Lagaly, G. *Handbook of Clay Science*; Elsevier, 2011; Vol. 1.

(25) Moore, D. M.; Guggenheim, S.; Martin, R. T. Definition of Clay and Clay Mineral; Joint Report of AIPEA Nomenclature and CMS Nomenclature Committees; Comment and Reply. *Clays Clay Miner.* **1996**, *44* (5), 710–715.

(26) Van Olphen, H. An Introduction to Clay Colloid Chemistry. *Soil Sci.* **1964**, *97* (4), 290.

(27) Gupta, V. No Title. *Surf. Charg. Featur. kaolinite Part. their Interact.* **2011**.

(28) Yan, L.; Alberta, U. of. *Study of Anisotropic Surface Property of Phyllosilicates by Atomic Force Microscopy*; 2013.

(29) Sondi, I.; Bišćan, J.; Pravdić, V. Electrokinetics of Pure Clay Minerals Revisited. *J. Colloid Interface Sci.* **1996**, *178* (2), 514–522.

(30) Duc, M.; Gaboriaud, F.; Thomas, F. Sensitivity of the Acid–base Properties of Clays to the Methods of Preparation and Measurement: 1. Literature Review. *J. Colloid Interface Sci.* **2005**, *289* (1), 139–147.

(31) Yeganeh, M. S.; Dougal, S. M.; Pink, H. S. B. T.-Q. E. & L. S. C. Vibrational Spectroscopy of Water at Charged Liquid/solid Interfaces; 1999.

(32) Hopkins, A. J.; McFearin, C. L.; Richmond, G. L. Investigations of the Solid–aqueous Interface with Vibrational Sum-Frequency Spectroscopy. *Curr. Opin. Solid State Mater. Sci.* **2005**, *9* (1–2), 19–27.

(33) Gerber, C. Atomic Force Microscope G. Binnig "a"and CF Quate 'b. *Phys. Rev. Lett.* **1986**.

(34) Butt, H.-J.; Cappella, B.; Kappl, M. Force Measurements with the Atomic Force Microscope: Technique, Interpretation and Applications. *Surf. Sci. Rep.* **2005**, *59* (1–6), 1–152.

(35) Gupta, V.; Miller, J. D. Surface Force Measurements at the Basal Planes of Ordered Kaolinite Particles. *J. Colloid Interface Sci.* **2010**, *344* (2), 362–371.

(36) Liu, J.; Sandaklie-Nikolova, L.; Wang, X.; Miller, J. D. Surface Force Measurements at Kaolinite Edge Surfaces Using Atomic Force Microscopy. *J. Colloid Interface Sci.* **2014**, *420*, 35–40.

(37) Eaton, P.; West, P. *Atomic Force Microscopy*; Oxford University Press, 2010.

(38) Derjaguin, B. V; Landau, L. Theory of the Stability of Strongly Charged Lyophobic Sols and of the Adhesion of Strongly Charged Particles in Solutions of Electrolytes. *Acta Physicochim.* **1941**, *14* (6), 633–662.

(39) Verwey, E. J. W.; Overbeek, J. T. G. *Theory of Stability of Lyophobic Colloids*; Elsevier: Amsterdam, 1948.

(40) Drelich, J.; Long, J.; Yeung, A. Determining Surface Potential of the Bitumen-Water Interface at Nanoscale Resolution Using Atomic Force Microscopy. *Can. J. Chem. Eng.* **2008**, *85* (5), 625–634.

(41) Kosmulski, M. *Chemical Properties of Material Surfaces*; Marcel Dekker: New York, 2001; Vol. 102.

(42) Yan, L.; Englert, A. H.; Masliyah, J. H.; Xu, Z. Determination of Anisotropic Surface Characteristics of Different Phyllosilicates by Direct Force Measurements. *Langmuir* **2011**, *27* (21), 12996–13007.

(43) Long, J.; Xu, Z.; Masliyah, J. H. Role of Illite-Illite Interactions in Oil Sands Processing. *Colloids Surfaces A Physicochem. Eng. Asp.* **2006**, *281* (1–3), 202–214.

(44) Yin, X.; Yan, L.; Liu, J.; Xu, Z.; Miller, J. D. Anisotropic Surface Charging of Chlorite Surfacesa. *Clays Clay Miner.* **2013**, *61* (2), 152–164.

(45) Fuerstenau, M. C.; Han, K. N. *Principles of Mineral Processing*; Society for Mining, Metallurgy, and Exploration: Littleton, Colo., 2003.

(46) Yan, L.; Masliyah, J. H.; Xu, Z. Understanding Suspension Rheology of Anisotropically-Charged Platy Minerals from Direct Interaction Force Measurement Using AFM. *Curr. Opin. Colloid Interface Sci.* **2013**, *18* (2), 149–156.

(47) Yin, X.; Yan, L.; Liu, J.; Xu, Z.; Miller, J. D. Anisotropic Surface Charging of Chlorite Surfaces. *Clays Clay Miner.* **2013**, *61* (2), 152–164.

(48) Alagha, L.; Wang, S.; Yan, L.; Xu, Z.; Masliyah, J. Probing Adsorption of Polyacrylamide-Based Polymers on Anisotropic Basal Planes of Kaolinite Using Quartz Crystal Microbalance. *Langmuir* **2013**, *29* (12), 3989–3998.

(49) Lu, Z.; Liu, Q.; Xu, Z.; Zeng, H. Probing Anisotropic Surface Properties of Molybdenite by Direct Force Measurements. *Langmuir* **2015**, *31* (42), 11409–11418.

(50) Hu, Y.; Wei, S.; Hao, J.; Miller, J. D.; Fa, K. The Anomalous Behavior of Kaolinite Flotation with Dodecyl Amine Collector as Explained from Crystal Structure Considerations. *Int. J. Miner. Process.* **2005**, *76* (3), 163–172.

(51) Miller, J. D.; Nalaskowski, J.; Abdul, B.; Du, H. Surface Characteristics of Kaolinite and Other Selected Two Layer Silicate Minerals. *Can. J. Chem. Eng.* **2008**, *85* (5), 617–624.

(52) Cuddy, G. *Oil Sands Geology. Guest Lecture Notes for Chemical Enginnering 534, Fundamentals of Oil Sands Extraction, January 7-9, at University of Alberta, Edmonton*; 2004.

(53) Liu, J. Surface Properties of Kaolinite Particles - Their Interactions and Flotation Consideration, The University of Utah, 2015.

(54) Yin, X.; Gupta, V.; Du, H.; Wang, X.; Miller, J. D. Surface Charge and Wetting Characteristics of Layered Silicate Minerals. *Adv. Colloid Interface Sci.* **2012**, *179–182*, 43–50.

(55) Tombácz, E.; Szekeres, M. Surface Charge Heterogeneity of Kaolinite in Aqueous Suspension in Comparison with Montmorillonite. *Appl. Clay Sci.* **2006**, *34* (1–4), 105–124.

(56) Alkan, M.; Demirbaş, Ö.; Doğan, M. Electrokinetic Properties of Kaolinite in Mono-and Multivalent Electrolyte Solutions. *Microporous Mesoporous Mater.* **2005**, *83* (1), 51–59.

(57) Gupta, V.; Hampton, M. A.; Stokes, J. R.; Nguyen, A. V; Miller, J. D. Particle Interactions in Kaolinite Suspensions and Corresponding Aggregate Structures. *J. Colloid Interface Sci.* **2011**, *359* (1), 95–103.

(58) Kosmulski, M. IEP as a Parameter Characterizing the pH-Dependent Surface Charging of Materials Other than Metal Oxides. *Adv. Colloid Interface Sci.* **2012**, *171*, 77–86.

(59) Helmholtz, H. L. F. von. Studies of Electric Boundary Layers. *Wied.Ann* **1879**, *7*, 337–382.

(60) Gouy, M. Sur La Constitution de La Charge Électrique À La Surface D'un Électrolyte. *J.Phys.Theor.Appl.* **1910**, *9* (1), 457–468.

(61) Chapman, D. L. LI. A Contribution to the Theory of Electrocapillarity. *London, Edinburgh, Dublin Philos. Mag. J. Sci.* **1913**, *25* (148), 475–481.

(62) Stern, O. Zur Theorie Der Elektrolytischen Doppelschicht. *Zeitschrift für Elektrochemie und Angew. Phys. Chemie* **1924**, *30* (21 - 22), 508–516.

(63) Hunter, R. J. *Foundations of Colloid Science*, Second.; Oxford University Press: Oxford ;New York, 2001.

(64) Grahame, D. C. The Electrical Double Layer and the Theory of Electrocapillarity. *Chem. Rev.* **1947**, *41* (3), 441–501.

(65) Modi, H. J.; Fuerstenau, D. W. Streaming Potential Studies on Corundum in Aqueous Solutions of Inorganic Electrolytes. *J. Phys. Chem.* **1957**, *61* (5), 640–643.

(66) Ardizzone, S.; Formaro, L.; Lyklema, J. Adsorption from Mixtures Containing Mono-and Bivalent Cations on Insoluble Oxides and a Revision of the Interpretation of Points of Zero Charge Obtained by Titration. *J. Electroanal. Chem. Interfacial Electrochem.* **1982**, *133* (1), 147–156.

(67) James, R. O.; Healy, T. W. Adsorption of Hydrolyzable Metal Ions at the Oxide—water Interface. I. Co (II) Adsorption on SiO_2 and TiO_2 as Model Systems. *J. Colloid Interface Sci.* **1972**, *40* (1), 42–52.

(68) James, R. O.; Healy, T. W. Adsorption of Hydrolyzable Metal Ions at the Oxide—water Interface. II. Charge Reversal of SiO_2 and TiO_2 Colloids by Adsorbed Co (II), La (III), and Th (IV) as Model Systems. *J. Colloid Interface Sci.* **1972**, *40* (1), 53–64.

(69) James, R. O.; Healy, T. W. Adsorption of Hydrolyzable Metal Ions at the Oxide-Water Interface. III. A Thermodynamic Model of Adsorption. *J. Colloid Interface Sci.* **1972**, *40* (1), 65–81.

(70) Gan, Y.; Franks, G. V. High Resolution AFM Images of the Single-Crystal α-Al2O3 (0001) Surface in Water. *J. Phys. Chem. B* **2005**, *109* (25), 12474–12479.

(71) Gan, Y.; Wanless, E. J.; Franks, G. V. Lattice-Resolution Imaging of the Sapphire (0 0 0 1) Surface in Air by AFM. *Surf. Sci.* **2007**, *601* (4), 1064–1071.

(72) Mugele, F.; Bera, B.; Cavalli, A.; Siretanu, I.; Maestro, A.; Duits, M.; Cohen-Stuart, M.; Van Den Ende, D.; Stocker, I.; Collins, I. Ion Adsorption-Induced Wetting Transition in Oil-Water-Mineral Systems. *Sci. Rep.* **2015**, *5*, 10519.

(73) Siretanu, I.; Ebeling, D.; Andersson, M. P.; Stipp, S. L. S.; Philipse, A.; Stuart, M. C.; Van Den Ende, D.; Mugele, F. Direct Observation of Ionic Structure at Solid-Liquid Interfaces: A Deep Look into the Stern Layer. *Sci. Rep.* **2014**, *4*, 4956.

(74) den Ende, D. Atomic Structure and Surface Defects at Mineral-Water Interfaces Probed by in Situ Atomic Force Microscopy. *Nanoscale* **2016**, *8* (15), 8220–8227.

(75) Drelich, J.; Long, J.; Xu, Z.; Masliyah, J.; White, C. L. Probing Colloidal Forces between a Si_3N_4 AFM Tip and Single Nanoparticles of Silica and Alumina. *J. Colloid Interface Sci.* **2006**, *303* (2), 627–638.

(76) Hamaker, H. C. The London—van Der Waals Attraction between Spherical Particles. *physica* **1937**, *4* (10), 1058–1072.

(77) Lifshitz, E. M. The Theory of Molecular Attractive Forces between Solids. **1956**.

(78) Israelachvili, J. N. *Intermolecular and Surface Forces: Third Edition*; 2011.

(79) Bergström, L. Hamaker Constants of Inorganic Materials. *Adv. Colloid Interface Sci.* **1997**, *70*, 125–169.

(80) Israelachvili, J. N. *Intermolecular and Surface Forces*, Third.; Academic Press: Burlington, MA, 2011.

(81) Graf, K.; Kappl, M. *Physics and Chemistry of Interfaces*; John Wiley & Sons, 2006.

(82) Sokolov, I.; Ong, Q. K.; Shodiev, H.; Chechik, N.; James, D.; Oliver, M. AFM Study of Forces between Silica, Silicon Nitride and Polyurethane Pads. *Journal of Colloid and Interface Science*. 2006, pp 475–481.

(83) Zhao, H.; Bhattacharjee, S.; Chow, R.; Wallace, D.; Masliyah, J. H.; Xu, Z. Probing Surface Charge Potentials of Clay Basal Planes and Edges by Direct Force Measurements. *Langmuir* **2008**, *24* (22), 12899–12910.

(84) Larson, I.; Drummond, C. J.; Chan, D. Y. C.; Grieser, F. Direct Force Measurements between Silica and Alumina. *Langmuir* **1997**, *13* (7), 2109–2112.

(85) Yan, L.; Masliyah, J. H.; Xu, Z. Interaction of Divalent Cations with Basal Planes and Edge Surfaces of Phyllosilicate Minerals: Muscovite and Talc. *J. Colloid Interface Sci.* **2013**, *404*, 183–191.

(86) Yin, X.; Drelich, J. Surface Charge Microscopy: Novel Technique for Mapping Charge-Mosaic Surfaces in Electrolyte Solutions. *Langmuir* **2008**, *24* (3), 8013–8020.

(87) Warszyński, P.; Adamczyk, Z. Calculations of Double-Layer Electrostatic Interactions for the Sphere/Plane Geometry. *J. Colloid Interface Sci.* **1997**, *187* (2), 283–295.

(88) Wang, M.; Revil, A. Electrochemical Charge of Silica Surfaces at High Ionic Strength in Narrow Channels. *J. Colloid Interface Sci.* **2010**, *343*, 381–386.

(89) Yang, D.; Xie, L.; Bobicki, E.; Xu, Z.; Liu, Q.; Zeng, H. Probing Anisotropic Surface Properties and Interaction Forces of Chrysotile Rods by Atomic Force Microscopy and Rheology. *Langmuir* **2014**, *30* (36), 10809–10817.

(90) Gan, W.; Crozier, B.; Liu, Q. Effect of Citric Acid on Inhibiting Hexadecane-Quartz Coagulation in Aqueous Solutions Containing Ca2+, Mg2+and Fe3+ions. *Int. J. Miner. Process.* **2009**, *92* (1–2), 84–91.

(91) Kasprzyk-Hordern, B. Chemistry of Alumina, Reactions in Aqueous Solution and Its Application in Water Treatment. *Advances in Colloid and Interface Science*. 2004, pp 19–48.

(92) Binner, J.; Zhang, Y. Characterization of Silicon Carbide and Silicon Powders by XPS and Zeta Potential Measurement. *J. Mater. Sci. Lett.* **2001**, *20* (2), 123–126.

(93) Lin, J. X.; Wang, L. Adsorption of Dyes Using Magnesium Hydroxide-Modified Diatomite. *Desalin. Water Treat.* **2009**, *8* (1–3), 263–271.

(94) Fuerstenau, M. C.; Miller, J. D.; Kuhn, M. C. *Chemistry of Flotation.*; Soc of Mining Engineers of AIME, 1985.

(95) Gupta, V.; Hampton, M. A.; Nguyen, A. V; Miller, J. D. Crystal Lattice Imaging of the Silica and Alumina Faces of Kaolinite Using Atomic Force Microscopy. *J. Colloid Interface Sci.* **2010**, *352* (1), 75–80.

(96) Masliyah, J. H.; Bhattacharjee, S. *Electrokinetic and Colloid Transport Phenomena*; 2005.

(97) Kar, G.; Chander, S.; Mika, T. . The Potential Energy of Interaction between Dissimilar Electrical Double Layers. *J. Colloid Interface Sci.* **1973**, *44* (2), 347–355.

(98) Mpofu, P.; Addai-Mensah, J.; Ralston, J. Influence of Hydrolyzable Metal Ions on the Interfacial Chemistry, Particle Interactions, and Dewatering Behavior of Kaolinite Dispersions. *J. Colloid Interface Sci.* **2003**, *261* (2), 349–359.

(99) Gan, W.; Crozier, B.; Liu, Q. Effect of Citric Acid on Inhibiting Hexadecane–quartz Coagulation in Aqueous Solutions Containing Ca^{2+}, Mg^{2+} and Fe^{3+} Ions. *International Journal of Mineral Processing*. 2009, pp 84–91.

Appendices

Appendix A Atomic resolution image processing

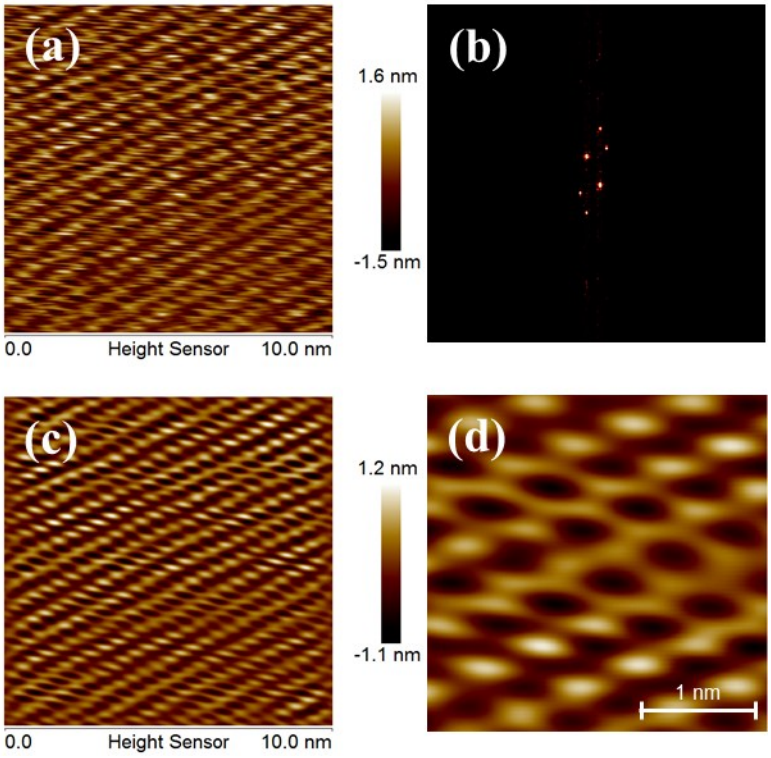

Figure A1. Image processing procedure. (a) Original atomic resolution image after being flattened, (b) Spectrum 2D image, (c) inverse FFT image, and (d) zoomed-in view of (c).

The atomic resolution image of the kaolinite Si-basal plane taken in Milli-Q water was used to show the image processing procedure. The original figure was 2nd-order flattened using NanoScope Analysis Version 1.8 (Bruker Corporation) and shown in Figure A1(a). Lowpass filtering can be used to further improve the image clarity if noise is high. Spectrum 2D function was then used to transform the image data to frequency domain via a 2D fast Fourier transform (FFT), as we can see in Figure A1(b). By passing selected

frequencies, the image was filtered and certain surface features (in this case, the surface lattice structure) were isolated, as shown in Figure A1(c). Finally, a zoomed-in view was provided to see the surface lattice structure image more clearly.

Appendix B Error analysis of the obtained Stern potentials

The AFM experimental force curves and the force fitting used to obtain the Stern potentials in Chapter 4 may bring about certain errors, which mainly come from following reasons:

1) Surface roughness of the substrate/kaolinite surfaces. The surface roughness of the kaolinite basal surfaces is between 0.3 ~ 1.2 nm, and the surface roughness of edge surfaces usually ranged from 1.06 ~ 2.3 nm, which is one of the contributions of the discrepancy between the experimental force curves and the theoretical force curves at short separation from the surfaces.

2) Non-DLVO forces were not taken into consideration in this study, such as the short-range hydration force.

3) Experimental force curves obtained from different locations on kaolinite surfaces may lead to a variation of the derived Stern potential, and the variation is usually between ± 2 to ± 8 mV. The variation of a few cases reached to about ± 10 mV, which usually happened near the PZC of the surfaces. This is because when near PZC, even slight change of the solution condition would cause big fluctuation of the Stern potentials of a surface.

4) In the calculation of the theoretical forces, although the surface charging mechanisms have been seriously explored and used to decide the studied surfaces carry constant surface potential or constant surface charge, absolute constant surface potential and constant surface charge are ideal cases. In reality, the interaction force between AFM tip and the substrate/kaolinite surface would always fall in between the two extreme cases. Therefore,

Calculating the theoretical forces based on surface charging mechanisms can only provide the best approximated forces to the experimental forces.

5) Error may also come from the determination of the spring constant of the cantilever, the deflection sensitivity, and the geometry of the AFM tip.

Appendix C Speciation diagram

Figure A1 shows the speciation diagram for 10^{-3} mol/L Ca^{2+} and Mg^{2+}, which was constructed using data from Fuerstenau et al.[94], and Gan et al.[99].

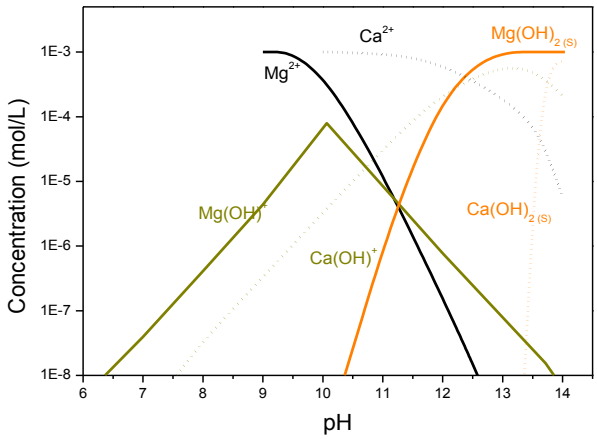

Figure C1. Concentration diagram for 10^{-3} mol/L Ca^{2+} and Mg^{2+}.